Automatische lokalisatie van referentiepunten op virtuele botmodellen

Automatic Localisation of Landmarks on Virtual Bone Models

Sofie Van Cauter

Promotoren: prof. dr. ir. B. Verhegghe, prof. dr. lth. M. Braem
Proefschrift ingediend tot het behalen van de graden van
Doctor in de Ingenieurswetenschappen: Biomedische Ingenieurstechnieken (UGent) en
Doctor in de Medische Wetenschappen (Universiteit Antwerpen)

Vakgroep Civiele Techniek
Voorzitter: prof. dr. ir. J. De Rouck
Faculteit Ingenieurswetenschappen en Architectuur

Vakgroep Translationele Neurowetenschappen
Voorzitter: prof. dr. P. Van de Heyning
Faculteit Geneeskunde en Gezondheidswetenschappen

UNIVERSITEIT GENT

Universiteit Antwerpen

Academiejaar 2011 - 2012

ISBN 978-90-8578-513-2
NUR 954
Wettelijk depot: D/2012/10.500/39

Supervisors:

prof. dr. ir. Benedict Verhegghe (promotor)
prof. dr. lth. Marc Braem (promotor)
dr. ir. Matthieu De Beule

Examination Committee:

prof. dr. lth. Marc Braem	University of Antwerp
prof. dr. ir. Patrick De Baets	Ghent University
dr. ir. Matthieu De Beule (secretary)	Ghent University
prof. dr. ir. Luc Taerwe (chairman)	Ghent University
dr. Olivier Vanderveken	University of Antwerp
prof. dr. Serge Van Sint Jan	Université Libre de Bruxelles
prof. dr. Peter Verdonk	Ghent University
prof. dr. ir. Benedict Verhegghe	Ghent University

Research units:

Biofluid, Tissue and Solid Mechanics for Medical Applications
Institute Biomedical Technology
Ghent University
De Pintelaan 185 - Blok B
B-9000 Ghent
Belgium

Lab Dental Materials
University of Antwerp
Groenenborgerlaan 171 - G.T.142
B-2020 Antwerp
Belgium

Aan mijn ouders,
voor hun inzet en motivatie

Dankwoord

Tijdens de voorbije vier jaar heb ik met verschillende zeer gemotiveerde mensen mogen samenwerken, die een belangrijke bijdrage geleverd hebben tot dit werk. Ik wil hen dan ook bedanken voor hun inzet en voor de fijne samenwerking.

Een eerste woord van dank gaat uit naar mijn promotoren: prof. Benedict Verhegghe en prof. Marc Braem. Jullie boden me de mogelijkheid en vrijheid om dit interessante onderzoek te voeren. Marc, bedankt voor de coördinatie van dit doctoraat in de Universiteit Antwerpen en de nuttige feedback op het geleverde werk. Benedict, het door jou ontwikkelde programma pyFormex is een rode draad doorheen deze thesis. De inspanningen die je levert om de functionaliteiten steeds uit te breiden zijn indrukwekkend en waren vaak cruciaal voor dit onderzoek. Bovendien was je altijd beschikbaar om even te overleggen en om programmeer- en Linuxtips te geven. Verder kon ik ook op de begeleiding van dr. Matthieu De Beule rekenen. Matthieu, dit werk is deels te danken aan jouw enthousiasme en inspanningen om als doctorassistent nieuwe projecten op te starten en mensen in contact te brengen. Ik heb ook je vele nuttige opmerkingen bij het uitschrijven van mijn onderzoek erg geapprecieerd.

Deze thesis is het resultaat van een nauwe samenwerking tussen ingenieurs, artsen en tandartsen en ik ben dan ook zeer dankbaar voor de input van tandarts dr. Walter Okkerse en de artsen Guy Brijs en prof. Peter Verdonk. Walter en Guy, jullie bezorgden me de nodige data en inzichten om de anatomie van de schedel te bestuderen. Jullie motivatie voor het verbeteren van de analyses en operaties is bewonderenswaardig. Walter, bedankt voor de tijd die je investeerde in dit project (inclusief de pyFormex analyses). Peter, dankzij jouw input kon ik mijn onderzoek verder toepassen op de femur. Bedankt om tijd vrij te maken om te brainstormen over nieuwe technieken en data te verzamelen. Ik apprecieer(de) ook je enthousiasme en vertrouwen in dit project. Tenslotte wil ik ook Mieke Van Haver bedanken om mij op weg te helpen bij het bestuderen van de anatomie van de femur en Emmanuel Audenaert voor het beschikbaar stellen van de femurmodellen.

Ik wil ook al mijn collega's bedanken voor de fijne koffie- en middagpauzes. Jullie verhalen en grappen zorgden steeds voor de nodige ontspanning. Daarnaast ben ik terecht trots om deel uit te maken van dit veelzijdige team. Patrick, bedankt om zowel een goede coach als teamlid te zijn. Pascal, jij legde de eerste contacten met de mensen van de Universiteit Antwerpen, die de basis waren voor dit project.

Bedankt hiervoor.

Dankzij mijn familie kon ik mij ook buiten de werkuren toeleggen op het schrijven van deze thesis. Mama, Chris, Martine en Frans, erg bedankt voor jullie zeer spontane hulp. Waldo, lieve schat, bedankt om mij de tijd te geven om dit doctoraat af te werken, om mijn werk na te lezen en om in mij te geloven. De toekomst is nog wat onzeker, maar ik weet alvast dat deze samen met jou, en met ons zoontje, enkel positief kan zijn! Wilson, jouw glimlach (of uitbundige gelach) en enthousiasme gaven me extra energie. Ik kon me geen betere ontspanning inbeelden.

Gent, februari 2012

Sofie

Table of Contents

List of Acronyms

1D	one-dimensional
2D	two-dimensional
3D	three-dimensional
AP	anteroposterior
CBCT	cone-beam computed tomography
CT	computed tomography
DFT	discrete Fourier transform
DP	distoproximal
FFT	fast Fourier transform
GTS	GNU Triangulated Surface Library
ML	mediolateral
MOI	moment of inertia
MRI	magnetic resonance imaging
RL	right-left
ROI	region-of-interest
SD	standard deviation
SI	superoinferior
TKA	total knee arthroplasty
TKP	totale knieprothese

Samenvatting

Hoofdstuk 1: Inleiding

Het opmeten van de anatomie aan de hand van referentiepunten is een gevestigde techniek in chirurgische procedures waarbij botten en protheses correct gepositioneerd dienen te worden. Aan de hand van homologe, opvallende kenmerken op het bot kunnen verscheidene lineaire en angulaire metingen worden uitgevoerd, waarop de chirurg zijn beslissingen baseert gedurende de hele behandelingsprocedure. Naast punten kunnen ook kenmerkende lijnen of zones gedefinieerd worden, die vaak een biologische betekenis hebben. Typische voorbeelden zijn uitsteeksels op het bot, naden tussen botten of aanhechtingszones van ligamenten.

Verschillende types medische beelden kunnen worden gebruikt om referentiepunten en klinisch relevante metingen te bepalen. Traditioneel worden tweedimensionale (2D) radiografische beelden gebruikt, maar deze verschaffen enkel een 2D aanzicht van de anatomie, waarbij de verschillende structuren bovendien overlappen. Via computertomografie (CT) kunnen 2D doorsnedes verkregen worden met hoog contrast voor de botstructuren. Bovendien laat deze techniek toe om driedimensionale (3D) multiplanaire reconstructies en modellen te genereren.

Een aandachtspunt bij het opmeten van de anatomie aan de hand van referentiepunten is dat de manuele lokalisatie van deze punten vaak geassocieerd is met intra- en interwaarnemer variabiliteit. Bovendien kan het bepalen van de punten tijdrovend zijn en is een aanzienlijke ervaring vereist om precieze metingen te bekomen. Automatische methodes om de punten te lokaliseren bieden verschillende voordelen ten opzichte van manuele analyses. Deze technieken laten een snellere analyse van de beelden toe, waardoor de chirurg tijd kan besparen. Door het gebruik van gestandaardiseerde procedures worden intra- en interwaarnemer variaties vermeden, wat kan leiden tot meer precieze metingen, een beter klinisch resultaat en een betere vergelijking van resultaten en uitwisseling van data.

Het doel van deze thesis is om, aan de hand van automatische methodes, referentiepunten en -assen op 3D virtuele modellen van de schedel en femur te bepalen. De punten en metingen zou men respectievelijk kunnen aanwenden voor orthognatische chirurgie en het plaatsen van totale knieprotheses. Orthognatische chirurgie wordt uitgevoerd om één of beide kaaksbeenderen te herpositioneren om zo bijvoorbeeld aanzienlijke afwijkingen tussen de posities van verschillende botonderdelen te corrigeren. De operatie wordt gepland door de dentale, skeletale en faciale verhoudingen in het hoofd op te meten, wat cefalometrische analyse wordt genoemd. Cefalometrie laat ook toe om te evalueren hoe goed de postoperatieve posities van de kaken overeenstemmen met de geplande posities en om de postoperatieve stabiliteit van de botsegmenten te bepalen. Afwijkingen van 2 à 4 mm kunnen reeds klinisch relevant zijn.

Een totale knieprothese (TKP) wordt geplaatst bij degeneratieve artrose van de knie, wanneer andere behandelingen geen oplossing bieden. Tijdens de operatie worden de gewrichtsoppervlakken van de femur (dijbeen) en tibia (scheenbeen) verwijderd en vervangen door een prothese. De uitlijning of het alignement van de protheseonderdelen wordt gepland op basis van verscheidene referentieassen in de knie. Het correct aligneren van de protheseonderdelen wordt beschouwd als een cruciale factor voor het welslagen van de operatie. Een postoperatief verkeerd alignement kan leiden tot het falen van de prothese zowel op korte als op lange termijn en is typisch gedefinieerd als een afwijking van 3° of meer ten opzichte van de beoogde positie.

Driedimensionale computerplanning wordt steeds vaker gebruikt bij deze chirurgische ingrepen. Aan de hand van computertechnieken kan de 3D anatomie gevisualiseerd worden en kunnen verschillende simulaties van de operatie uitgevoerd worden. Bovendien zijn verscheidene technologieën beschikbaar om het preoperatieve plan over te brengen van de computer naar het operatieveld tijdens de ingreep. Hoewel reeds verschillende 3D punten en metingen werden voorgesteld in de literatuur, is er nood aan meer gestandaardiseerde definities en referentiesystemen. Automatische methodes om de referentiepunten op het bot te bepalen kunnen tot een snellere en meer precieze 3D analyse leiden. Dit kan bijdragen tot een verbeterde planning en evaluatie van de chirurgische ingrepen.

Hoofdstuk 2: Overzicht van de literatuur omtrent 3D lokalisatie van referentiepunten

Het is belangrijk om de reproduceerbaarheid van de referentiepunten te bepalen om te evalueren welke metingen met voldoende klinische precisie kunnen uitgevoerd worden en dus een correcte analyse van de patiëntdata toelaten. Verschillende auteurs geven aan dat 2 mm of 2° een mogelijke drempelwaarde is voor klinisch significante verschillen bij het bepalen van cefalometrische punten. In TKP worden referentieassen met variaties van 3° beschouwd als niet betrouwbaar. Dit hoofdstuk vat enkele studies samen omtrent de reproduceerbaarheid van punten en assen bepaald op 3D beelden van het hoofd en de onderste ledematen, en heeft als doel enkele algemene conclusies te trekken omtrent de betrouwbaarheid van verschillende punten en metingen.

De literatuur omtrent de manuele identificatie van referentiepunten toont aan dat intra- en interwaarnemer variaties een beperkende factor kunnen zijn voor het verkrijgen van correcte metingen op basis van 3D medische beelden. Er zijn duidelijke verschillen tussen punten en anatomische richtingen en deze blijken consistent te zijn tussen verschillende studies. Referentiepunten op relatief vlakke of wijd gekromde anatomische structuren vertonen doorgaans een grotere variabiliteit. Toch kunnen precieze metingen verkregen worden op basis van dergelijke punten indien de variatie klein is in de relevante richtingen. Bovendien hangt de betrouwbaarheid van de manuele analyse af van de ervaring van de operator en kan deze verbeterd worden via training of door gedetailleerde definities en anatomische tekeningen te gebruiken. De referentiesystemen die worden voorgesteld in de literatuur zijn meestal gedefinieerd aan de hand van de meest betrouwbare punten. Uit de resultaten voor een set van vaak gebruikte cefalometrische referentiepunten op de schedel wordt afgeleid dat 40 % van de gemiddelde 3D intrawaarnemer waarden groter zijn dan 1.5 mm en dat 52 % van de gemiddelde 3D interwaarnemer waarden groter zijn dat 2 mm. Sommige referentieassen in de knie blijken zeer betrouwbaar te zijn, terwijl voor andere gemiddelde variaties groter dan 2° voorkomen.

Verscheidene (semi-)automatische methodes werden voorgesteld in de literatuur omwille van de nadelen verbonden aan de manuele lokalisatie van referentiepunten. In het tweede deel van dit hoofdstuk wordt de literatuur omtrent automatische lokalisatie op 3D beelden van het hoofd en de onderste ledematen besproken, en worden enkele conclusies omtrent de state-of-the-art getrokken. Bij het gebruik van multiplanaire beelden dienen gelijktijdig de botstructuren geselecteerd te worden en de referentiepunten bepaald te worden. Voor de analyse van de 3D modellen daarentegen dient enkel geometrische informatie verwerkt te worden, maar dit vereist dat de botstructuren reeds werden gesegmenteerd uit de medische beelden.

De literatuur omtrent automatische lokalisatie van referentiepunten toont aan dat volledig geautomatiseerde technieken om de multiplanaire beelden te verwerken, moeilijk te ontwikkelen zijn. De methodes kunnen worden opgedeeld in operatoren op basis van afgeleiden en vervormbare analytische modellen, sjablonen en statistische vormmodellen. Via de automatische aanpak kan de tijd voor manuele interventie gereduceerd worden en de precisie van de punten verbeterd worden. Er werden echter slechts weinig studies gepubliceerd omtrent de schedel en de onderste ledematen. In tegenstelling tot multiplanaire beelden werden reeds verschillende studies over automatische analyse van 3D modellen van de onderste ledematen uitgevoerd. De meest gebruikte methodes zijn het analyseren van de kromming en het fitten van analytische curves en oppervlakken. De meeste publicaties beschrijven echter slechts één of twee technieken of een beperkt aantal geometrische parameters. Het meest uitvoerige werk werd gepubliceerd door twee onderzoeksgroepen: de eerste beschreef methodes om afwijkingen in de onderste ledematen op te meten en de tweede bepaalde verscheidene punten en assen van de femur en het bekken en toonde aan dat de meeste parameters in relatief goede overeenstemming zijn met manuele metingen (<2 mm en 2°). Een volledige set van metingen met betrekking tot het alignement van de femur en tibia ontbreekt echter. In tegenstelling tot de onderste ledematen werden geen automatische methodes voor de lokalisatie van referentiepunten op de virtuele schedel voorgesteld.

Het doel van deze thesis is het ontwikkelen van automatische methodes om referentiepunten en -assen op de 3D virtuele schedel en femur te bepalen, die men respectievelijk zou kunnen aanwenden bij orthognatische chirurgie en TKP. Zoals werd aangetoond in dit hoofdstuk, is het automatisch bepalen van referentiepunten op het 3D model van de schedel een nieuwe aanpak voor 3D cefalometrie. Bovendien worden de huidige beperkingen in de automatische opmeting van het distale alignement van de femur behandeld in deze thesis.

Hoofdstuk 3: Automatische methodes voor het bepalen van 3D referentiepunten

Dit hoofdstuk geeft een overzicht van de algoritmes die in deze thesis worden aangewend om de botten te analyseren. De voornaamste wiskundige achtergrond wordt gegeven en iedere techniek wordt geïllustreerd aan de hand van voorbeelden op de schedel en femur. De algoritmes werden geïmplementeerd aan de hand van de pyFormex software en werden specifiek ontwikkeld voor driehoekige oppervlaktemeshes, het meest voorkomende type van 3D modellen dat wordt gegenereerd uit medische beelden.

Verschillende operaties om een vereenvoudigd of verfijnd model te bekomen of om ruis te verwijderen worden besproken. De vereenvoudigingsmethode van Lindstrom & Turk wordt toegepast om het aantal elementen in het model te reduceren. Ruis en overbodige details worden verwijderd aan de hand van het $\lambda|\mu$ algoritme voorgesteld door Taubin. Het verfijnen van de mesh gebeurt via de subdivisie-techniek van Dyn et al. en Zorin et al., die een gladde interpolatie tussen de oorspronkelijke hoekpunten van het model toelaat. Tenslotte werd een functie geïmplementeerd om de geometrische afstand tussen beide meshes te meten en werd geverifieerd dat de meshoperaties geen grote geometrische fouten introduceren.

Omwille van de verschillende soorten referentiepunten is het vaak aangewezen een combinatie van meerdere technieken te gebruiken om de geometrie van het bot te bestuderen. Daarom werden verschillende methodes geïmplementeerd en getest op de schedel en femur. Zowel convexe, concave als zadelvormige structuren kunnen worden geanalyseerd door extreme punten in vooraf vastgelegde richtingen te bepalen. Bovendien werden methodes geïmplementeerd om de kromming van 3D curves en oppervlakken te berekenen. Terwijl de eerste methode toelaat om punten met lokaal extreme kromming op een curve te bepalen, zijn de krommingswaarden van de oppervlakken moeilijker te verwerken en te herleiden tot één specifiek punt. Het fitten van geometrische objecten laat toe om de anatomische structuren te benaderen door een vooraf gedefinieerde vorm en kan daarom robuuster zijn tegen ruis in het model. Verder kan de kleinste of grootste doorsnede van de mesh berekend worden door een optimaal snijvlak te bepalen. Via het berekenen van de rotationele inertie van de oppervlaktemesh is het mogelijk de hoofdassen van de geometrie te bepalen. Tenslotte werd een algoritme geïmplementeerd om de mesh te projecteren op een vlak en de 2D contour te bepalen.

Hoofdstuk 4: 3D analyse van de schedel

In dit hoofdstuk worden twee studies omtrent de lokalisatie van referentiepunten op de schedel besproken. Eerst wordt een methode voorgesteld om op semi-automatische wijze de punten op de schedel te bepalen. Deze nieuwe techniek laat toe om een zone te selecteren waarin het punt gelegen is, waarna de positie van het punt automatisch berekend wordt. Aangezien vele cefalometrische punten in de literatuur beschreven worden als het verst gelegen in een welbepaalde anatomische richting, werd gekozen om de aanpak van de extreme punten te volgen. De nieuwe methode wordt geëvalueerd door de intra- en interwaarnemer variabiliteit van metingen die worden uitgevoerd op eenzelfde beeld van de schedel te bepalen. Acht van de tien punten vertonen variaties kleiner dan 0.2 mm.

Vervolgens werd verder onderzoek gedaan om de techniek te verbeteren, wat beschreven is in de tweede studie. De intrawaarnemer variabiliteit van metingen die worden uitgevoerd op verschillende beelden van dezelfde schedel wordt bepaald, aangezien de positie van het punt beïnvloed wordt door de precieze discretisatie van de anatomie via de mesh. Bovendien worden de parameters voor het verwijderen van ruis verder bestudeerd. De resultaten worden vergeleken met studies omtrent de manuele lokalisatie van referentiepunten op 3D beelden. De automatische werkwijze laat een precieze lokalisatie van de punten toe. Verschillen tussen punten en anatomische richtingen werden geobserveerd en blijken in overeenstemming te zijn met andere studies. De gemiddelde 3D intrawaarnemer variaties zijn kleiner dan 1.4 mm en de maximale waarden zijn kleiner dan 2 mm voor 11 van de 15 bestudeerde punten. Deze resultaten tonen aan dat de semi-automatische methode een hogere precisie toelaat dan de manuele analyse. Een belangrijk voordeel van de automatische analyse zou het beperken van extreme variaties kunnen zijn. Tenslotte wordt aangetoond dat een betrouwbaar coördinatenstelsel voor cefalometrische analyse kan worden opgesteld op basis van de referentiepunten.

Er kan besloten worden dat de voorgestelde methode vernieuwend is en een meer objectieve en gestandaardiseerde 3D analyse van de schedel toelaat. De automatische analyse kan bijdragen tot een betere 3D planning en evaluatie van orthognatische chirurgie.

Hoofdstuk 5: 3D analyse van de femur

In dit hoofdstuk wordt de femur volledig automatisch geanalyseerd aan de hand van verscheidene algoritmes. In een eerste studie wordt de gekromde anatomische as van de femur berekend door de diafyse te benaderen met een reeks hyperboloïdes. Deze as wordt vervolgens gebruikt om het optimale ingangspunt van de intramedullaire staaf, die tijdens TKP wordt ingebracht in het mergkanaal, te bepalen. Daarnaast wordt nagegaan of een gereduceerd scanprotocol kan gebruikt worden door de methode toe te passen op zowel volledige als gereduceerde modellen van de femur, waarbij de laatste verkregen worden door bepaalde zones uit het model te verwijderen. Precieze metingen kunnen verkregen worden wanneer twee buitenste delen en een centraal deel van de femur wordt gescand. Het toevoegen van het centrale deel is vereist om de buiging van de femur correct te meten.

In een tweede studie worden de verschillende methodes van hoofdstuk 3 toegepast om verscheidene referentieassen te berekenen, die gebruikt worden om het alignement van de femur te meten. Er worden relevante metingen in de drie anatomische vlakken bepaald en de resultaten worden vergeleken met gemiddelde waarden uit de literatuur. Via de automatische methodes kunnen bepaalde assen berekend worden die manueel moeilijk te bepalen zijn. Hoewel de gemiddelde waarden van de meeste metingen in overeenstemming zijn met andere studies, is verder werk noodzakelijk om de automatische procedure te valideren.

De voorgestelde technieken vormen een basis voor een meer objectieve en gestandaardiseerde 3D analyse van het alignement van de femur. De automatische analyse kan bijdragen tot een snellere en preciezere 3D planning en evaluatie van TKP.

Hoofdstuk 6: Conclusies en perspectieven

Dit hoofdstuk geeft een overzicht van de belangrijkste verwezenlijkingen van de thesis met betrekking tot het lokaliseren van 3D referentiepunten en -assen. Daarnaast worden enkele suggesties voor verder onderzoek geformuleerd. Het doel van deze thesis was het ontwikkelen van automatische methodes om referentiepunten en -assen te bepalen die aangewend worden voor orthognatische chirurgie en TKP. Een nieuwe semi-automatische methode om referentiepunten op de virtuele schedel te lokaliseren en een uitgebreide set van functies om het alignement van de femur op te meten, werden voorgesteld. Definities werden aangepast naar de drie dimensies, wiskundige beschrijvingen en referentiesystemen werden voorgesteld en de methodes werden geëvalueerd aan de hand van verschillende technieken. De automatische aanpak zou kunnen bijdragen tot een snellere en objectievere analyse van de patiëntdata, maar verder onderzoek is nodig om de resultaten nog beter te evalueren en om de methodes aan te wenden voor klinische toepassingen. Met betrekking tot cefalometrie werden reeds verscheidene referentiepunten op de schedel bepaald, maar moet de semi-automatische procedure aangewend worden om ook de punten op de kaken, tanden en het aangezicht te bepalen. Bovendien moeten betrouwbare metingen voor de cefalometrische analyse voorgesteld worden op basis van deze punten. Met betrekking tot TKP moeten relevante metingen voor de planning en evaluatie van de operatie bepaald worden en moet het alignement van de tibia en de protheseonderdelen bestudeerd worden. Tenslotte wordt ook aangetoond dat de technieken kunnen gebruikt worden voor vele andere toepassingen, zowel in medische als andere onderzoeksdomeinen.

Summary

Chapter 1: Introduction

Landmark-based measurement is a well-established technique in surgical procedures requiring correct positioning of bones and prostheses. From homologous, prominent features on the bones various linear and angular measurements can be derived, which aid the surgeon in decision making throughout the whole patient treatment process. Landmarks can be isolated points, lines or regions and often have a biological meaning. Typical examples are a prominence on the bone, a suture between bones or an insertion site of ligaments.

Several types of medical images are used to obtain landmark coordinates and clinically relevant measurements. Two-dimensional (2D) radiographs are most commonly employed, but only provide a 2D representation of the anatomy, with the structures being superimposed onto each other. Computed tomography (CT) produces cross-sectional images with high contrast for the bony structures. Furthermore, three-dimensional (3D) multiplanar reconstructions and models can be generated from the slices.

An important issue in landmark-based measurement is that the manual localisation of landmarks is prone to intra- and interobserver variations. Moreover, precise landmark identification is time-consuming and requires a high level of experience. Automatic approaches to localise the landmarks offer several advantages over manual analysis. They allow for a faster analysis and could thus save time for the surgeon. Observer variability is eliminated by using standardised procedures, which could result in more reliable measurements and improved clinical outcome, result comparison and data exchange.

This thesis aims at developing automatic approaches to extract reference points and axes from 3D virtual models of the skull and femur. The studied landmarks and measurements could be applied for orthognathic surgery and total knee arthroplasty, respectively. Orthognathic surgery is a procedure in which one or both jaws are repositioned, for example to correct significant skeletal discrepancies. The surgical movements are planned by measuring the dental, skeletal and soft tissue relationships in the head, which is called cephalometric analysis. In addition, cephalometry can be used to evaluate how well the planned jaw positions were reached during the operation and to assess the postsurgical stability of the bone segments. Deviations in the range of 2-4 mm can already be considered potentially clinically significant.

Total knee arthroplasty (TKA) is a surgical procedure to treat end stage osteoarthritis of the knee. During surgery the articular surfaces of the femur (thighbone) and tibia (shinbone) are removed and replaced by a prosthesis. The alignment of the prosthesis components is planned based on various reference axes in the knee. It has been demonstrated that correct alignment of the prosthesis components is a crucial factor for the success of TKA. Postoperative malalignment has been associated with failure on short as well as long term and is typically defined as a deviation of 3° or more from the targeted position.

An increased interest for 3D computer-assisted planning is shown for both of these procedures, as it allows for visualising the 3D anatomy of the bones and simulating different surgical procedures. Moreover, several technologies can aid in transferring the preoperative plan from the computer to the operating room. Different 3D landmarks and measurements have been proposed, but there is still a lack of standardised definitions and reference systems. Automatic approaches to identify the landmarks on the virtual bone model could speed up and increase the precision of the 3D analysis. This could contribute to an improved planning as well as evaluation of the surgical procedure.

Chapter 2: Literature review on 3D landmark localisation

The reliability of landmarks should be measured to determine which measurements are clinically acceptable and thus allow for correct analysis of the patient data. Several authors suggested that 2 mm or 2° provides a potential threshold for clinically meaningful differences in cephalometric landmark identification. In TKA, reference axes with observer variations approaching 3° can not be considered as reliable landmarks. This chapter summarises some of the studies reporting on the reliability of landmark identification on 3D images of the head and lower limbs and aims at drawing some conclusions about the reliability of different landmarks and measurements.

The literature review on manual landmark localisation demonstrates that intra- and interobserver variability can be a limiting factor for obtaining correct measurements from 3D medical images. Differences between landmarks and anatomical directions are found and seem to be consistent among different studies. Landmarks located on relatively flat or widely curved anatomical structures and short axes are more prone to observer variability. However, precise measurements can also be obtained based on these points if the variations are small in the relevant directions. Furthermore, the reliability of manual landmark localisation may depend on the experience of the operator and might be improved through training and by using detailed landmark definitions and anatomical drawings. Finally, the reference frames proposed in literature are usually defined from the most reliable landmarks or landmark directions. By summarising the results for a set of commonly used skeletal cephalometric points it is found that 40 % of the mean 3D intraobserver values are above 1.5 mm and that 52 % of the mean 3D interobserver values are greater than 2 mm. Some of the axes of the knee were found to be very reliable, while other showed mean variations above 2°.

Because of the disadvantages associated with manual landmark localisation, several (semi-)automatic approaches have been presented in literature. In the second part of this chapter, the literature on automatic landmark localisation on 3D images of the head and lower limbs is reviewed, and some conclusions about the current state-of-the-art are drawn. When using multiplanar images, both the selection of the bony structures and landmark extraction need to be performed at the same time. For the 3D models, only geometrical information needs to be processed, but this requires that the bony anatomy is already segmented from the medical images.

By reviewing the literature on automatic landmark localisation, it is seen that fully automatic approaches to process 3D multiplanar images are hard to develop. The methods can be grouped into differential operators and deformable analytical, template and statistical shape models. The automatic approaches seem to reduce the time spent for manual intervention and improve the landmark localisation precision. However, the amount of work published on the skull and lower limb bones is very limited. In contrast to multiplanar images, several studies on automatic analysis of 3D models of the lower limbs have been published. The most commonly used methods are curvature analysis and analytical curve and surface fitting. However, most papers describe only one or two techniques or extract only a limited amount of geometrical parameters. The most extensive work has been performed by two research groups: one presented methods for automatically measuring lower limb deformities and the other extracted several points and axes on the femur and pelvis and showed that most of the parameters were relatively close to the manual measurements ($<$2 mm and 2°). However, a complete set of measurements of femoral and tibial alignment has not yet been presented. In contrast to the lower limbs, no automatic approaches for landmark localisation on the virtual skull model have been proposed.

This thesis aims at developing automatic approaches to extract reference points and axes from the 3D virtual skull and femur, which could be used in orthognathic surgery and TKA, respectively. As shown in this chapter, extracting landmarks from the 3D model of the skull is a novel approach for 3D cephalometry. Moreover, the current limitations in the automatic measurement of distal femoral alignment are addressed in this thesis.

Chapter 3: Automatic approaches to 3D landmark extraction

This chapter provides an overview of the algorithms that are used in this thesis to analyse the bone models. The main mathematical background is given and each method is illustrated using examples on the skull and femur models. The algorithms are implemented using the pyFormex software and are developed for triangulated surface meshes, the most common type of 3D models that are obtained from medical images.

Several operations to obtain a simplified, refined or smoothed approximation of the original surface mesh are discussed. The simplification method proposed by Lindstrom & Turk is applied to reduce the model size. Using Taubin's $\lambda|\mu$ algorithm, the models are smoothed to remove noise and useless details. The subdivision technique of Dyn et al. and Zorin et al. was implemented to smoothly refine the mesh. Finally, a tool to quantify the geometric difference between the meshes was implemented and it was verified that the mesh operations can be performed without introducing large geometrical errors.

Because of the many different types of landmark definitions found in literature, the combination of multiple landmark extraction techniques is often desired for a complete 3D analysis of the bone geometry. Therefore, different methods were implemented and tested on the skull and femur. Convex-, concave- as well as saddle-shaped structures can be processed to detect the extreme points in predefined directions. Also, methods for curvature analysis of 3D curves and surfaces were implemented. While the first method allows for extracting points of local extreme curvature on a curve, the surface curvature values are more difficult to process and to reduce to one particular point. Geometrical entity fitting could be more robust to noise as it allows to approximate the anatomical structures with several predefined shapes. Furthermore, the smallest or largest cross-section of the mesh can be computed by searching for an optimal slicing plane. Another method is to use the rotational inertia characteristics of the surface mesh to extract the principal axes of the geometry. Finally, a 2D projection algorithm was implemented to create a 2D contour from the 3D surface mesh.

Chapter 4: 3D analysis of the skull

In this chapter, two studies about landmark localisation on the skull are presented. First, a method for semi-automatic localisation of landmarks on the virtual skull is proposed. This novel approach allows the user to select a region-of-interest in which the landmark is located and the position of the point is then determined automatically. It was chosen lo localise the landmarks using the extreme point technique, as many cephalometric points have been described in this way. The new approach is evaluated by assessing the intra- and interobserver variability for measurements performed on one image of each skull. Observer variations below 0.2 mm were found for eight out of ten landmarks.

Further research was done to improve the technique, as described in the second study. The intraobserver variability for measurements performed on different images of the same skull is obtained, as the landmark position may change if the anatomy is discretised in a different way. In addition, the effect of using different smoothing parameters is investigated. The results are compared to studies reporting on manual landmark localisation on 3D images. The automatic approach allows for precise landmark localisation. Differences in precision between landmarks and anatomical directions were observed and were in agreement with other studies. The mean 3D intraobserver variations are below 1.4 mm and the maximum variations are below 2 mm for 11 of the 15 studied landmarks. These results show that the semi-automatic approach allows for an improvement in landmark precision compared to the manual analysis. A major advantage of the automatic analysis might be that it is less prone to outlier variations. Finally, it is demonstrated that a reliable coordinate system for cephalometric analysis can be set up from the studied landmarks.

Overall, the proposed method is novel and allows for a more objective and standardised 3D analysis of the skull. The automatic analysis can contribute to an improved 3D surgical planning as well as evaluation of orthognathic surgery.

Chapter 5: 3D analysis of the femur

The femur is fully automatically analysed in this chapter using a variety of landmark extraction techniques. In a first study, the 3D femoral anatomical axis is extracted from a series of best-fit hyperboloids to the shaft. This axis is then used to determine the optimal entry point for the intramedullary rod, which is inserted into the medullary canal during TKA. In addition, the feasibility of a reduced scanning protocol is investigated by applying the method on both full and reduced models of the femur, the latter being obtained by removing specific regions from the model. Precise measurements can be obtained by scanning two outer and a central part of the femur. Including the central part of the femur is required to correctly measure femoral bowing.

In a second study, various reference axes to study femoral alignment are automatically determined by applying the different feature extraction methods presented in chapter 3. Relevant angular measurements in the three anatomical planes are made and compared to mean values reported in literature. It is shown that the automatic methods allow for determining axes that are difficult to identify manually. While the mean values for most measurements are in agreement with other studies, further work is required to validate the automatic procedure.

The presented techniques form a basis for a more objective and standardised 3D analysis of femoral alignment. The automatic analysis can contribute to a faster and more precise 3D planning and evaluation of TKA.

Chapter 6: Conclusions and perspectives

This chapter gives an overview of the main contributions of this work to the field of 3D landmarks and offers some suggestions for further research. This thesis aimed at developing automatic approaches to extract reference points and axes that could be used for orthognathic surgery and TKA. A novel semi-automatic approach for landmark localisation on the virtual skull was proposed and an extensive set of tools to measure femoral alignment was presented. Landmark definitions were adapted to include the three dimensions, mathematical descriptions and reference frames were proposed and the methods were evaluated using different techniques. The automatic techniques may save time for the surgeon and allow for a more objective analysis of patient data, but further work is needed to evaluate the results and to employ the methods for clinical applications. Regarding cephalometry, several landmarks of the skull have been extracted, but the semi-automatic procedure should be employed to also detect the landmarks on the jaws, teeth and face. Furthermore, reliable measurements for cephalometric analysis should be proposed based on these landmarks. Concerning TKA, relevant measurements for planning and evaluation of surgery should be determined and the alignment of the tibia and prosthesis components should be studied. Finally, it is illustrated that the techniques could be used for many other applications, both within or outside the medical field.

1 Introduction

1.1 Motivation

Landmark-based measurement is a well-established technique in surgical procedures requiring correct positioning of bones and prostheses. From homologous, prominent features on the bones various axes, planes, sizes and linear and angular measurements can be derived, which aid the surgeon in decision making throughout the whole patient treatment process: diagnosis of the pathological anatomy, surgical planning, restoration of normal anatomy, positioning of surgical instruments and postoperative follow-up.

Due to the subjective perception of human operators, each attempt of one or different observers to identify a specific landmark may result in slightly different coordinates. Even when high quality images are used and clear definitions are provided for the landmarks, intra- and interobserver variabilities occur. Precise landmark identification is also time-consuming and requires a high level of experience. To allow for good clinical outcome, however, the variability of the landmark coordinates and corresponding measurements should be in the clinically acceptable range. In addition, patient data, such as pre- and postoperative images, can only be compared in a reliable way if the morphological measurements are obtained with sufficient precision. Computer-assisted methods can be used to aid the operator in landmark identification, e.g. by creating intersections or fitting geometrical shapes. While these might allow slight improvement in precision and analysis time, the disadvantages of the manual procedure remain.

Automatic approaches to localise the landmarks offer several advantages over manual analysis. They allow for a faster analysis and could thus save time for the surgeon. In addition, rapid data processing is of interest for obtaining morphological measurements of large control and patient populations. They can be applied to gain additional insights in different pathological morphologies and to compare the results of different surgical procedures. Observer variability is eliminated by using standardised procedures, which could result in more reliable measurements and improved clinical outcome, result comparison and data exchange.

This thesis aims at developing automatic approaches to extract anatomical landmarks from three-dimensional (3D) virtual models of the skull and femur. The studied landmarks and measurement could be applied for orthognathic surgery and total knee arthroplasty, respectively. An increased interest for 3D computer-assisted planning is shown for both of these procedures, due to difficulties associated with the two-dimensional (2D) approach and easier transfer of the 3D preoperative plan to the operating room and due to advances in 3D imaging, image processing and computer technology.

This chapter first gives a brief introduction to the use of bony anatomical landmarks and medical images. Then, the anatomical terminology is illustrated and validation terms are explained. Next, the two surgical procedures considered in this thesis are discussed: orthognathic surgery and total knee arthroplasty. The conventional landmark-based 2D measurement method is explained and the current trend towards 3D analysis is demonstrated. Some remarks about 3D automatic landmark extraction are given and finally, the outline of the thesis is described.

1.2 Anatomical landmarks

Anatomical landmarks are prominent features that establish an unambiguous correspondence among specimens. They can be isolated points, lines or regions and often have a biological meaning. Typical examples are a prominence on the bone, a suture between bones, an insertion site of muscles or ligaments or an axis around which a bone rotates. They are often defined based on a geometrical description, i.e. using shape, size and relative position. Because their positions are homologous among specimens, they can be used to determine relevant axes, planes, sizes and linear and angular measurements. Bony landmarks can be both identified on the skin or underlying bone through manual palpation and digitised using a probe or on medical images through virtual, either manual or automatic, palpation. Manual palpation on the body is often performed during surgery, e.g. to position an implant or surgical instrument, or before in-vivo kinematic analysis to place markers on the body. In addition, functional methods can be used to estimate the centre of rotation of a ball-and-socket joint from kinematic data. Landmarks obtained from medical images, which allow to view the inner structures of the body, are primarily used for diagnosis, surgery planning and treatment evaluation.

Bony landmarks are employed for various reasons in medicine. Many morphological parameters (e.g. distances, angles, sizes) have been defined based on landmarks to describe the geometry of anatomical parts [1–3]. A reference set of measurement values obtained from normal anatomies can be used to diagnose pathological cases [4] and to restore the anatomy [5]. Joint prostheses are often positioned with respect to certain anatomical reference axes and various recommendations for the orientation angles have been presented [6]. Also, joint kinematics are often described relative to joint coordinate systems that are defined based on anatomical landmarks [7]. Another application is landmark-based image registration, which uses the locations of corresponding landmarks to determine the geometric transformation between images [8]. This allows for example to superimpose images of a patient obtained with different imaging modalities or at different times. In image-based navigation, patient-to-image registration can be performed using landmarks that are determined on the image as well as on the patient during the operation [9]. Furthermore, different landmarks can be used to determine the insertion locations in ligament reconstruction [10, 11]. Finally, statistical shape models, representing the mean shape and modes of shape variation of a specific anatomical part, can be built from a set of corresponding landmarks in the training shapes [12].

An important issue in landmark-based measurement is the use of standardised definitions. It has been shown that the use of more anatomically detailed landmark definitions [13] increase their localisation reproducibility [14]. Also, standardised patient positioning during 2D image acquisition is required as the resulting measurements can be significantly affected by variabilities in orientation of the anatomical part [15, 16]. Differences in the choice of reference frame and in the definition of orientation angles may lead to inconsistencies in the recommendations for correct positioning of joint prostheses [6]. Quantifications of how different coordinate systems produce different outputs for joint motion [17] also reveal the need for using standardised definitions and recommendations on the definitions of joint coordinate system of various joints have been presented [18, 19]. Automatic approaches for landmark localisation may contribute to improved standardisation by employing unambiguous definitions.

1.3 Medical images

Several types of medical images can be used to obtain landmark coordinates and clinically relevant measurements (see Figure 1.1). Two-dimensional radiography is the most commonly used imaging technique for deriving landmark-based measurements. A disadvantage of these images is that they provide a 2D representation in which the anatomical structures are superimposed onto each other. The analysis of asymmetrical anatomies, for which bilateral structures are not superimposed, might therefore be more difficult and thus prone to error. The presence of large deformities might also hamper radiographic analysis because traditional measurements might not suffice. The imaged plane and consequently the obtained measurements may also vary if the anatomical part is oriented differently during imaging [20]. In addition, magnification and distortion errors occur depending on the distances between the X-ray source, the patient and the film [21]. Multiplanar images (e.g. a frontal and lateral radiograph) can be used to obtain 3D measurements [22], but these require that the landmarks are visible on both images and that the difference in magnification of the various anatomical structures is corrected.

More detailed, cross-sectional images are provided by computed tomography (CT) and magnetic resonance (MRI) imaging. In addition, software programs allow to generate 3D multiplanar reconstructions and surface renderings or models from the 2D slices. These allow to view the 3D anatomical structures from different angles and can provide additional useful information for patient treatment. While MRI is most adequate for visualising soft tissues, CT is preferred to obtain high contrast images of the bone structures. Combined techniques may also be used, such as arthro-CT, which uses a contrast agent to obtain a better view of the cartilage. Both radiography and CT imaging expose the patient to X-ray radiation, but the effective dose is considerably larger for the latter. Because of radiation issues and higher cost, CT imaging is currently mainly used to treat patients with more complex anatomies, such as asymmetrical cases or large deformities. However, an increasing amount of studies is ongoing on how radiation dose can be reduced without compromising the image quality [23, 24]. In particular, new software technologies [25, 26] and individual settings adjusted to the body type and to the anatomical part that is imaged [27] allow for low-dose CT scanning. Reduced radiation dose will likely result in a more widespread use of this technology for cases where improved outcome is expected or has been proven.

The medical images used for landmark localisation can thus be classified into four types with regards to their dimensions and to how the information is stored in the image: 2D projections, 2D slices, 3D multiplanar reconstructions and 3D models. Two-dimensional images, both projections and slices, display the object using pixel intensity values, usually grayscale values. The image's signal (the intensity function) is a function of the position values (the pixels). Similarly, 3D multiplanar reconstructions contain voxel information: an intensity function is defined over the 3D voxel positions. In 3D models, however, the information is stored in a different way as the signal's values are the positions themselves. This is a direct result of the additional segmentation step that is performed before generating the 3D model.

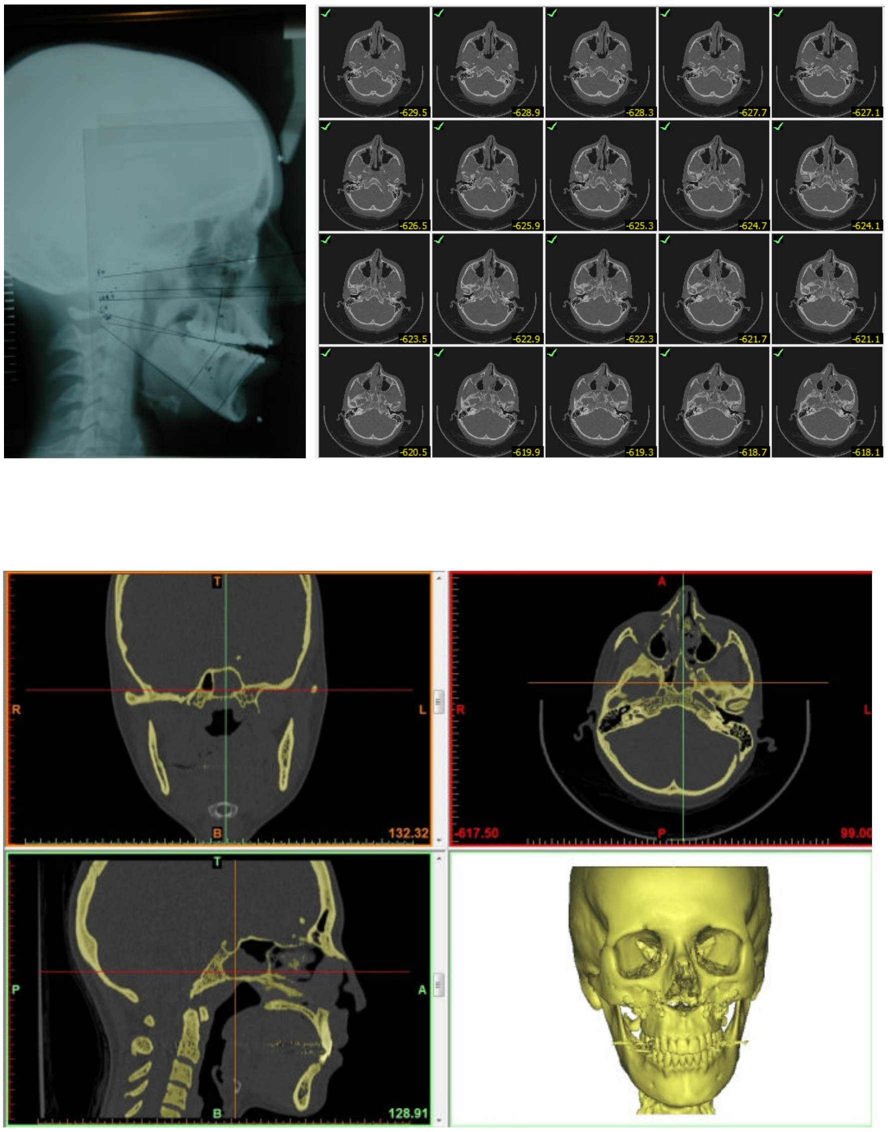

Figure 1.1: Different types of medical images: 2D radiograph (top left), set of 2D axial CT slices (top right), 3D multiplanar reconstruction showing coronal, axial and sagittal slices (bottom) and 3D model (bottom).

1.4 Terminology

Anatomical directional terms and planes of reference are employed throughout the thesis to indicate the locations of anatomical structures and landmarks and to define the reference frames. These are illustrated in Figures 1.2 and 1.3.

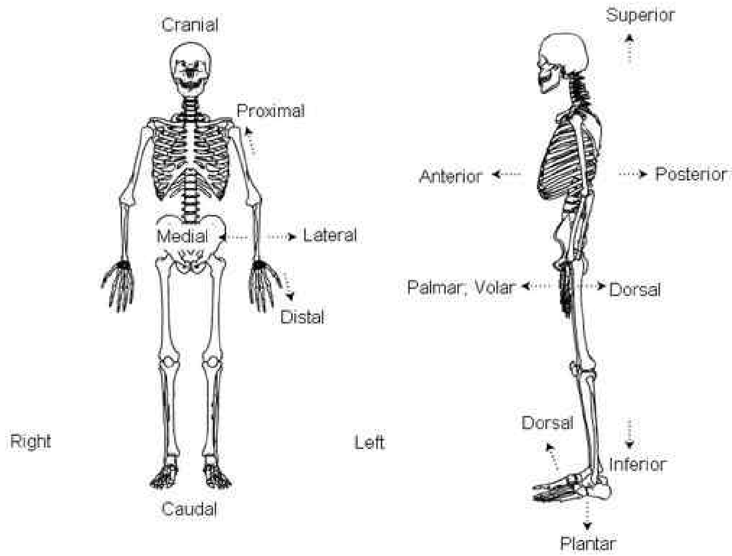

Figure 1.2: Anatomical directions [28].

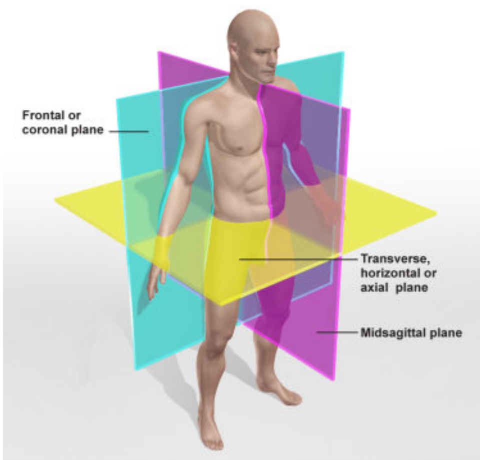

Figure 1.3: Anatomical planes [29].

Furthermore, the macroscopic anatomy of the studied bones is given in this section. Figures 1.4 to 1.7 give an overview of the skull bones and their main anatomical structures. The skull is composed of 28 bones: 8 cranial bones protecting the brain, 14 facial bones supporting the face and 6 ear ossicles.

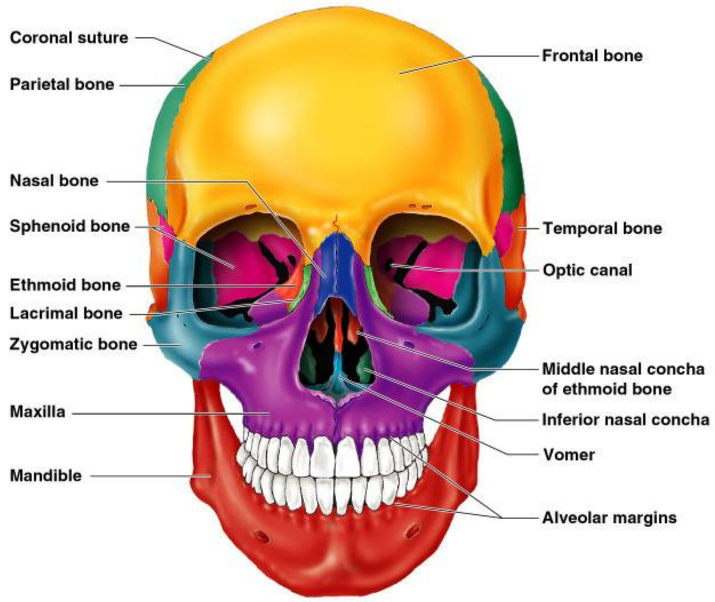

Figure 1.4: Anatomical structures in the skull: anterior view [30].

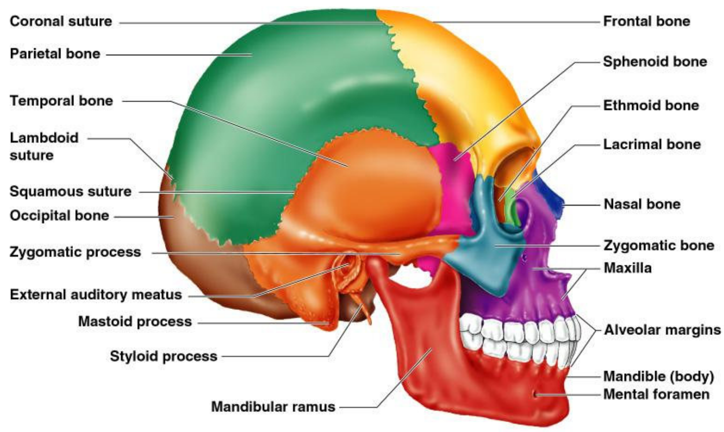

Figure 1.5: Anatomical structures in the skull: right view [30].

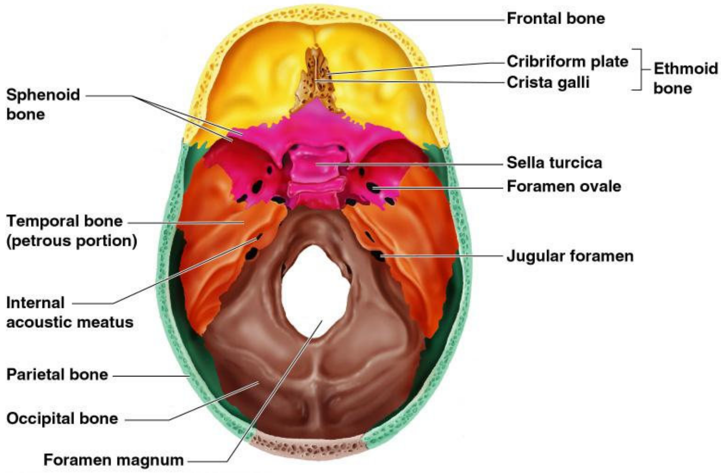

Figure 1.6: Anatomical structures in the skull: intracranial superior view [30].

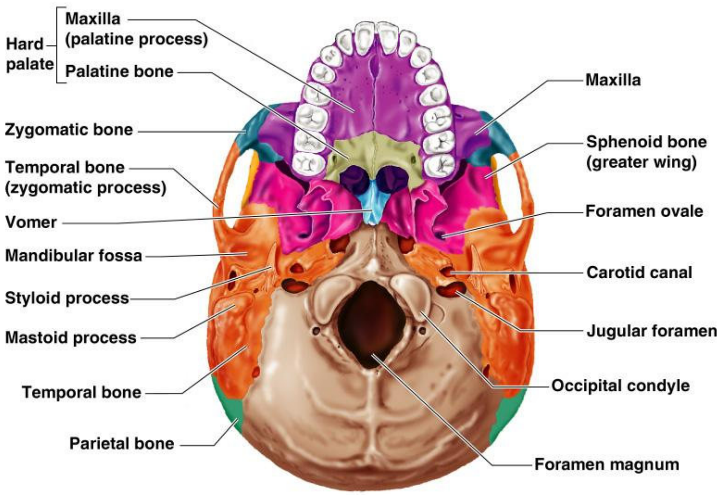

Figure 1.7: Anatomical structures in the skull: inferior view [30].

Figure 1.8 gives an overview of the 31 bones that are found in each lower limb: the hip bone, femur, patella, tibia, fibula, 7 tarsal bones, 5 metatarsals and 14 phalanges. The hip bone, which is illustrated in Figure 1.9, is formed by the union of three bones at the acetabulum: the ilium, the pubis and the ischium. The femur and tibia are shown in Figure 1.10.

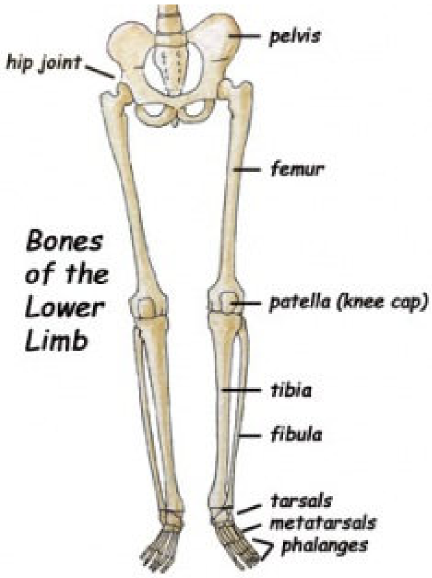

Figure 1.8: Bones of the lower limbs: anterior view [28].

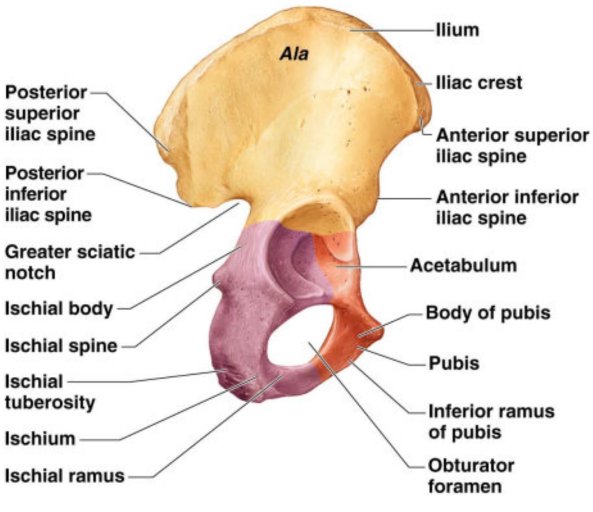

Figure 1.9: Anatomical structures in the hip bone: anterolateral view [30].

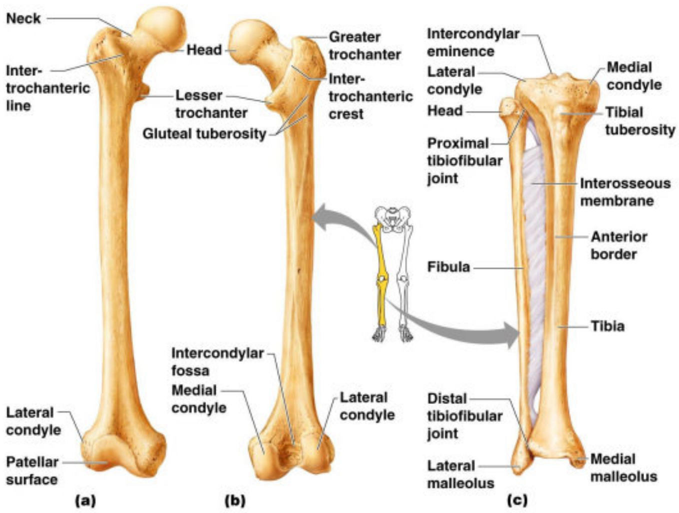

Figure 1.10: Anatomical structures in the leg: (a) anterior view of the femur, (b) posterior view of the femur, (c) anterior view of the tibia [30].

Finally, some terminology on validation of the measurements should be explained. The most adequate method to validate the position of the landmarks is to assess the accuracy of the measurements. Accuracy refers to a combination of trueness and precision, with the latter one being defined in terms of repeatability or reproducibility. These terms can be described as follows:

- Accuracy/validity: the closeness of agreement between a measurement result and the true value or an accepted reference value;
  - Trueness: the closeness of agreement between the average value obtained from a large series of measurement results and the true value or an accepted reference value;
  - Precision/reliability: the closeness of agreement between independent measurement results obtained under stipulated conditions;
    * Repeatability: the closeness of agreement between independent measurement results obtained with the same method on identical test material, under the same conditions (same operator, same apparatus, same laboratory and after short intervals of time);
    * Reproducibility: the closeness of agreement between independent measurement results obtained with the same method on identical test material, but under different conditions (different operators, different apparatus, different laboratories and/or after longer intervals of time).

The difference between accuracy, trueness and precision is illustrated in Figure 1.11 using the analogy of arrows that are shot at a target. The accuracy or closeness of an individual test result to the accepted reference value, which is indicated by the centre of the target, improves with increasing precision and increasing trueness and therefore is a measure of both of these validation parameters [32].

Measurement errors can be split into two components: systematic errors or biases and random errors. Systematic errors are constant, while random errors are caused by unknown and unpredictable variations in the experiment. Trueness and precision are limited by systematic and random errors, respectively.

Two commonly used variables to express the precision of the landmark positions are intra- and interobserver reproducibility. These terms refer to the closeness of agreement between measurement results obtained by one observer after relatively long intervals of time (e.g. more than one day) and measurement results obtained by multiple observers, respectively. The main goal of this thesis is to employ automatic landmark localisation methods to improve the precision of the 3D analysis of the bones.

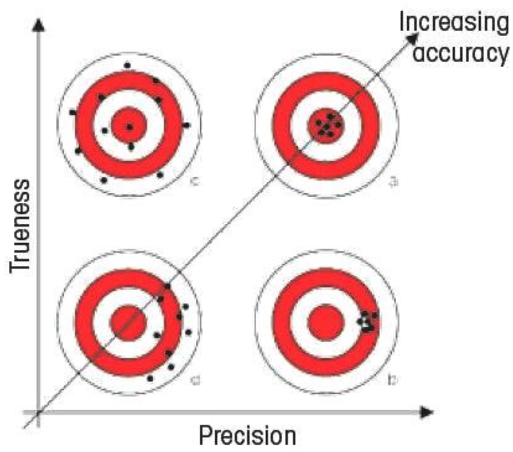

Figure 1.11: Illustration of accuracy, trueness and precision using the analogy of arrows that are shot at a target. The accuracy improves with increasing precision and increasing trueness [31].

1.5 Orthognathic surgery

Orthognathic surgery is a procedure performed to reposition one or both jaws. During surgery, the maxilla (upper jaw) is cut loose from the skull and is usually repositioned relative to the mandible (lower jaw), while the mandible is usually split at the left and right ascending rami and repositioned relative to the moved maxilla, or vice versa. After the bones are realigned, they are held in place with plates and/or screws. The main indications for orthognathic surgery are significant skeletal discrepancies, temporomandibular joint pathology and obstructive sleep apnea [33–35]. Traditionally, the procedure is planned using photographs, lateral and/or frontal radiographs and plaster dental casts as well as bite registrations establishing the antagonistic tooth contacts in generally habitual occlusion, i.e. when the teeth in both jaws are brought into maximum contact. A double jaw surgery is generally planned in the following way. The new position and corresponding movements of the maxilla relative to the skull are determined from the clinical examination, photographs and radiographs and are based on esthetical, anatomical and functional norms. The dental casts are mounted onto an articulator in their correct anatomical positions using a face-bow and a bite impression. The face-bow records the position of the maxilla relative to the skull and is used to orient the maxillary cast in the articulator, while the bite impression records the patient's occlusion and is used to orient the mandibular cast in the articulator. The planned movements are then transferred to the articulator by separating the maxillary cast from its base and moving it to the new position. Next, the mandibular cast is separated from its base and moved to its new position by determining the optimal occlusion between the two dental arches. To position the jaws during surgery, two acrylic temporary splints are fabricated: an intermediate splint to simulate the new position of the maxilla relative to the original position of the mandible and a final splint to simulate the new position of the mandible relative to the moved maxilla. Figure 1.14 shows the splints in case of computer-assisted planning.

The radiographic analysis is based on various landmarks and measurements that allow to determine the relationships between the teeth, bones and soft tissues. The study of the dental, skeletal and soft tissue relationships in the head is named cephalometric analysis. Cephalometry was introduced by Broadbent [36] and Hofrath [37] in 1931 by the development of the cephalostat, a head-positioning device to obtain more standardised lateral and frontal views of the skull. Since then, it is a widely used measurement tool for diagnosis, treatment planning and evaluation of dentofacial disharmonies. Several types of analyses have been presented to relate the cranial and facial bones and teeth with each other [2, 3]. Figure 1.12 gives an overview of commonly used hard tissue landmarks. Figure 1.13 shows two common types of analyses. Among other measures, the Downs analysis uses the facial angle (N-Pg to FH), angle of convexity (N-A-Pg) and A-B plane angle (A-B to N-Pg) to describe the positions of the maxilla and mandible relative to the Frankfort horizontal plane (Po-Or). In the Steiner analysis, the SNA and SNB angles relate the horizontal position of the maxilla and mandible to the cranial base. The ANB angle describes the relationship between the maxilla and mandible [2].

Besides planning, cephalometry can be used to evaluate the outcome of the surgical procedure. Postoperative images can be analysed to evaluate how well the planned jaw positions were reached during the operation. In addition, short- and long-term postsurgical stability of the bone segments can be assessed. Instability or relapse may occur due to several factors such as inadequate mobilization of

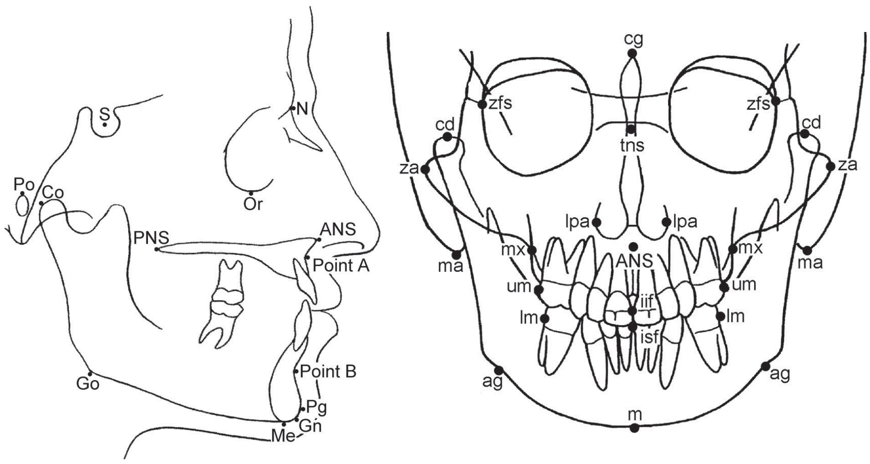

Figure 1.12: Landmarks commonly used in the analysis of the skull: lateral view (left) and frontal view (right) [2] (abbreviations are explained in Table 1.1).

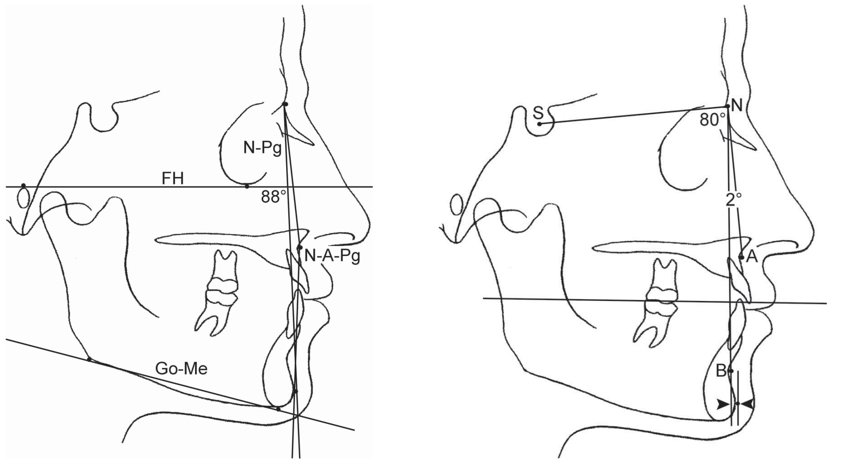

Figure 1.13: Cephalometric analysis based on a lateral radiograph: Downs analysis (left) and Steiner analysis (right) [2] (abbreviations are explained in Table 1.1).

the repositioned jaws, improper positioning of the condyles in the fossa, muscular forces and bone resorption [38, 39]. The amount of relapse varies largely by the direction of surgical movement. Proffit et al. [40] presented a hierarchy of stability for orthognathic surgery with rigid fixation and reported that isolated mandibular setback, downward movement of the maxilla and widening of the maxilla are the least stable procedures within one year after surgery. They considered changes below 2 mm to be within the range of method error and clinically insignificant, 2-4 mm outside the range of method error and potentially clinically significant and above 4 mm as often beyond the range of orthodontic compensation and clinically highly significant. Similarly, according to Lagravère et al. [41] it is reasonable that mean differences in landmark identification less than 1 mm are clinically acceptable, that mean differences between 1 and 2 mm are useful in most analyses, and that landmarks with mean differences greater than 2 mm should be used with caution. While there is no general accepted standard for the maximum allowable error, many authors suggest that 2 mm or 2° provides a potential threshold for clinically meaningful differences, because these are generally within one standard deviation of norm values of most of the cephalometric analyses, are not likely to be noticeable to the naked eye or will probably not make a difference in treatment [42–46].

Because of the difficulties associated with developing a 3D surgical plan based on the 2D cephalograms and 3D dental casts that do not visualise the jawbones, 3D computer-assisted planning is more and more performed [47–49]. In contrast to the traditional approach, this virtual environment allows the surgeon to view the 3D anatomy of the teeth, bones and soft tissues and simulate different surgical procedures and setups. As shown in Figure 1.14, the jaws can be virtually cut and repositioned and surgical splints can be fabricated from the virtual occlusion allowing to transfer the treatment plan and occlusal characteristics to the operation table. As an alternative, surgical navigation has been used to position the jaws according to the preoperative plan [50]. This technique allows tracking and displaying of the anatomy and surgical instruments on a computer screen by

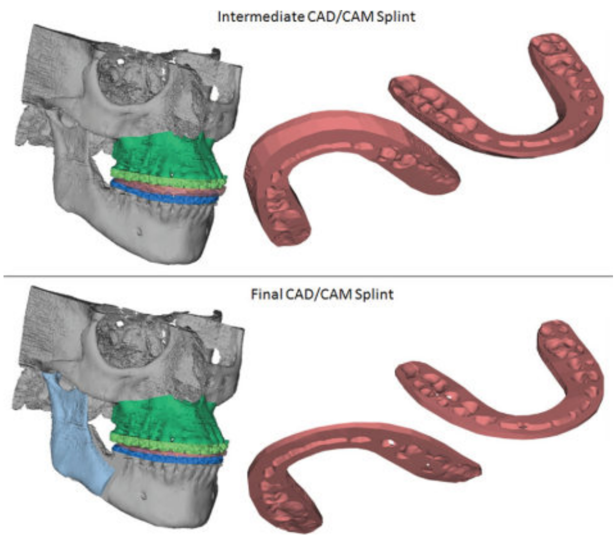

Figure 1.14: Computer-assisted planning of orthognathic surgery: two surgical splints are fabricated from the virtual treatment plan, which relate the new position of the maxilla to the original position of the mandible (top) and the new position of the mandible to the moved maxilla (bottom) [49].

registering the preoperative image to the patient's anatomy during surgery. It has the advantage that the maxilla does not need to be moved relative to the mandible, which is not fixed in relation to the skull.

As for the 2D cephalometric analyis, different 3D landmarks and measurements have been proposed [13, 51–53]. Table 1.1 gives an overview of 3D landmark definitions proposed by Swennen et al. [51]. Automatic approaches to identify the landmarks on the virtual skull model could speed up and improve the precision of the 3D analysis. They could contribute to an improved surgical planning as well as evaluation of the procedure, which requires quantifying deviations in the order of 2 mm.

Table 1.1: Landmarks commonly used in the analysis of the skull and their 3D definition as proposed by Swennen et al. [51] (abbreviations according to Figure 1.12).

Landmark	3D definition
Anterior nasal spine (ANS)	Most anterior midpoint of the anterior nasal spine of the maxilla
A-point (A)	Point of maximum concavity in the midline of the alveolar process of the maxilla
Basion (Ba)	Most anterior point of the great foramen (foramen magnum)
B-point (B)	Point of maximum concavity in the midline of the alveolar process of the mandible
Condylion left/right (Co)	Most postero-superior point of each mandibular condyle in the sagittal plane
Frontozygomatic Point (Zfs)	Most medial and anterior point of each frontozygomatic suture at the level of the lateral orbital rim
Gnathion (Gn)	Most anterior and inferior midpoint of the chin on the outline of the mandibular symphysis
Gonion left/right (Go)	Point at each mandibular angle that is defined by dropping a perpendicular from the intersection point of the tangent lines to the posterior margin of the mandibular vertical ramus and inferior margin of the mandibular body or horizontal ramus
Menton (Me)	Most inferior midpoint of the chin on the outline of the mandibular symphysis
Nasion (N)	Midpoint of the frontonasal suture
Orbitale left/right (Or)	Most inferior point of each infraorbital rim
Pogonion (Pg)	Most anterior midpoint of the chin on the outline of the mandibular symphysis
Porion left/right (Po)	Most superior point of each external auditory meatus
Posterior nasal spine (PNS)	Most posterior midpoint of the posterior nasal spine of the palatine bone
Sella (S)	Centre of the sella turcica
Zygion left/right (Za)	Most lateral point on the outline of each zygomatic arch

1.6 Total knee arthroplasty

Total knee arthroplasty (TKA) is a surgical procedure to treat end stage osteoarthritis of the knee. During surgery the articular surfaces of the femur (thighbone) and tibia (shinbone) are removed and replaced by a prosthesis. Traditionally, radiographic images are used to plan the size and alignment of the prosthesis components relative to specific reference axes of the bones. Figure 1.15 gives an overview of commonly used reference axes of the femur. Alignment in the frontal plane usually aims at obtaining a neutral lower limb mechanical axis, i.e. the angle between the mechanical axis of the femur and the mechanical axis of the tibia is 180°. As shown in the top left part of Figure 1.15, the femoral mechanical axis joins the centre of the hip with the centre of the knee. Similarly, the tibial mechanical axis joins the centre of the knee with the centre of the ankle. The femoral and tibial prosthesis components are positioned perpendicular to the mechanical axes of the femur and tibia, respectively. Regarding the sagittal and horizontal plane alignment there is less agreement. For example, the bottom part of Figure 1.15 shows different axes that are used for determining rotational (horizontal plane) alignment.

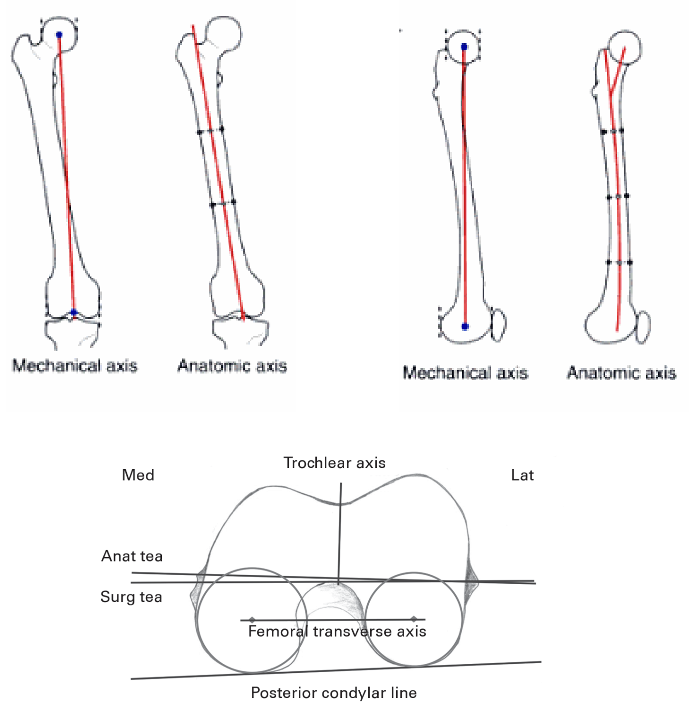

Figure 1.15: Reference axes commonly used in the analysis of the femur: frontal plane (top left) [1], sagittal plane (top right) [1] and horizontal plane (bottom) [54].

Positioning of the femoral component relative to the mechanical axis is not straightforward as the centre of the hip can not be readily identified during surgery. Therefore, the femoral anatomical axis or medial axis of the long diaphysis (see top figures) is commonly used as a reference axis. During surgery, this axis is determined by inserting a metal rod into the medullary canal of the femur. The preoperatively measured angle between the mechanical and anatomical axis is then used to cut the distal femur. In the horizontal plane, the posterior condylar line is often used as a hard reference for positioning the cutting guide. The preoperative measurement of the angle between the posterior condylar line and the desired reference axis (e.g. surgical transepicondylar axis) then allows for determining the proper cutting angle.

It has been demonstrated that correct alignment of the prosthesis components is a crucial factor for the success of TKA [55, 56]. Postoperative malalignment has been associated with instability, stiffness, loosening and patellar dislocation [57–59] and is typically defined as a deviation of 3° or more from the targeted position [60, 61]. Several factors may contribute to errors in alignment, such as observer variability during preoperative planning, difficulties in locating the reference axis during surgery and improper positioning of surgical instruments. In particular, the positioning of intramedullary rods, which allow for determining the anatomical axis, is prone to error. It has been shown that the alignment of the rod is highly dependent on the position of its entry point [62–64]. A thorough planning should therefore be performed, especially in case of large bowing of the distal femur [65].

Computer-assisted planning is more and more performed to allow for visualising the 3D anatomy of the bones and simulating different surgical procedures. The preoperative plan is then transferred to the operation room by fabricating physical guides [66, 67] or using intraoperative navigation [68]. Figure 1.16 shows an example of patient-specific instrumentation for the femur: a surgical guide that fits the patient's anatomy (left) is used to drill the fixation pins of a cutting block (right), which allows to transfer the preoperatively planned bone cuts.

Figure 1.16: Signature™ femoral positioning guide (left) and cutting block (right) for distal resection [69].

A set of 3D landmark and axis definitions, as presented by Victor et al. [70], is summarised in Figure 1.17 and Tables 1.2 and 1.3. Automatic approaches to extract these reference axes could contribute to a faster and more precise 3D planning and evaluation of the procedure.

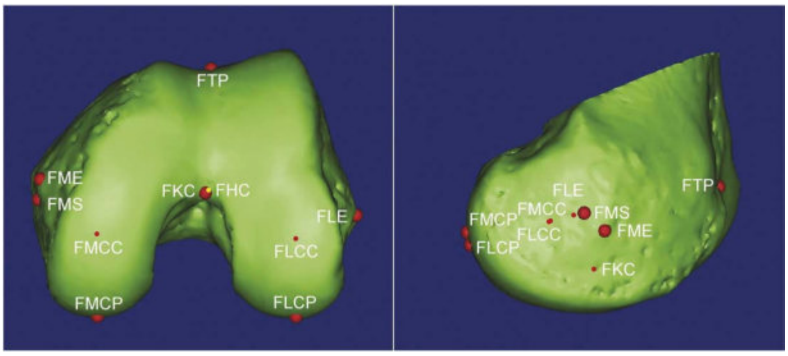

Figure 1.17: Landmarks commonly used in the analysis of the femur: horizontal plane (left) and sagittal plane (right) [70].

Table 1.2: Landmarks commonly used in the analysis of the femur and their 3D definition as proposed by Victor et al. [70].

Landmark	3D definition
Femoral hip centre (FHC)	Centre of best-fit sphere to the head of the femur
Femoral knee centre (FKC)	Most anterior point in the middle of the femoral notch on a caudal to cranial view of the femur, aligning the hip centre with the roof of the femoral notch
Femoral lateral condyle centre (FLCC)	Centre of the best-fit sphere to the lateral condyle
Femoral lateral condyle posterior (FLCP)	The most posterior point of the lateral condyle on the 3D model of the femur, aligned along the mechanical axis
Femoral lateral epicondyle (FLE)	The most anterior and distal osseous prominence over the lateral aspect of the lateral femoral
Femoral medial condyle centre (FMCC)	Centre of the best-fit sphere to the medial condyle
Femoral medial condyle posterior (FMCP)	The most posterior point of the medial condyle on the 3D model of the femur, aligned along the mechanical axis
Femoral medial epicondyle (FME)	Most anterior and distal osseous prominence over the medial aspect of the medial femoral condyle
Femoral medial sulcus (FMS)	Depression on the bony surface slightly proximal and posterior to FME
Femoral trochlea proximal (FTP)	Deepest point of the trochlear groove on the 3D model of the femur, aligned along the mechanical axis

Table 1.3: Axes commonly used in the analysis of the femur and their 3D definition as proposed by Victor et al. [70].

Axis	3D definition
Anatomical transepicondylar axis	FME - FLE
Mechanical axis	FHC - FKC
Posterior condylar line	FMCP - FLCP
Surgical transepicondylar axis	FMS - FLE
Transverse axis	FMCC - FLCC
Trochlear antero-posterior axis (also called Whiteside line)	FKC - FTP

1.7 Remarks on 3D automatic landmark extraction

While many 2D landmark definitions are available in literature, the data on 3D measurements is more limited. Many conventional 2D landmarks can be used by adding definitions for the third dimension, but new landmarks should also be defined to allow for a 3D analysis of the anatomical structures. As only a limited number of approaches for 3D measurement have been described and different definitions for the same landmarks are sometimes found, standardisation of 3D analyses is still an issue. Compared to conventional radiographic analysis, some landmarks might be easier and other more difficult to define and localise. Studies on the accuracy and precision of these 3D landmarks and measurement are thus required. The orientation of the anatomical part during image acquisition is no longer a concern using CT and MRI as a 3D reconstructed image of the anatomy is provided. However, many measurements require the definition of proper anatomical directions. Establishing one or more standardised reference frames during the analysis is thus usually required.

As mentioned above, automatic landmark extraction techniques may allow for improved standardisation by employing unambiguous definitions. However, the landmarks should be chosen carefully as they should be both anatomically relevant and automatically computable. The well-established geometrical definitions used for manual analysis could be translated into mathematical descriptions, but a good correspondence between both definitions should be found to allow for accurate results. Alternatively, slightly modified definitions for existing landmarks could be proposed and mathematical descriptions for new landmarks could be presented.

While each trial to manually identify a landmark on a medical image may result in different coordinates, automatic procedures aim at determining a unique solution. However, it should be noticed that this only applies to landmark localisation on a single medical image. Different results may be obtained if the algorithms are applied on multiple images of the same anatomical part because the geometry is discretised in different ways. As for manual analysis, the image quality should also be sufficient to allow for accurate results. It is thus desirable to investigate the effect of using different images of the same structure and to compare the results for different image qualities. In addition, the results of the automatic analysis should be compared to the mean values of a set of manually obtained measurements to assess the closeness of agreement between the automatic methods and the clinical knowledge.

Throughout the thesis, several of these issues are addressed: landmark definitions are adapted to include the three dimensions, mathematical descriptions and reference frames are proposed and different images of the same anatomical part are analysed.

1.8 Outline

The thesis is organised as follows:

- In chapter 2, the literature on 3D landmark localisation is reviewed. First, some reports on intra- and interobserver variability associated with manual landmark identification on 3D images of the head and lower limbs are summarised. The results of different studies are compared to see if valuable conclusions about the reliability of different landmarks and measurements can be drawn. Second, the literature on (semi-)automatic landmark extraction from 3D images of the head and lower limbs is reviewed and conclusions about the current state-of-the-art are drawn.

- Chapter 3 provides an overview of the algorithms that are used in this thesis to analyse the skull and femur models. Some mesh operations to simplify, smooth and refine the 3D models and several automatic approaches for landmark extraction are discussed. The main mathematical background is given and each method is illustrated using examples on the skull and femur models.

- In chapter 4, two studies about landmark localisation on the skull are presented. First, a method for semi-automatic localisation of landmarks on the virtual skull is proposed. The new approach is evaluated by assesssing the intra- and interobserver variability for measurements performed on one image of each skull. The second study presents the extraction of a larger number of landmarks and evaluates the method by determining the intraobserver variability for measurements performed on multiple images of the same skull.

- In chapter 5, two studies about landmark extraction on the femur are presented. The first study deals with the insertion of intramedullary rods and aims at determining the optimal entry point. In addition, the feasibility of a reduced scanning protocol is investigated by applying the method on both full and reduced models of the femur, the latter being obtained by removing specific regions from the model. In the second study, the alignment of the femur in the three anatomical planes is considered by extracting various reference axes.

- Finally, chapter 6 gives an overview of the main contributions of this thesis to the field of 3D landmarks and offers some suggestions for further research.

References

[1] Paley D. Normal lower limb alignment and joint orientation. In: Paley D, Herzenberg JE. Principles of deformity correction. Springer-Verlag, New York, 2002.

[2] Hurst CA, Eppley BL, Havlik RJ, Sadove AM. Surgical cephalometrics: applications and developments. Plast Reconstr Surg, 120(6):92e-104e, 2007.

[3] Taub PJ. Cephalometry. J Craniofac Surg, 18(4):811-817, 2007.

[4] Delaunay S, Dussault RG, Kaplan PA, Alford BA. Radiographic measurements of dysplastic adult hips. Skeletal Radiol, 26(2):75-81, 1997.

[5] Pogrel MA. What are normal esthetic values? J Oral Maxillofac Surg, 49(9):963-969, 1991.

[6] Yoon YS, Hodgson AJ, Tonetti J, Masri BA, Duncan C. Resolving inconsistencies in defining the target orientation for the acetabular cup angles in total hip arthroplasty. Clin Biomech, 23(3):253-259, 2008.

[7] Grood ES, Suntay WJ. A joint coordinate system for the clinical description of three-dimensional motions: application to the knee. J Biomech Eng, 105(2):136-144, 1983.

[8] Thirion J-P, Gourdon A. Computing the differential characteristics of isointensity surfaces. Comput Vis Image Underst, 61(2):190-202, 1995.

[9] Nizard R. Computer assisted surgery for total knee arthroplasty. Acta Orthop Belg, 68(3):215-230, 2002.

[10] Schöttle PB, Schmeling A, Rosenstiel N, Weiler A. Radiographic landmarks for femoral tunnel placement in medial patellofemoral ligament reconstruction. Am J Sports Med, 35(5):801-804, 2007.

[11] Ziegler CG, Pietrini SD, Westerhaus BD, Anderson CJ, Wijdicks CA, Johansen S, Engebretsen L, LaPrade RF. Arthroscopically pertinent landmarks for tunnel positioning in single-bundle and double-bundle anterior cruciate ligament reconstructions. Am J Sports Med, 39(4):743-752, 2011.

[12] Gomes GT, Van Cauter S, De Beule M, Vigneron L, Pattyn C, Audenaert EA. Patient-specific modelling in orthopedics: from image to surgery. Biomedical imaging and computational modeling in biomechanics, Springer, accepted.

[13] Van Sint Jan S. Color atlas of skeletal landmark definitions. Guidelines for reproducible manual and virtual palpations. Churchill Livingstone-Elsevier, Edinburgh, 2007.

[14] Van Sint Jan S, Della Croce U. Identifying the location of human skeletal landmarks: why standardized definitions are necessary-a proposal. Clin Biomech (Bristol, Avon), 20(6):659-660, 2005.

[15] Tng TT, Chan TC, Cooke MS, Hgg U. Effect of head posture on cephalometric sagittal angular measures. Am J Orthod Dentofacial Orthop, 104(4):337-341, 1993.

[16] Shibanuma N, Sheehan FT, Stanhope SJ. Limb positioning is critical for defining patellofemoral alignment and femoral shape. Clin Orthop Relat Res, 434:198-206, 2005.

[17] Bull AM, Katchburian MV, Shih YF, Amis AA. Standardisation of the description of patellofemoral motion and comparison between different techniques. Knee Surg Sports Traumatol Arthrosc, 10(3):184-193, 2002.

[18] Wu G, Siegler S, Allard P, Kirtley C, Leardini A, Rosenbaum D, Whittle M, D'Lima DD, Cristofolini L, Witte H, Schmid O, Stokes I; Standardization and Terminology Committee of the International Society of Biomechanics. ISB recommendation on definitions of joint coordinate system of various joints for the reporting of human joint motion-part I: ankle, hip, and spine. International Society of Biomechanics. J Biomech, 35(4):543-548, 2002.

[19] Wu G, van der Helm FC, Veeger HE, Makhsous M, Van Roy P, Anglin C, Nagels J, Karduna AR, McQuade K, Wang X, Werner FW, Buchholz B; International Society of Biomechanics. ISB recommendation on definitions of joint coordinate systems of various joints for the reporting of human joint motion–Part II: shoulder, elbow, wrist and hand. J Biomech, 38(5):981-992, 2005.

[20] Mori Y, Miyajima T, Minami K, Sakuda M. An accurate three-dimensional cephalometric system: a solution for the correction of cephalic malpositioning. J Orthod, 28(2):143-149. 2001.

[21] Bergersen EO. Enlargement and distortion in cephalometric radiography: compensation tables for linear measurements. Angle Orthod, 50(3):230-244, 1980.

[22] Grayson B, Cutting C, Bookstein FL, Kim H, McCarthy JG. The three-dimensional cephalogram: theory, technique, and clinical application. Am J Orthod Dentofacial Orthop, 94(4):327-337, 1988.

[23] Van Sint Jan S, Sobzack S, Dugailly PM, Feipel V, Lefèvre P, Lufimpadio JL, Salvia P, Viceconti M, Rooze M. Low-dose computed tomography: a solution for in vivo medical imaging and accurate patient-specific 3D bone modeling? Clin Biomech (Bristol, Avon), 21(9):992-998, 2006.

[24] Olszewski R, Reychler H, Cosnard G, Denis JM, Vynckier S, Zech F. Accuracy of three-dimensional (3D) craniofacial cephalometric landmarks on a low-dose 3D computed tomograph. Dentomaxillofac Radiol, 37(5):261-267, 2008.

[25] Loubele M, Bogaerts R, Van Dijck E, Pauwels R, Vanheusden S, Suetens P, Marchal G, Sanderink G, Jacobs R. Comparison between effective radiation dose of CBCT and MSCT scanners for dentomaxillofacial applications. Eur J Radiol, 71(3):461-468, 2009.

[26] Zbijewski W, De Jean P, Prakash P, Ding Y, Stayman JW, Packard N, Senn R, Yang D, Yorkston J, Machado A, Carrino JA, Siewerdsen JH. Design and optimization of a dedicated cone-beam CT system for musculoskeletal extremities imaging. SPIE Medical Imaging, Physics of Medical Imaging, vol. 7961, pages 796104-796104-8, 2011.

[27] Henckel J, Richards R, Lozhkin K, Harris S, Baena FM, Barrett AR, Cobb JP. Very low-dose computed tomography for planning and outcome measurement in knee replacement. The imperial knee protocol. J Bone Joint Surg Br, 88(11):1513-1518, 2006.

[28] http://thesebonesofmine.wordpress.com

[29] http://www.anatomy.tv/StudyGuides

[30] Marieb EN, Hoehn K. Anatomy & physiology. Pearson Education, Inc., publishing as Pearson Benjamin, 2008.

[31] Zappa M. Analytical measurement terminology in the laboratory. Part 1: Trueness, precision and accuracy. Thermal analysis, 1/ 2009.

[32] The truth about accuracy in the validation of analytical methods. Training Resources from Mourne Training Services, 2009.

[33] Bailey LJ, Proffit WR, White R Jr. Assessment of patients for orthognathic surgery. Semin Orthod, 5(4):209-222, 1999.

[34] Al-Riyami S, Cunningham SJ, Moles DR. Orthognathic treatment and temporomandibular disorders: a systematic review. Part 2. Signs and symptoms and meta-analyses. Am J Orthod Dentofacial Orthop, 136(5):626.e1-16, discussion 626-627, 2009.

[35] Schendel SA, Powell NB. Surgical orthognathic management of sleep apnea. J Craniofac Surg, 18(4):902-911, 2007.

[36] Broadbent BH. A new X-ray technique and its application to orthodontia. Angle Orthod, 1(2):45-66, 1931.

[37] Hofrath H. Die bedeutung der rontgenfern und abstandsaufnahme für die diagnostik der kieferanomalien. J Orofac Orthop, 1(2):232-258, 1931.

[38] Eggensperger N, Smolka K, Luder J, Iizuka T. Short- and long-term skeletal relapse after mandibular advancement surgery. Int J Oral Maxillofac Surg, 35(1):36-42, 2006.

[39] Patel PK, Morris DE, Gassman A. Complications of orthognathic surgery. J Craniofac Surg, 18(4):975-985, 2007.

[40] Proffit WR, Turvey TA, Phillips C. The hierarchy of stability and predictability in orthognathic surgery with rigid fixation: an update and extension. Head Face Med, 3:21, 2007.

[41] Lagravère MO, Low C, Flores-Mir C, Chung R, Carey JP, Heo G, Major PW. Intraexaminer and interexaminer reliabilities of landmark identification on digitized lateral cephalograms and formatted 3-dimensional cone-beam computerized tomography images. Am J Orthod Dentofacial Orthop, 137(5):598-604, 2010.

[42] Chen YJ, Chen SK, Yao JC, Chang HF. The effects of differences in landmark identification on the cephalometric measurements in traditional versus digitized cephalometry. Angle Orthod, 74(2):155-161, 2004.

[43] Kumar V, Ludlow J, Soares Cevidanes LH, Mol A. In vivo comparison of conventional and cone beam CT synthesized cephalograms. Angle Orthod, 78(5):873-879, 2008.

[44] Kaipatur N, Flores-Mir C. Accuracy of computer programs in predicting orthognathic surgery soft tissue response. J Oral Maxillofac Surg, 67(4):751-759, 2009.

[45] Kaipatur N, Al-Thomali Y, Flores-Mir C. Accuracy of computer programs in predicting orthognathic surgery hard tissue response. J Oral Maxillofac Surg, 67(8):1628-1639, 2009.

[46] Shaheed S, Iftikhar A, Rasool G, Bashir U. Accuracy of linear cephalometric measurements with scanned lateral cephalograms. Pak Oral Dent J, 31(1):68-72, 2011.

[47] Swennen GR, Mollemans W, Schutyser F. Three-dimensional treatment planning of orthognathic surgery in the era of virtual imaging. J Oral Maxillofac Surg, 67(10):2080-2092, 2009.

[48] Popat H, Richmond S, Drage NA. New developments in: three-dimensional planning for orthognathic surgery. J Orthod, 37(1):62-71, 2010.

[49] McCormick SU, Drew SJ. Virtual model surgery for efficient planning and surgical performance. J Oral Maxillofac Surg, 69(3):638-644, 2011.

[50] Mazzoni S, Badiali G, Lancellotti L, Babbi L, Bianchi A, Marchetti C. Simulation-guided navigation: a new approach to improve intraoperative three-dimensional reproducibility during orthognathic surgery. J Craniofac Surg, 21(6):1698-1705, 2010.

[51] Swennen GRJ, Schutyser F, Hausamen JE. Three-dimensional cephalometry. A color atlas and manual, Springer, 2006.

[52] Olszewski R, Cosnard G, Macq B, Mahy P, Reychler H. 3D CT-based cephalometric analysis: 3D cephalometric theoretical concept and software. Neuroradiology, 48(11):853-862, 2006.

[53] Bettega G, Payan Y, Mollard B, Boyer A, Raphael B, Lavallee S. A simulator for maxillofacial surgery integrating 3D cephalometry and orthodontia. Comp Aid Surg, 5(3):156-165, 2000.

[54] Victor J, Van Doninck D, Labey L, Van Glabbeek F, Parizel P, Bellemans J. A common reference frame for describing rotation of the distal femur: a ct-based kinematic study using cadavers. J Bone Joint Surg Br, 91(5):683-690, 2009.

[55] Lotke PA, Ecker ML. Influence of positioning of prosthesis in total knee replacement. J Bone Joint Surg Am, 59(1):77-79, 1977.

[56] Ritter MA, Faris PM, Keating EM, Meding JB. Postoperative alignment of total knee replacement. Its effect on survival. Clin Orthop Relat Res, (299):153-156, 1994.

[57] Seil R, Pape D. Causes of failure and etiology of painful primary total knee arthroplasty. Knee Surg Sports Traumatol Arthrosc, 19(9):1418-1432, 2011.

[58] Windsor RE, Scuderi GR, Moran MC, Insall JN. Mechanisms of failure of the femoral and tibial components in total knee arthroplasty. Clin Orthop Relat Res, (248):15-19; discussion 19-20, 1989.

[59] Motsis EK, Paschos N, Pakos EE, Georgoulis AD. Review article: Patellar instability after total knee arthroplasty. J Orthop Surg (Hong Kong), 17(3):351-357, 2009.

[60] Sikorski JM. Alignment in total knee replacement. J Bone Joint Surg Br, 90(9):1121-1127, 2008.

[61] Lombardi AV Jr, Berend KR, Ng VY. Neutral mechanical alignment: a requirement for successful TKA: affirms. Orthopedics, 34(9):e504-506, 2011.

[62] Reed SC, Gollish J. The accuracy of femoral intramedullary guides in total knee arthroplasty. J Arthroplast, 12(6):677-682, 1997.

[63] Harding IJ, Crawford RW, Mclardy-Smith P, Murray DW. The importance of femoral intramedullary entry point in knee arthroplasty. The Knee, 6(3):207-210, 1999.

[64] Mihalko WM, Boyle J, Clark LD, Krackow KA. The variability of intramedullary alignment of the femoral component during total knee arthroplasty. J Arthroplasty, 20(1):25-28, 2005.

[65] Jeffery JA. Accuracy of intramedullary femoral alignment in total knee replacement: intraoperative assessment of alignment rod position. The Knee, 6(3):211-215, 1999.

[66] Ng VY, DeClaire JH, Berend KR, Gulick BC, Lombardi AV Jr. Improved accuracy of alignment with patient-specific positioning guides compared with manual instrumentation in TKA. Clin Orthop Relat Res, 470(1):99-107, 2012.

[67] Nunley RM, Ellison BS, Zhu J, Ruh EL, Howell SM, Barrack RL. Do patient-specific guides improve coronal alignment in total knee arthroplasty? Clin Orthop Relat Res, 470(3):895-902, 2012.

[68] Mason JB, Fehring TK, Estok R, Banel D, Fahrbach K. Meta-analysis of alignment outcomes in computer-assisted total knee arthroplasty surgery. J Arthroplasty, 22(8):1097-1106, 2007.

[69] http://www.biomet.com/orthopedics

[70] Victor J, Van Doninck D, Labey L, Innocenti B, Parizel PM, Bellemans J. How precise can bony landmarks be determined on a CT scan of the knee? Knee, 16(5):358-365, 2009.

2

Literature review on 3D landmark localisation

This chapter provides an overview of the literature on 3D landmark localisation. First, some reports on intra- and interobserver variability associated with manual landmark identification on 3D images of the head and lower limbs are summarised. The results of different studies are compared to see if valuable conclusions about the reliability of different landmarks and measurements can be drawn. Second, the literature on (semi-)automatic landmark extraction from 3D images of the head and lower limbs is reviewed and conclusions about the current state-of-the-art are drawn. Most studies have been published in the last decade, which shows that 3D landmark-based analysis is a relatively new topic both in academic research and clinical practice. The reader is referred to Figure 1.12 and Table 1.1 for an overview of the landmarks that are most commonly used in the analysis of the skull and to Figures 1.17 and 1.15 and Tables 1.2 and 1.3 for an overview of the points and axes that are most commonly used in the analysis of the femur.

2.1 Variability of manual landmark identification

The manual localisation of landmarks, either on the bone or on medical images, is prone to intra- and interobserver variations. Different factors contribute to the landmark localisation variability: the perception of human operators is subjective, the image resolution might be insufficient, the operators might use other landmark definitions, the landmarks are often not merely points but relatively large areas, etc. It is important to measure their reliability to determine which landmarks are clinically acceptable and thus allow for correct analysis of the patient data. This section summarises some of the studies reporting on the reliability of landmark identification on 3D images of the head and lower limbs and aims at drawing some conclusions about the reliability of different landmarks and measurements. Studies reporting on the precision of a relatively large number of landmarks and/or including a large number of datasets were selected. In addition, results on the precision of the individual landmarks were preferred over the precision of linear or angular measurements between the landmarks. Finally, linear or angular deviations were preferred over correlation coefficients as they allow for a better evaluation of clinically significant values. The literature study is split into two parts: first, the landmarks of the skull are analysed and second, the lower limbs are discussed.

2.1.1 Landmarks of the skull

2.1.1.1 Studies

Swennen et al. [1] obtained CT scans with 1.25 mm slice thickness of 20 patients to compute the reliability of 14 landmarks. The points were identified using the corresponding 3D surface models and using virtual lateral and frontal cephalograms that are computed as orthogonal projections from the CT dataset. Two investigators each marked the points two times. Correlation tests were performed for each landmark and each anatomical direction based on the two trials (intraobserver) and on the average observer values (interobserver). Intraobserver squared correlation coefficients were above 0.95 for all anteroposterior (AP), 13 superoinferior (SI) and 8 mediolateral (ML) measurements. Interobserver squared correlation coefficients were above 0.95 for all AP, 12 SI and 7 ML measurements. The landmarks that were least reliable in the SI direction were condylion and zygion. The landmarks that were least reliable in the ML direction were anterior nasal spine, A-point, posterior nasal spine and orbitale.

Ludlow et al. [2] studied the reliability of 14 hard tissue and 10 soft tissue landmarks. They used multiplanar reconstructed images with 0.4 mm slice thickness and 3D surface renderings obtained by cone-beam CT (CBCT) scanning of 20 presurgical orthodontic patients. Five observers each performed four analyses, spread over two weeks. Interobserver pairwise differences were calculated and averaged across all trials and datasets. The mean values of the 3D distances for the bony landmarks ranged between 1.24 mm and 8.07 mm. The most reliable landmarks were nasion and sella ($<$1.5 mm), while the least reliable points were orbitale and porion ($>$6.0 mm). The mean values for the remaining points ranged between 1.5 mm and 3.3 mm. Significant differences in variability between the different anatomical directions were found for some of the landmarks. For example, both orbitale and porion showed large variations in the ML direction (5.76 mm and 7.14 mm). The large deviations for landmark porion, however, were due to differences in the definition that was employed by different observers.

The reliability of landmark identification for two different types of analyses, 3D-Swennen [1] and 3D-ACRO [3], was studied by Olszewski et al. [4]. They used 3D surface renderings, generated from CT images with 1 mm slice thickness, from 13 patients. Two observers made two series of landmark identifications that were 1 week apart. For both types of analyses 22 landmarks were marked and for each landmark two intraobserver and four pairwise interobserver distances were obtained. The mean interobserver variation for the 3D-ACRO analysis (1.8 mm $\pm$ 1.04 mm) was significantly lower than the mean interobserver variation for the 3D-Swennen analysis (2.47 mm $\pm$ 1.04 mm). The least reliable landmarks in the 3D-Swennen analysis were zygion (>8 mm), pogonion (>5 mm), porion, orbitale, infraorbitale, mentale and gonion (>3 mm). The most reliable landmarks were anterior nasal spine, frontozygomatic and basion (<1.5 mm). Some differences in landmark ranking are observed compared to the study of Swennen et al., where for example orbitale was found to be less reliable than pogonion, and low precision was found for anterior nasal spine in the ML direction. However, different sets of landmarks were included in the studies, making it difficult to compare them.

Lagravère et al. [5] used CBCT scans with 0.5 mm slice thickness of 10 patients to determine the reliability of 26 points. Multiplanar and 3D reconstructions were created and landmark coordinates were obtained for each image set by one investigator three times and by two investigators one time. All examiners were trained in using the software and in landmark identification. Intraclass correlation coefficients and measurement errors (mean differences between measurement trials) were obtained for all landmark coordinates. Intraclass correlation coefficients were greater than 0.9. Interobserver errors were higher than 1 mm for 21, 12 and 11 of the landmarks respectively in the ML, AP and SI directions. Landmarks that were least reliable were gonion (>6 mm), anterior nasal spine, condylion, orbitale and porion (>3 mm).

The interobserver variability for a large number of operators was investigated by Schlicher et al. [6]. Nine second- and third-year orthodontic residents identified 32 landmarks in 19 datasets. Multiplanar reconstructions with 0.3 mm slice thickness and 3D renderings, obtained from the CBCT scans, were available for landmark identification. All examiners attended two 1 hour training sessions and were then given six months to locate the points on the 19 patient files. The interobserver consistency was obtained by calculating the distance of each landmark value from the mean value across all observers. Mean variations were obtained by averaging across all observers and datasets. Outliers, greater than 2 times the standard deviation (SD) from the mean landmark location, were assumed to be due to technical errors and were removed from the dataset. They found that midline structures and landmarks formed by acute angles were more consistently identified than bilateral structures and landmarks along broad curves. Among the most consistent points were sella, basion and nasion (<1.1 mm), while orbitale, porion, condylion and gonion were among the least consistent landmarks (>2 mm). The ML error was largely responsible for the low reliability of orbitale and porion.

Titiz et al. [7] measured the reliability of 28 landmarks using spiral CT scans of 20 patients. Axial sectional images were reconstructed at 0.6 mm intervals and 3D reconstructions were created. The datasets were analysed by two orthodontists and two postgraduate students. Each dataset was analysed twice by each observer with an interval of three weeks. Outliers, outside of the range of 4 times the SD, were detected for each subgroup defined by patient, landmark and coordinate axis and excluded from the analysis. The number of outliers per patient ranged from 0 to 2.2 %. The intraobserver SD ranged between 0.14 mm and 2.00 mm (median 0.46 mm) and interobserver SD ranged between 0.02 mm and 2.47 mm (median 0.20 mm). About 85 % of the landmarks were measured with a total SD of less than or equal to 1 mm. The landmarks nasion and infradentale were most reliable, with minor SD for all three coordinates. Point orbitale revealed high interobserver SD, especially in the ML direction (2.54 mm).

The mean 3D intra- and interobserver variations for a number of commonly used skeletal landmarks are summarised in Table 2.1. It should be mentioned that mean 3D values were only reported by Olszewski et al. [4]. Therefore, the other 3D values in the table are computed from the mean variations in the three anatomical directions. The interobserver variations for each direction are given in Table 2.2 for three of the studies.

Table 2.1: Mean 3D intra- and interobserver precision for landmarks commonly used in the analysis of the skull.

	Intra (mm)			Inter (mm)				
Landmark / Study	[4]	[5]	[7]	[2]	[4]	[5]	[6]	[7]
Anterior nasal spine	0.61	1.51	0.71	1.74	0.71	3.36	1.15	0.36
A-point	1.22	0.90	0.99	2.25	1.80	1.44	1.20	0.40
Basion	0.83	1.62	0.66	/	1.14	1.87	0.85	0.40
B-point	2.38	1.58	1.40	2.65	2.97	2.42	1.50	1.50
Condylion left	/	1.07	/	/	/	3.43	2.06	/
Condylion right	/	1.78	/	3.29	/	3.75	2.42	/
Gnathion	/	0.74	0.87	2.51	/	1.85	1.35	0.58
Gonion left	0.80	1.65	1.59	/	2.26	4.97	2.31	1.18
Gonion right	1.45	1.60	/	2.73	3.09	6.70	1.91	/
Menton	1.79	0.92	/	2.31	1.84	2.01	1.58	/
Nasion	0.55	0.66	0.58	1.24	1.13	2.09	1.02	0.18
Orbitale left	0.74	1.41	2.17	/	1.09	2.91	2.43	2.72
Orbitale right	1.71	1.14	/	6.45	3.35	3.69	2.69	/
Pogonion	2.16	0.90	1.06	2.44	5.14	2.02	1.63	0.17
Porion left	2.08	3.69	1.29	/	2.64	3.42	2.33	0.99
Porion right	2.52	2.90	/	8.07	3.21	2.94	2.69	/
Sella	0.75	1.70	0.82	1.40	1.72	1.40	0.50	0.32

Table 2.2: Mean interobserver precision in the mediolateral (ML), anteroposterior (AP) and superoinferior (SI) directions for landmarks commonly used in the analysis of the skull.

	ML (mm)			AP (mm)			SI (mm)		
Landmark / Study	[2]	[5]	[6]	[2]	[5]	[6]	[2]	[5]	[6]
Anterior nasal spine	0.66	1.93	0.47	1.43	2.51	0.76	0.73	1.13	0.36
A-point	0.68	0.92	0.47	0.74	0.80	0.34	2.01	0.77	1.07
Basion	/	1.23	0.33	/	0.97	0.32	/	1.03	0.35
B-point	1.32	1.51	0.65	0.69	0.54	0.55	2.19	1.81	0.87
Condylion left	/	3.08	1.04	/	1.28	1.50	/	0.78	0.52
Condylion right	2.55	3.48	1.25	1.82	1.36	1.07	1.01	0.37	0.46
Gnathion	1.40	1.42	0.67	1.04	0.93	0.78	1.80	0.73	0.72
Gonion left	/	1.57	0.86	/	3.90	0.96	/	2.66	1.78
Gonion right	1.22	1.54	0.71	1.71	5.50	0.77	1.75	3.50	1.37
Menton	1.43	1.51	0.69	1.65	1.21	1.20	0.75	0.55	0.38
Nasion	0.65	0.68	0.48	0.66	0.86	0.33	0.83	1.78	0.62
Orbitale left	/	2.57	2.09	/	1.20	0.59	/	0.64	0.62
Orbitale right	5.76	3.25	2.37	2.80	1.63	0.94	0.80	0.61	0.43
Pogonion	1.35	1.44	0.70	0.69	0.71	0.50	1.91	1.22	1.23
Porion left	/	2.94	2.20	/	1.65	0.62	/	0.59	0.49
Porion right	7.14	2.70	2.37	1.46	0.90	0.94	3.46	0.73	0.43
Sella	1.05	1.21	0.14	0.65	0.41	0.23	0.66	0.57	0.31

2.1.1.2 Discussion

Studies reporting on the reliability of landmarks of the skull generally include a large number of points. This is partially due to the fact that some landmarks can be found on the left as well as on the right part of the skull. Nevertheless, they allow to compare between the different landmarks and anatomical directions. Among the least reliable points are porion, orbitale, zygion, gonion and condylion, while basion, nasion and sella are typically among the most reliable landmarks. Some points, such as gonion and condylion, are located on widely curved surfaces, making it difficult to identify them as one specific point. For other points, it is found that they are easily identified along one or two directions, but more difficult along a third direction. For example, orbitale is most easily distinguished along the SI and AP axes, but can be hard to identify in the ML direction if the inferior orbital margin has a relatively flat shape. Also porion is usually more difficult to localise along the ML axis because of the relatively flat shape of the external acoustic meatus in this direction. In general, the reliability of landmark localisation is least in the ML direction. This might be a result of the traditional use of lateral cephalograms, which allow for measurement in the SI and AP directions.

The reported values of intra- and interobserver variability vary among different studies. This might be due to different factors: the method used to calculate intra- and interobserver variability, the number of trials, the experience of the operators, the image quality, etc. For example, Swennen et al. calculated correlation coefficients, Ludlow et al., Olszewsi et al. and Lagravère et al. used pairwise differences, Schlicher et al. obtained differences from the mean value and Titiz et al. calculated the SD of the landmark positions. The 3D interobserver variations reported by Schlicher et al. and Titiz et al. are in general smaller compared to the other studies, which might be related to their definition of variability and the exclusion of outliers from the analysis.

Based on the studies discussed in this section, it is found that the mean 3D intraobserver error of the points basion, nasion and sella is usually below 1 mm and that their interobserver error is mostly below 1.5 mm (see Table 2.1). While for some of the landmarks mean interobserver values below 1 mm are found in one of the anatomical directions (e.g. AP direction for pogonion, SI direction for orbitale, porion and menton), mean variations above 2 mm occur for several other points along one of the axes (see Table 2.2). From Table 2.1 it is found that 17 out of 42 (40 %) of the mean 3D intraobserver values are above 1.5 mm and that 37 out of 71 (52 %) of the mean 3D interobserver values are greater than 2 mm.

Because of the differences in observer variability between the landmarks, it is desirable to define a coordinate system based on the more reliable landmarks. For example, Swennen et al. [1] proposed to orient the skull relative to the midsagittal plane using paired midfacial anatomical structures (e.g. the orbits, frontal process of the maxilla, frontozygomatic suture) and to position the horizontal plane 6° below the anterior cranial base (sella-nasion). While the points orbitale and porion may suffer from large observer variability in the ML direction, they are usually very reliable in the SI direction, making them appropriate for defining the horizontal plane. Haffner et al. [8] presented a coordinate system with the ML, AP and SI axes respectively parallel to the orbitale-orbitale line, sella-nasion line and nasion-A-point line. Also, Park et al. [9] established the horizontal plane based on orbitale left and both porion right and left, and the midsagittal plane based on nasion and a point in the prechiasmatic groove. The studies discussed in this section show that the proposed reference frames for cephalometric analysis are indeed based on the more reliable landmarks.

2.1.2 Landmarks of the lower limbs

2.1.2.1 Studies

Yoshino et al. [10] measured the posterior condylar line and surgical and anatomical transepicondylar axis on CT scans of 48 patients who were candidates for total knee arthroplasty. Five continuous, 2 mm thick images at the level of the femoral epicondyle were obtained and rotational alignment of the distal femur was measured by three observers using the single slice in which both epicondyles were seen most clearly among the five images. However, the medial sulcus was detected in only 33 knees. The more severe the grade of osteoarthritis, the more difficult it was to detect the medial sulcus. Pairwise interobserver differences were calculated and averaged across all scans. The mean interobserver variability of the angle between the posterior condylar line and surgical transepicondylar axis across 33 scans was below 1.1°, while for the angle between the posterior condylar line and anatomical transepicondylar axis the mean value across 96 scans was below 0.7°.

Hung et al. [11] used both 2D axial CT slices with 0.625 mm thickness and 3D reconstructions to identify the surgical transepicondylar axis. The position of the transepicondylar axis was expressed as the degree of rotation from the posterior condylar line and compared to the measurements on the 10 cadaveric knees. Six observers performed the measurements on 2 separate occasions at least 1 week apart. They obtained an average of 2.4° ± 2.8° external rotation error in the identification of the transepicondylar axis with 2D CT and an average of 2.9° ± 3.1° with 3D CT. The reported SD shows considerable interobserver differences for the angle between the surgical transepicondylar axis and the posterior condylar line.

A study on the accuracy in ankle centre location was performed by Nofrini et al. [12]. They evaluated the localisation accuracy and reliability of four landmarks and three corresponding tibial mechanical axes (based on most prominent points of malleoli, tibialis anterior tendon point and most distal points of malleoli). The manual measurements were performed using two scout views (frontal and lateral) and a set of 70 axial CT slices with 1 mm thickness. Four surgeons identified the landmarks on the images of four cadaveric limbs. In addition, one surgeon repeated the acquisition three times for each limb. Pairwise differences were calculated and averaged across all trials and limbs. The intraobserver reliability of the four landmark points ranged between 2.8 mm and 5.4 mm, while the interobserver reliability ranged between 3.1 mm and 5.4 mm. The reliability of the three tibial mechanical axes was below 0.6°, 1.2 ° and 0.7° for the three methods used.

While the above studies include only a limited number of measurements, Victor et al. [13] evaluated the reliability of a large set of landmarks on the knee. Six cadaver specimens were scanned with a CT slice thickness of 1.25 mm and 3D models of the femur and tibia were reconstructed. Three observers participated in the study: one experienced surgeon, one medical student and one engineer. After a brief teaching session by the surgeon, they all identified 17 landmarks on each dataset. Two observers also performed all analyses three times with a minimum interval of one week. In addition to the landmarks, the variation of the femoral and tibial axes was quantified. A coordinate frame was defined for the femur and tibia based on the mean positions of the selected landmarks to differentiate between precisions along the relevant anatomical axes. Also, the axes relevant for rotational alignment were projected on the horizontal plane. The difference of the observed values from the mean values were calculated and averaged across all trials and datasets. The intraobserver variability ranged between 0.4 mm and 1.4 mm. The joint centres and condyle centres showed to be most reliable (<1 mm), while the femoral epicondyles and sulcus and the posterior points on the tibial condyles were least reliable (>1 mm). Interobserver variability ranged between 0.3 mm and 3.5 mm. The lowest variation was obtained for the joint centres (<1 mm, except for the tibial knee centre), while the highest variation was shown for the posterior points on the tibial condyles, the tibial tubercle and the femoral lateral epicondyle (>2 mm). Both mechanical axes were determined very precisely ($< 0.3°$). The most reliable axes for rotational alignment were the femoral posterior condylar line ($0.56°$) and tibial transverse axis ($1.66°$). The highest variability was found for the femoral trochlear antero-posterior axis ($2.07°$) and tibial posterior condylar line ($3.16°$). Finally, it was demonstrated that the coordinate systems are defined based on reliable landmarks.

In a study about automatic landmark extraction on 3D models of the knee, Subburaj et al. [14] compared their results to manual measurements performed by three experienced surgeons on three knee models. The models were reconstructed from CT scans with 0.67 mm slice thickness. The interobserver SD was calculated and averaged across all datasets and coordinate axes. The mean values ranged between 2.15 mm and 5.98 mm. All landmarks were located on prominent structures. As a result, the lowest variation was obtained for sharp regions (e.g. tibial intercondylar tubercles) and the highest variation was found for indistinct regions (e.g. tibial medial and lateral peak, femoral medial epicondyle and adductor magnus tubercle).

Similarly, Cerveri et al. [15] presented automated methods to analyse 3D models of the proximal femur and obtained manual measurements to evaluate their method. For intraobserver variability one orthopaedic surgeon analysed 20 CT datasets with 1 mm slice thickness, obtained from cadavers, three times. For interobserver variability three surgeons analysed four datasets once. The difference of the observed values from the mean values were calculated and averaged across all trials. Finally, the maximum values across all datasets were considered for each landmark. The intraobserver results showed high reproducibility for the femoral diaphysis axis (0.4°), head centre (1.9 mm) and head radius (0.8 mm) and lower reproducibility for the neck centre (2.4 mm), neck axis (3.2°), offset (3.0 mm) and neck-shaft angle (3.5°). The values for interobserver variability confirmed these results: diaphysis axis (0.5°), head centre (1.8 mm), head radius (0.5 mm), neck centre (3.1 mm), neck axis (3.3°), offset (3.0 mm) and neck-shaft angle (3.7°).

In a second study on the distal femur [16], the same methodology was followed. The mean intraobserver reliability was highest for the diaphysis axis (0.45°) and posterior condylar line (0.31°) and lower for the anatomical transepicondylar axis (1.01°) and Whiteside line (1.17°). Similar observations were made for the interobserver variability: diaphysis axis (0.50°), posterior condylar line (0.68°), anatomical transepicondylar axis (2.11°) and Whiteside line (2.52°).

The surgical transepicondylar axis and Whiteside line were measured in a third study [17]. A higher number of analyses was performed as the three experts each analysed all 20 datasets four times. Again, the difference of the observed values from the mean values was obtained and root mean square errors across all trials were calculated. Finally, the median value of the errors across all datasets was reported. The intraobserver error was below 1 mm for all landmarks, while the interobserver error was less than 2 mm. The interobserver reliability was least for the anterior patellar groove, resulting in higher variations for the Whiteside line (3.5°) compared to the transepicondylar axis (2.0°).

The same methodology, but using mean instead of root mean square, was applied for measurements of the hip joint [18]. Intraobserver values were reported for the acetabular centre (2.41 mm), radius (0.45 mm) and axis (3.38°). The interobserver values were: centre (2.80 mm), radius (1.02 mm) and axis (3.51°).

2.1.2.2 Discussion

Except for the study of Victor et al., few data are available on the reproducibility of landmarks used for CT-based measurement of lower limb alignment. However, some conclusions can be drawn from the different studies. In the horizontal plane of the femur, both Victor et al. and Cerveri et al. found that the posterior condylar axis is most reliable, while the Whiteside line is least reliable. This can be explained from the reliability of the landmarks that define these axes. The posterior points of the femoral condyles have high reproducibility in the AP direction, leading to low variations in the posterior condylar line. In contrast, the deepest points of the trochlea and femoral notch are more prone to observer variability in the ML direction, leading to higher variations in the Whiteside line. In addition, the Whiteside line is short and consequently, reliability is highly dependent on the precision of its endpoints. As this axis exceeds the clinically acceptable limit of 3°, it is not a reliable landmark for determining rotational alignment. Large differences between the studies are found for the reliability of the surgical and anatomical transepicondylar axis. Interobserver variability below $< 1.1°$ was found by Yoshino et al., but measurements were made on a single slice and the medial sulcus was not identified in all images. In contrast, Hung et al. found larger deviations between different observers (3.1°). While Cerveri et al. reported mean interobserver variabilities around 2°, Victor et al. found values around 1°. However, their measurements were made after a short teaching session and with anatomical drawings at hand. The mechanical axes of femur and tibia were found to be very reliable, which might be due to the large distance between the joint centres. Cerveri et al. also found the long diaphysis axis to be highly reliable, while the neck axis and acetabular axis had lower reproducibility. The interobserver variations reported by Subburaj et al. were relatively high for all landmarks (>2 mm), but the effect on the clinical parameters was not obtained.

2.2 Approaches to automatic landmark extraction

Because of the disadvantages associated with manual landmark localisation, several (semi-)automatic approaches have been presented in literature. This section summarises some of the studies on (semi-)automatic landmark extraction from 3D images of the head and lower limbs and aims at drawing some conclusions about the current state-of-the-art. As mentioned in chapter 1, there is a fundamental difference between 3D multiplanar reconstructions and 3D models: 3D multiplanar images are defined by an intensity function over the 3D voxel positions, while 3D models are usually defined by a mesh topology (i.e. a set of nodes and elements, usually triangles). Therefore, the literature study is split into two parts according to the type of images that is used.

2.2.1 Approaches for 3D multiplanar reconstructions

Many digital image processing techniques have been developed since the 1960s. The types of operations that can be applied to digital images to transform an input image into an output image can be classified into three categories: point, local and global operators if the output value at a specific coordinate is dependent on respectively the input value at that same coordinate, the values in the neighbourhood of that coordinate or the values in the whole image [19]. A popular point operator is contrast stretching by histogram normalisation: the histogram is stretched and shifted so that the intensities lie between the specified upper and lower limits. A typical example of local operators are convolution-based methods, which compute a new value for each pixel in the following way: a window or kernel mask of finite size is overlaid on the image, with the central pixel of the mask matching the pixel to be convolved, and the products of the input values and mask values are summed. The output value is thus calculated as a weighted sum of the input pixels within the convolution kernel. For example, smoothing or noise reduction can be performed using various convolution filters, such as uniform filters (3x3 kernel with equal weights) or Gaussian filters (weights defined by a Gaussian function). The discrete Fourier transform, which converts an image from its spatial domain representation to its frequency domain representation, is a global operator. Its kernel spans the whole image and changes from pixel to pixel.

Different methods for low-level and high-level feature extraction from 2D images have been proposed [20]. Low-level feature extraction methods require only local processing. Typical examples are edge detection and corner detection using first-order and second-order differentiation kernels. High-level feature extraction aims at finding shapes in the image, using for example (rigid and deformable) template matching and active contours.

2.2.1.1 Studies

The 3D analogue of 2D corners are prominent points, such as peak (or tip) and saddle points. Intuitively, corners are understood as points of high curvature on the region boundaries [21]. As for the 2D case, these point landmarks can be detected from the intensity variations in a certain neighbourhood around the point. Various 3D differential operators have been proposed for landmark extraction. Monga et al. [22] and Thirion et al. [23] described the extraction of characteristic lines using differential operators. Two extremality functions are derived from the differential characteristics of the intensity function of the image. These functions are defined as the derivatives of the principal curvatures along the associated principal directions. Its zero-crossings are a set of extremal lines, where the principal curvature is locally extremal in the corresponding principal direction. In [24], the extremal lines are extracted from the 3D image as the intersection of two isosurfaces: one of constant intensity value (e.g. representing the bones) and one of zero extremality. Figure 2.1 shows an example of extremal line extraction on 3D images of the skull. Analogously, extremal points are found where both extremality functions are zero. While some of the extremal lines and points may be recognized as anatomical landmarks, they have been mainly applied for fully automatic image registration. Moreover, the extremality functions use partial derivatives up to the third order, which in general are very sensitive to noise [26]. Differential operators based on the mean and Gaussian curvatures of isocontours [27] and 3D generalizations of 2D corner detectors [26] using partial derivatives up to the second order have also been described to detect points with high intensity variations.

Figure 2.1: Landmark extraction based on differential operators: extremal lines superimposed on the isosurface of the skull [25].

The 3D point landmarks are often determined using a semi-automatic procedure. First, an approximate position of a specific landmark is manually determined. Then, a 3D operator is applied within a region-of-interest (ROI) around the approximate position to extract potential landmark candidates. Finally, the user selects the most promising candidate [28]. A general problem is, however, that often a rather large number of false detections are obtained, due to image noise and the presence of neighbouring anatomical structures in the ROI [29]. Moreover, the differential methods yield voxel positions. Frantz et al. [29] proposed a multi-step approach that combines the 3D point detection with automatic ROI size selection and incorporation of a priori knowledge of the intensity structure at a landmark (e.g. a peak or saddle) to reduce the number of false detections. In addition, they described a method for subvoxel localisation of the 3D point landmarks [30]. Figure 2.2 shows the extraction of the tips of the horns of the ventricular system of the brain. The performance of the multi-step semi-automatic approach was compared with that of a purely manual procedure: five observers each identified up to 76 landmarks on five MRI/CT image pairs. They reported a mean reduction of 38 % of the time spent for landmark extraction (11'30 versus 18'28 minutes) and a mean RMS distance from the mean landmark position of 1.06 mm versus 2.22 mm.

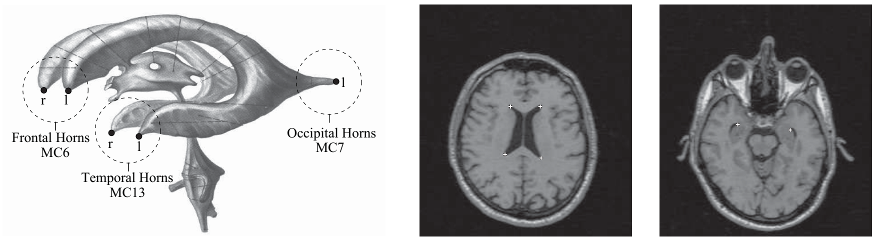

Figure 2.2: Landmark extraction based on differential operators: ventricular system of the brain (left) and axial slices of MRI image with the tips of the frontal and occipital horns (middle) and of the temporal horns (right) marked by white crosses [30].

Despite their relatively low computational costs, differential operators use local image information and are therefore generally sensitive to noise, which leads to false detections and also affects the localisation accuracy [31]. Semi-global approaches based on parametric deformable models have therefore been proposed by Frantz et al. [32, 33]. These models approximate tip- and saddle-like anatomical structures as quadric surfaces (ellipsoids and hyperboloids), which are combined with additional global deformations (like bending or tapering) to enlarge the range of shapes (see Figure 2.3). An initial landmark position is first estimated using the differential approach and the initial model parameters are semi-automatically estimated. The model is then fit to the image data by optimising an edge-based fitting measure that incorporates the strength as well as the direction of the intensity variations. The better the similarity between the directions of the intensity gradients and the normals of the surface model and the stronger the intensity variations along the model surface, the smaller is the fitting measure. Finally, the landmark position can be found as the prominent point of the model, which can be directly computed from the model parameters. The localisation accuracy of the model-fitting approach was compared with that of a differential approach alone for 6 landmarks identified on one MRI/CT image pair of the head. Mean distances to the ground truth positions (manually determined with up to four persons) of 1.22 mm versus 2.11 mm were reported.

Because the deformable surface model approach requires the detection of 3D image edges and uses a relatively complicated fitting measure based on the image gradient as well as the first-order partial derivatives of the surface model, the concept of parametric intensity models was introduced by Worz and Rohr [31]. This

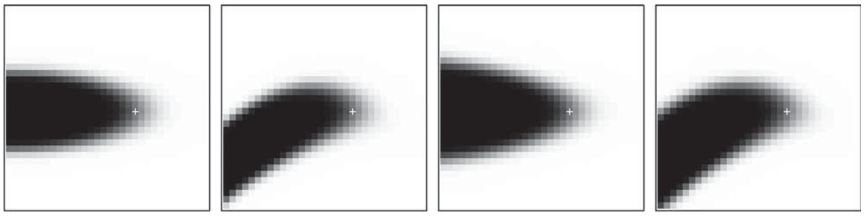

Figure 2.3: Landmark extraction based on parametric intensity models: ellipsoid model (representing tip-like landmarks) without deformations, with bending, with tapering and with both bending and tapering [31].

method uses a fitting measure that directly exploits the intensity information. This work was applied on the ventricular system, zygomatic and occipital bones and orbits using 2 MRI and 1 CT image dataset. A fully automated ROI size selection and parameter initialization was presented, but resulted in unsuccessful model fitting for some of the landmarks, especially in the case of small structures and poor image quality due to image noise. The localisation accuracy of the semi-automatic model-fitting approach was again compared with that of a differential approach alone. While the mean distance to the ground truth position (manually determined with up to four persons) was 1.14 mm versus 2.18 mm for 19 tip-like landmarks, a comparable localisation accuracy was found for 6 saddle-like landmarks. Also, better results were found in comparison to the surface model approach for four tip-like landmarks: 0.68 mm versus 1.26 mm.

Both deformable surface and intensity models allow to extract tip- and saddle-like points. However, the localisation of anatomical landmarks is defined on a historical basis and often does not coincide with points of maximum curvature [34]. This problem might be overcome by using a global approach, such as deformable template matching, a technique which was applied by Ehrhardt et al. [34] to extract landmarks of the pelvis from patient data. They built two 3D atlases of the pelvis (one for each gender), holding labeled CT data sets, 3D models of the separate bone structures and their associated anatomical point landmarks. After automatic segmentation of the bony voxels of the patient data, a gray value-based registration process is performed to align the bone structures of the atlas to the patient data. The bone structures of the patient data set are then separated by means of a nearest-neighbour approach, i.e. the label of the nearest structure in the transformed atlas data set is assigned to each segmented voxel, resulting in an initial set of landmark points. To account for high intersubject anatomical variability, the final landmark position is iteratively computed by performing a non-linear registration of the surface areas in the local neighbourhoud of the atlas landmark and previous patient's landmark. Finally, a patient-related coordinate system is determined and orthopaedic parameters are calculated. The method was applied on seven datasets and by comparison with manual segmentation it was found that for six cases 98.5 % of the bony voxels were correctly labeled. However, an interactive correction was needed for the hip joint and took between 20 and 60 minutes per data set. The detected landmark positions were evaluated visually and found to be correct, except for landmarks near pathological deformations. For one model, a set of 26 manually identified points was obtained five times by two persons, but because of the high deviations of these points (mean value of 2.5 mm), a quantitative comparison of manually and automatically detected landmarks was omitted.

Seim et al. described a procedure for fully automatic segmentation of the pelvis based on a statistical shape model [35] and corresponding landmark extraction [36]. A statistical shape model, representing the mean shape and modes of shape variation is generated from 50 CT scans with a slice thickness of 5 mm. Next, a three-step process is proposed to automatically segment new CT datasets: an affine transformation between the average shape and CT data based on the Generalized Hough Transform, a statistical shape model adaptation, and a free-form deformation based on optimal graph searching. Three different methods were then presented to extract the anterior pelvic plane, which is defined by the left and right anterior superior iliac spines and the pubic symphysis. In the first method, the convex hull of the pelvis is computed and the triangle, whose vertices have the smallest sum of distances from the pubis and the left and right ilium, is determined. The three landmarks are then found from the closest points of the pubis and ilium to the extracted triangle. In the second method, the manually determined landmarks of each training shape are included in the statistical shape model. The adaption of this model yields landmark positions, which are then expressed as a weighted sum of the mesh vertices. These weights are used to calculate the final landmark coordinates from the free-form deformed mesh. In the third method, the manually determined landmarks of a small set of training shapes are used to generate averaged weights, which are applied on the final mesh.

The extracted landmark coordinates and anterior pelvic plane were compared to the positions that were manually identified by one expert. Furthermore, the positions determined by two other experts were used to obtain the interobserver variability. Finally, an additional set of measurements was obtained from 50 higher resolution images (slice thickness of 1 mm). High mean landmark position errors were found for all methods in the low resolution datasets: 2.5 - 6.8 mm for the manual method and 3.6 - 7.8 mm for the automatic methods. The deviation of the anterior pelvic plane was lowest for the convex hull method (1.0°), followed by the manual identification and averaged weights (1.3°) and the statistical shape model weights (1.6°). The landmark position errors improved for the high resolution datasets: 2.3 - 3.9 mm for the manual and convex hull method and 3.5 - 6.8 mm for the other methods. However, the anterior pelvic plane angle only improved for the manual identification (0.7°). The authors state that the lower values for the averaged and statistical shape model weights methods may be attributed to the training landmarks which stem from low resolution data.

2.2.1.2 Discussion

Direct processing of the 3D images requires both selection of the anatomy and landmark extraction to be performed at the same time. As shown by the above studies, fully automatic approaches to handle this complex task are hard to develop. Most of the proposed methods require to manually estimate the landmark position or the deformable model parameters, select the landmark from a set of candidates or perform some manual segmentation. While the extremal line and point algorithm of Thirion et al. is fully automatic, it is mainly used for image registration as only part of the extracted features corresponds to anatomical landmarks. The automatic methods presented by Seim et al. were only evaluated for a small number of landmarks. Also, the number of processed image datasets was relatively low in most of the studies. Nevertheless, automatic approaches can reduce the time spent for manual intervention and improve the landmark localisation precision. Compared to local differential operators, the semi-global deformable models are more robust to image noise by including more a priori knowledge about the landmarks, resulting in better values for the reproducibility. As the above studies mainly focused on the ventricular system, hip and pelvis, automatic landmark extraction from 3D multiplanar images of the skull and femur can be considered a nearly undiscussed topic in literature.

2.2.2 Approaches for 3D models

Unlike for 3D multiplanar images, only geometrical information needs to be processed for automatic landmark localisation on the 3D model. However, this requires that the bony anatomy is already available from the medical images. Although CT imaging allows to obtain high contrast images of the bone structures, which can be mainly segmented using thresholding and region growing algorithms, some manual intervention might be required. (Semi)-automatic approaches for segmentation might also be used, but these methods are beyond the scope of this thesis. Several studies have demonstrated the feasibility of fully automatic landmark extraction from 3D models. As for the 3D multiplanar images, local as well as semi-global and global methods have been described.

2.2.2.1 Studies

A local approach that has been used by different authors is to compute 3D curvature characteristics and then use shape descriptors to select points of local minimum/maximum curvature. For example, Liu et al. [37] applied curvature analysis on optical surface scans of the foot and leg. From the discrete surface data points a regular coordinate grid is generated by least-squares fitting of small second-order polynomial surface patches. A Koenderink shape index colormap is then created from the polynomials to distinguish between convex-shaped, concave-shaped and saddle-shaped structures. The method was tested by scanning a leg 10 times and manually localising five landmarks based on the curvature maps: lateral and medial malleolus, fibular head, point anterior to lateral tibial condyle and medial tibial condyle. Consistent measures of tibial torsion were obtained from the landmarks, with a standard deviation of 0.75°.

A fully automatic approach was presented by Subburaj et al. [14] to determine 14 landmarks on the knee (see Figure 2.4). They segment the mesh surfaces of the femur and tibia into different landmark regions based on surface curvature and label them based on the spatial adjacency relationship between the landmarks. First, the vertices and triangles are grouped based on their mean and Gaussian curvatures values, leading to six different groups. Each group corresponds to a certain geometrical shape, such as a peak or a pit. Probable landmark regions are then formed by searching for edge-connected triangles within a group. Figure 2.5 shows an example of the extracted landmark regions on a femur and tibia model. Next, unwanted regions are detected, e.g. based on area and location, and removed. Finally, the spatial relationships between the landmarks, expressed in terms of the anatomical directions, are used to label the remaining regions by means of a recursive process. The location of each landmark is then given by the mean location of the points in the region. The method was evaluated based on 3 knee models by comparing the extracted landmark locations to the mean values of manual measurements performed by three experienced surgeons. The deviation, averaged over the models and coordinate axes, ranged between 1.92 mm and 4.88 mm for the 14 landmarks. It was found that the automatic identification consistently performed equal or better than the manual method, which resulted in mean interobserver variabilities between 2.15 mm and 5.98 mm. The same approach was also applied on a pelvis model [38].

A commonly used semi-global approach for landmark extraction is analytical curve and surface fitting. Several anatomical structures can be approximated by 2D or 3D quadratic shapes, such as circles and spheres. For example, Li et al. [39] com-

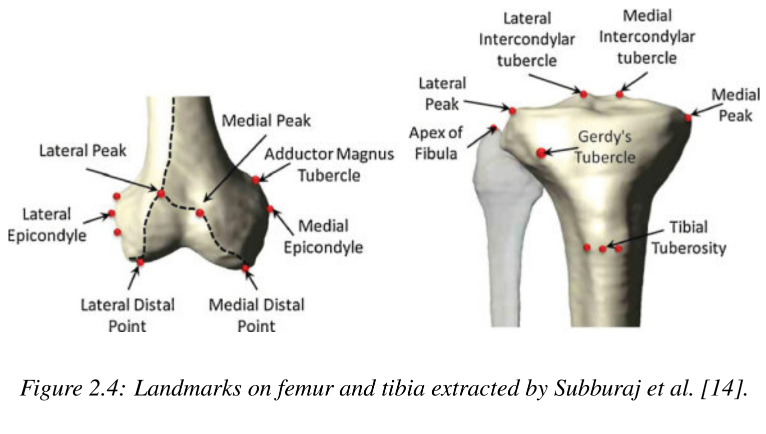

Figure 2.4: Landmarks on femur and tibia extracted by Subburaj et al. [14].

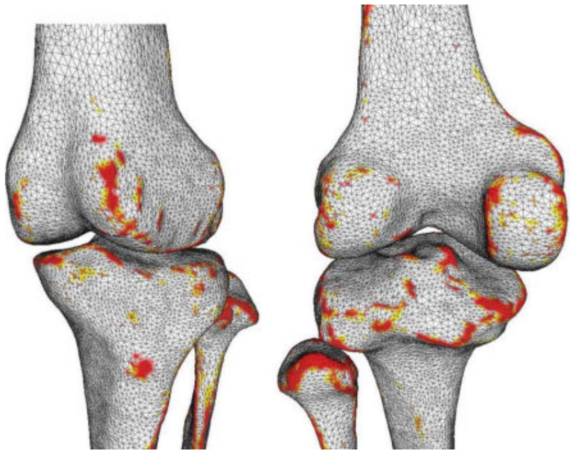

Figure 2.5: Landmark extraction based on curvature analysis: extracted landmark regions [14].

bined curvature characteristics with ellipse fitting to automatically analyse the distal femur articular geometry. They compute the curvature of 2D sagittal profiles to separate the articulating and nonarticulating portions of the condyles. The anterior and posterior extremities of the articulating surface in each cross section are identified from the local curvature maxima and by considering specific regions for each point. This is illustrated in Figure 2.6, where points A and B indicate the posterior and anterior endpoints. A unified sagittal plane is then established by minimizing the eccentricity of all best-fit ellipses to the articular portions, where eccentricity is measured as the dispersion of the focus locations. The proposed framework was tested on 12 knee models. Also, the importance of using a standardised protocol was demonstrated by comparing the radii of best-fit circles to the flexion facet for different lower end locations of the facet and different sagittal plane orientations.

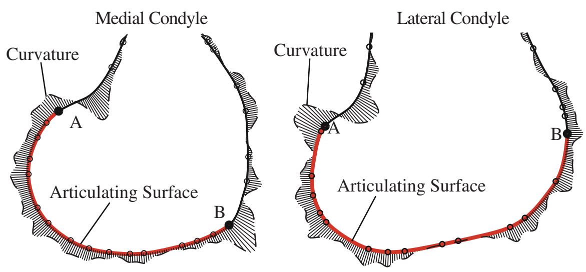

Figure 2.6: Curvature analysis of femoral condyle profiles: the anterior (B) and posterior (A) extremities of the articulating surface are identified from the local curvature maxima and by considering specific regions for each point [39].

Mahaisavariya et al. [40] used conic sections and quadric surfaces to study the geometry of the proximal femur. A best-fit sphere function is applied to the femoral head to derive the femoral head centre and diameter. The neck isthmus centre is found iteratively from the smallest circular cross-section to an iterative neck axis, which is estimated from the centres of best-fit ellipses to the femoral neck. The final femoral neck axis is then defined as the line between the femoral head centre and the neck isthmus centre. Finally, the shaft isthmus and proximal and distal shaft axes are computed from a series of best-fit circles to the medullary canal and shaft. The methods were applied to extract 10 morphological parameters from 108 Thai cadaveric femora. The average values were compared to those reported for Caucasians, but precision or accuracy was not assessed.

Similar methods were applied by Jun and Choi [41] to extract geometrical parameters of the proximal femur to design a patient-specific hip implant. The femoral shaft axis is determined from the centres of best-fit circles to the medullary canal and the shaft isthmus is defined as the location of the smallest circle (see Figure 2.7). A similar approach is used to determine the femoral neck axis and neck isthmus. The femoral head is analysed with slicing planes having a 45° orientation in the AP view. The head radius is found as the maximum radius of a series of best-fit circles and the head centre is the centre of the maximum circle. While the above landmarks are extracted semi-automatically, some other parameters must be determined with the surgeon's intervention to obtain a full set of measurements for implant design. The system also allows the surgeons to modify the value of the extracted parameters based upon their experience. The feasibility of the method was tested using 10 models. They also measured the distance from the implant model to the inner bone surface to study the fit between the models, but the results were not reported.

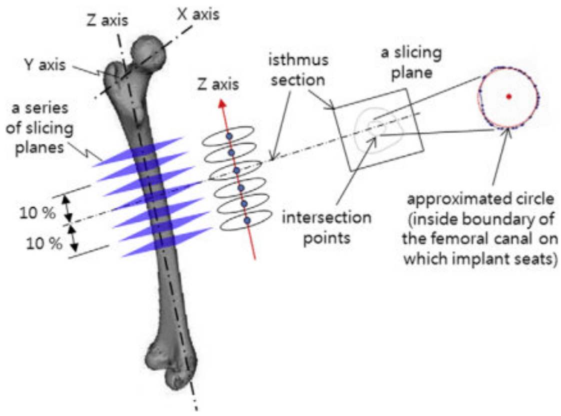

Figure 2.7: Landmark extraction based on geometrical entity fitting: femoral shaft axis determined from the centres of best-fit circles to the medullary canal [41].

Kim et al. [42] measured femoral neck anteversion using a combination of different techniques. The head centre and radius are estimated by fitting circles to the femoral head. Then, the slicing plane that minimises the cross-sectional area of the neck is determined and the neck axis is defined as the line between the centre of the head and the centre of the neck. The long axis of the femur is found by fitting a line to the centres of a series of cross-sections of the femoral shaft. Finally, the condylar line is determined by iteratively computing the most posterior points on the medial and lateral condyles. Neck anteversion is measured as the angle between the neck axis and condylar line projected onto a plane perpendicular to the long axis. The angle was measured on 20 models and compared to measurements on the dried femurs to determine the accuracy of the method. It was shown that the method greatly improves accuracy compared to the manual measurement on 2D CT slices as the absolute difference from the dried femur angle was $1.10° \pm 1.19°$ for the automatic 3D method compared to $5.33° \pm 1.93°$ for the manual 2D CT method.

Miranda et al. [43] combined quadric surfaces with inertial properties to establish anatomical coordinate systems defined solely on the knee geometry, i.e. that do not use the proximal femur and distal tibia. The femoral coordinate system is obtained by fitting a cylinder to the condyles (ML axis) and computing the smallest inertial axis of the diaphysis (axis lying in the frontal plane). Its centre is located at the centroid of the cylinder. The tibial coordinate system is found by isolating the tibial plateau and calculating its centre of mass and inertial axes. To evaluate the repeatability of the algorithm the distal femur and proximal tibia models of 10 cadavers were scaled and aligned to a template bone and the differences in location and orientation of each coordinate system compared to the mean coordinate system were computed. The mean values were below 1.5 mm and 2.5° and the variability between the coordinate systems was thought to arise primarily from differences in bone morphology between specimens.

Subburaj et al. [44] applied their curvature approach along with sphere fitting and medial axis computation to measure lower limb deformities. The medial axes of the bones are extracted using a distance-controlled thinning process, which iteratively removes the outer-most surface of the object, while preserving the topology, until a thin medial structure is left. The following axes were calculated on the femur: mechanical axis, anatomical axis, distal condylar axis, transepicondylar axis and neck axis. The algorithms were tested on three femur and tibia models and angular measurements in the three anatomical planes were derived. The obtained parameters were verified by manual measurement by an experienced surgeon, but no values on the deviations were reported.

A combination of techniques was presented by Cerveri et al. to determine morphological parameters of the femur and pelvis. In a first study [15] they analysed the proximal femur. The femoral diaphysis is approximated by a best-fit cylinder that is initialised from the first principal component direction. Then, the proximal and distal parts are isolated based on the equivalent radius of subsequent cross-sections along the shaft. The femoral head is approximated by a best-fit sphere and the neck centre and axis are defined from the slicing plane that minimises the cross-sectional area of the neck. The reliability of the method was assessed by comparing the measurement values with those obtained by manual expert analysis. Median errors below 1.0 mm, 1.5 mm, 2.0°, 1.0°, 2.1°, 0.2 mm and 1.5 mm were reported for the femoral head centre, neck centre, neck-shaft angle, diaphysis axis, neck axis, head radius and offset.

Their second paper [16] describes the extraction of axes of the distal femur. The anatomical sagittal direction is obtained by iteratively fitting an ellipse to a 2D profile of each condyle and minimizing the difference between the two focal parameters. The anatomical flexion axis is then assumed to be parallel to the sagittal direction and passing through the lateral epicondyle, which is calculated as the surface point at maximum lateral distance. The medial epicondyle is calculated from the 2 mm most medial lying surface of the protuberance. The posterior condylar line is found by connecting the two most posterior points on the medial and lateral condyles. Finally, the Whiteside line or trochlear axis is computed by slicing the intercondylar fossa with a set of planes parallel to the frontal plane, approximating the contours with fourth-order polynomials and fitting a line to the points of maximum curvature of the polynomials. The median values for the reliability test were below 1.0°, 1.6°, 2.0° and 2.4° for the diaphysis axis, posterior condylar line, Whiteside line and anatomical transepicondylar axis.

A third study [17] was presented about the extraction of the Whiteside line by fitting fifth-order polynomials to the cross-sections of the intercondylar fossa. The method is illustrated in Figure 2.8. This paper reported an error of 4.0° ± 2.64° between the automatic and manual measurements. This result might be due to the high median interobserver error of 3.5° that was found in this study.

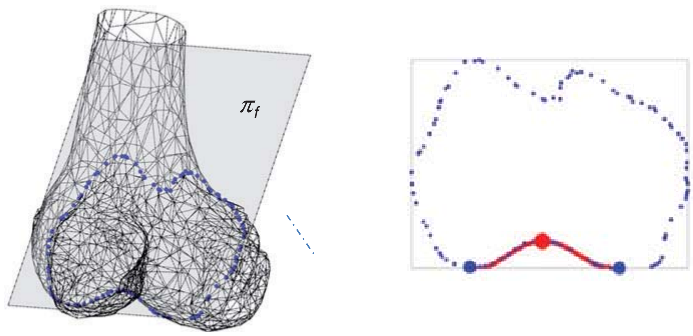

Figure 2.8: Landmark extraction based on polynomial fitting: processing of the femoral intercondylar notch [17].

In their fourth paper [18], they used curvature analysis and sphere and circle fitting to study the acetabular morphology. Based on the Koenderink shape index two groups of clustered regions are generated, corresponding to pit and ridge shapes. A combination of requisites is then used to filter out unwanted regions and generate two single clusters from the pits and ridges, representing respectively the internal acetabular surface and acetabular rim surface. The morphological parameters are then found as follows. The acetabular centre and radius are determined from the best-fit sphere to the union of both surfaces. The acetabular axis is calculated as the normal vector of the best-fit circle to the acetabular rim, passing through the acetabular centre. The notch point and roof thickness are obtained by intersecting the acetabular axis with the pelvic bone surface. The median values for reliability were below 2.7°, 1.5 mm and 0.3 mm for the acetabular axis, centre and radius.

While in most studies local and semi-global methods are applied for landmark extraction, some global approaches have been presented as well. Gargouri and De Guise [45] represented the femur as an algebraic surface using implicit modeling. The implicit function blends together basic geometries such as quadrics (e.g. spheres, cylinders) and superquadrics. The function parameters (positions, orientations, sizes) are found through optimisation. In a next step, landmarks are extracted from the function parameters and the normal vectors on the surface. However, no details are given about the landmark extraction process. The implicit modeling technique was tested on 9 femurs, which were each reconstructed three times, and by visual inspection it was found that the method converges to the same landmarks for all three reconstructed models. Figure 2.9 (left) shows the representation for the proximal femur, which is modelled with an elliptic cylinder and four spheres. It could be critized that the basic geometries might not closely represent the anatomy of the whole bone. However, as demonstrated in Figure 2.9 (right) the method is able to detect the different anatomic regions and the boundaries between them.

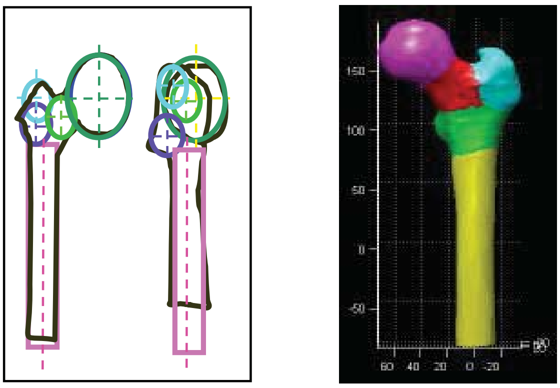

Figure 2.9: Landmark extraction based on implicit modeling: representation of the proximal femur (left) and detection of different regions (right) [45].

Sholukha et al. [46] proposed a regression method to approximate the position of joint coordinate systems and the shape morphology of the femur from three palpable anatomical landmarks: lateral epicondyle, medial epicondyle and greater trochanter. A database of 75 virtual femurs was processed, resulting in three anatomical landmarks and 36 morphological characteristics for each bone. Multiple regression was then performed to determine the relationship between each of the measurements and the three landmarks, i.e. the regression coefficients. This method has the advantage that it can be used in an in-vivo setting: after identifying the location of the three anatomical landmarks on the patient, the morphological characteristics can be estimated using the regression coefficients. The method was validated by manual and virtual palpation of the three landmarks on a (virtual femur of a) healthy volunteer. The morphological measurements predicted from the regression method were compared with the same data obtained directly on the virtual femur. Mean distance and orientation errors of 2.7 mm $\pm$ 2.5 mm and 6.8° $\pm$ 2.7 ° for virtual palpation and 4.5 mm $\pm$ 5.2 mm and 7.5° $\pm$ 5.3° for manual palpation were reported. These results show that the method accuracy depends on the palpation accuracy: the soft tissue interposition on the individual leads to higher errors compared to the landmarks identified on the 3D bone model. It is mentioned by the authors that some of the large errors might be due to large inter-subject variations in the database and it has been proposed to address this problem by including sub-groups characterised by particular bone morphologies.

Figure 2.10 shows how the database models were processed to generate the 36 morphological measurements. Three point landmarks are identified: lateral epicondyle, medial epicondyle and greater trochanter (LE, ME, TC). Also, landmark clouds are selected by virtual palpation on each femoral joint surface: head, lateral and medial condyles at tibiofemoral joint, lateral and medial aspects of patellofemoral joint and patellofemoral sulcus (H, LT, MT, PL, PM, S). These joint surfaces are then approximated by primitive shapes, such as planes and spheres. In addition, each database bone is semi-automatically split into 9 areas-of-interest by transformation of a manually divided template bone and by making manual corrections if required (1-9). Quadric surfaces are then fit to each of the 9 regions: the femoral head is processed as a sphere, the two condyles as ellipsoids and the femoral neck and five diaphysis segments as hyperboloid sheets.

2.2.2.2 Discussion

The above studies show that different approaches for landmark extraction from the virtual lower limbs have been applied. While for some methods, a ROI is first selected, which is then processed to find the specific landmark, other methods allow to segment the whole model into different landmark regions. Curvature analysis has been applied for both semi-automatic as well as fully automatic landmark localisation. The main problem with this method is that the curvature values and thus the landmark position can be strongly influenced by the bone morphology. Analytical curve and surface fitting seems to be the most commonly used method for analysing the lower limb bones. However, different approaches have been used to study the same anatomical part. For example, the femoral diaphysis has been approximated with best-fit circles as well as cylinders and hyperboloids. This shows that there is currently still a lack of standardisation in the 3D analysis. The regres-

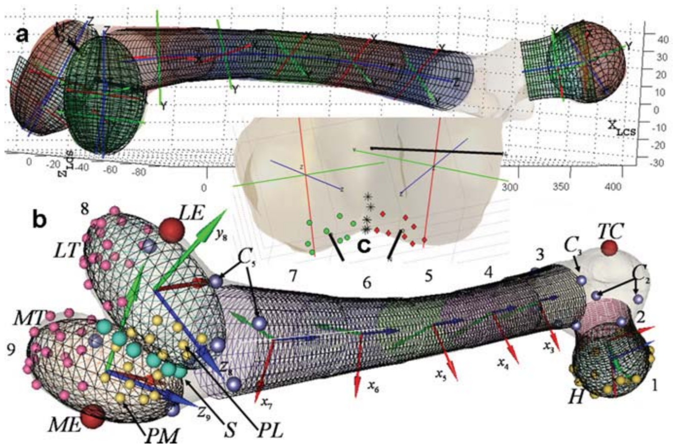

Figure 2.10: Landmark extraction based on multiple regression: processing of database models by point landmark selection (LE, ME, TC), plane and sphere fitting to landmark clouds on the joint surfaces (H, LT, MT, PL, PM, S) and quadric surface fitting to 9 areas-of-interest (1-9) [46].

sion method proposed by Sholukha et al. has the advantage that it can be used in an in-vivo setting, such as for gait analysis, but the precision is currently insufficient for surgical procedures. Nevertheless, they were able to extract a large amount of morphological parameters from the virtual femurs.

While most authors apply one or two techniques for landmark extraction, the combination of multiple techniques might be desirable because of the many different types of landmark definitions found in literature. This was demonstrated by Subburaj et al. and Cerveri et al., who were able to extract a large amount of geometrical parameters. Also, they tested the reliability of their algorithms by comparing the results to the mean values of a set of manually determined measurements. The deviations obtained by Subburaj et al. using the curvature method ranged between 1.92 mm and 4.88 mm. These values are relatively high and the effect on the clinical parameters was not obtained. Moreover, the algorithms were only tested on three knee models. Cerveri et al. showed that most of their parameters were relatively close to the manual measurements ($<$2 mm and 2°). The least reliable axes were the Whiteside line, anatomical transepicondylar axis and acetabular axis, which shows that some of the axes are more prone to variability in both the manual and automatic approaches. The posterior condylar line, however, showed a larger deviation (1.6°) compared to the manual analysis.

This thesis aims at developing automatic approaches to extract reference points and axes from the 3D virtual skull and femur, which could be used in orthognathic surgery and TKA. Despite the growing use of 3D cephalometry and virtual surgical planning, no automatic approaches for landmark localisation on the virtual skull model have been proposed. This might be related to the complexity of the skull, which consists of many different bones, making it more difficult to analyse automatically. Applying landmark extraction techniques to the 3D model of the skull would thus be a novel approach for 3D cephalometry. Several relevant axes for TKA have been determined in literature, but a complete analysis of femoral and tibial alignment is currently lacking. Regarding the femur, Subburaj et al. extracted the mechanical, anatomical, distal condylar and anatomical transepicondylar axis. However, various other axes are used in clinical practice for measuring rotational alignment. Cerveri et al. extracted the diaphysis axis, anatomical flexion axis, anatomical transepicondylar axis, posterior condylar line and Whiteside line. A major limitation is that the diaphysis axis is defined from a best-fit cylinder to the shaft, which does not take into account femoral bowing. Also, the femoral condyles were approximated by ellipses, while several authors demonstrated the circular profile of the posterior condyles and proposed to calculate the flexion-extension axis from best-fit circles, spheres or cylinders to the flexion facets of the condyles. Finally, the mechanical axis and surgical transepicondylar axis were not determined. A more comprehensive study of femoral alignment is thus required to allow for applications in clinical practice.

2.3 Conclusions

The studies discussed in this chapter show that intra- and interobserver variability can be a limiting factor for obtaining correct measurements from 3D medical images. Differences between landmarks and anatomical directions are found and seem to be consistent among different studies. Landmarks located on relatively flat or widely curved anatomical structures and short axes are more prone to observer variability. However, precise measurements can also be obtained based on these points if the variations are small in the relevant directions. Furthermore, the reliability of manual landmark localisation may depend on the experience of the operator and might be improved through training and by using detailed landmark definitions and anatomical drawings. Finally, the reference frames proposed in literature are usually defined from the most reliable landmarks or landmark directions. By summarising the results for a set of commonly used skeletal cephalometric points it is found that 40 % of the mean 3D intraobserver values are above 1.5 mm and that 52 % of the mean 3D interobserver values are greater than 2 mm. Some of the axes of the knee were found to be very reliable, while other showed mean variations above 2°.

By reviewing the literature on automatic landmark localisation, it is seen that fully automatic approaches to process 3D multiplanar images are hard to develop. The methods can be grouped into differential operators and deformable analytical, template and statistical shape models. Compared to local differential operators, deformable models are more robust to image noise by including more a priori knowledge about the landmarks, resulting in better values for the reproducibility.

The automatic approaches seem to reduce the time spent for manual intervention and improve the landmark localisation precision. However, the amount of work published on the skull and lower limb bones is very limited. In contrast to multiplanar images, several studies on automatic analysis of 3D models of the lower limbs have been published. The most commonly used methods are curvature analysis and analytical curve and surface fitting. However, most papers describe only one or two techniques or extract only a limited amount of geometrical parameters. The most extensive work has been performed by two research groups: one presented methods for automatically measuring lower limb deformities and the other extracted several points and axes on the femur and pelvis and showed that most of the parameters were relatively close to the manual measurements (<2 mm and $2°$). However, a complete set of measurements of femoral and tibial alignment has not yet been presented. In contrast to the lower limbs, no automatic approaches for landmark localisation on the virtual skull model have been proposed.

This thesis aims at developing automatic approaches to extract reference points and axes from the 3D virtual skull and femur, which could be used in orthognathic surgery and TKA. These methods may save time for the surgeon and allow for a more objective analysis of patient data. While some landmarks are more prone to variability in both the manual and automatic method, the latter may allow for a more standardised approach. As shown in this chapter, extracting landmarks from the 3D model of the skull is a novel approach for 3D cephalometry. Finally, the current limitations in the automatic measurement of distal femoral alignment are addressed in this thesis.

References

[1] Swennen GR, Schutyser F, Barth EL, De Groeve P, De Mey A. A new method of 3-D cephalometry Part I: the anatomic Cartesian 3-D reference system. J Craniofac Surg, 17(2):314-325, 2006.

[2] Ludlow JB, Gubler M, Cevidanes L, Mol A. Precision of cephalometric landmark identification: Cone-beam computed tomography vs conventional cephalometric views. Am J Orthod Dentofacial Orthop, 136:312.e1–312.e10, 2009.

[3] Olszewski R, Cosnard G, Macq B, Mahy P, Reychler H. 3D CT-based cephalometric analysis: 3D cephalometric theoretical concept and software. Neuroradiology, 48(11):853-862, 2006.

[4] Olszewski R, Tanesy O, Cosnard G, Zech F, Reychler H. Reproducibility of osseous landmarks used for computed tomography based three-dimensional cephalometric analyses. J Craniomaxillofac Surg, 38(3): 214-221, 2010.

[5] Lagravère MO, Low C, Flores-Mir C, Chung R, Carey JP, Heo G, Major PW. Intraexaminer and interexaminer reliabilities of landmark identification on digitized lateral cephalograms and formatted 3-dimensional cone-beam computerized tomography images. Am J Orthod Dentofacial Orthop, 137(5):598-604, 2010.

[6] Schlicher W, Nielsen I, Huang JC, Maki K, Hatcher DC, Miller AJ. Consistency and precision of landmark identification in three-dimensional cone beam computed tomography scans. Eur J Orthod, 2011 Mar 8. [Epub ahead of print]

[7] Titiz I, Laubinger M, Keller T, Hertrich K, Hirschfelder U. Repeatability and reproducibility of landmarks–a three-dimensional computed tomography study. Eur J Orthod, 2011 May 12. [Epub ahead of print]

[8] Haffner CL, Pessa JE, Zadoo VP, Garza JR. A technique for three-dimensional cephalometric analysis as an aid in evaluating changes in the craniofacial skeleton. Angle Orthod, 69(4):345-348, 1999.

[9] Park SH, Yu HS, Kim KD, Lee KJ, Baik HS. A proposal for a new analysis of craniofacial morphology by 3-dimensional computed tomography. Am J Orthod Dentofacial Orthop, 129(5):600.e23-600.e34, 2006.

[10] Yoshino N, Takai S, Ohtsuki Y, Hirasawa Y. Computed tomography measurement of the surgical and clinical transepicondylar axis of the distal femur in osteoarthritic knees. J Arthroplasty, 16(4):493-497, 2001.

[11] Wai Hung CL, Wai Pan Y, Kwong Yuen C, Hon Bong L, Lei Sha LW, Ho Man SW. Interobserver and intraobserver error in distal femur transepicondylar axis measurement with computed tomography. J Arthroplasty, 24(1):96-100, 2009.

[12] Nofrini L, Slomczykowski M, Iacono F, Marcacci M. Evaluation of accuracy in ankle center location for tibial mechanical axis identification. J Invest Surg, 17(1):23-29, 2004.

[13] Victor J, Van Doninck D, Labey L, Innocenti B, Parizel PM, Bellemans J. How precise can bony landmarks be determined on a CT scan of the knee? Knee, 16(5):358-365, 2009.

[14] Subburaj K, Ravi B, Agarwal M. Automated identification of anatomical landmarks on 3D bone models reconstructed from CT scan images. Comput Med Imaging Graph, 33(5):359-368. 2009.

[15] Cerveri P, Marchente M, Bartels W, Corten K, Simon JP, Manzotti A. Automated method for computing the morphological and clinical parameters of the proximal femur using heuristic modeling techniques. Ann Biomed Eng, 38(5):1752-1766, 2010.

[16] Cerveri P, Marchente M, Bartels W, Corten K, Simon JP, Manzotti A. Towards automatic computer-aided knee surgery by innovative methods for processing the femur surface model. Int J Med Robot, 6(3):350-361, 2010.

[17] Cerveri P, Marchente M, Manzotti A, Confalonieri N. Determination of the Whiteside line on femur surface models by fitting high-order polynomial functions to cross-section profiles of the intercondylar fossa. Comput Aided Surg, 16(2):71-85, 2011.

[18] Cerveri P, Marchente M, Chemello C, Confalonieri N, Manzotti A, Baroni G. Advanced computational framework for the automatic analysis of the acetabular morphology from the pelvic bone surface for hip arthroplasty applications. Ann Biomed Eng, 39(11):2791-2806, 2011.

[19] Young IT, Gerbrands JJ, van Vliet LJ. Fundamentals of image processing, Delft PH Publications, 2007.

[20] Nixon MS, Aguado AS. Feature extraction and image processing, Newnes, 2002.

[21] Zitová B, Flusser B. Image registration methods: a survey. Image Vis Comput, 21(11):977-1000, 2003.

[22] Monga O, Benayoun S. Using partial derivatives of 3D images to extract typical surface features. Comput Vis Image Underst, 61(2):171-189, 1995.

[23] Thirion J-P, Gourdon A. Computing the differential characteristics of isointensity surfaces. Comput Vis Image Underst, 61(2):190-202, 1995.

[24] Thirion J-P, Gourdon A. The 3D marching lines algorithm. Graph Models Image Process, 58(6):503-509, 1996.

[25] Thirion J-P, Gourdon A. The 3D marching lines algorithm and its application to crest lines extraction. Research report RR-1672, INRIA, May 1992.

[26] Rohr K. On 3D differential operators for detecting point landmarks. Image Vis Comput, 15(3):219-233, 1997.

[27] Beil W, Rohr K, Stiehl HS. Investigation of approaches for the localization of anatomical landmarks in 3D medical images. In Proc CAR'97, pp. 265-270, Elsevier Science, 1997.

[28] Hartkens T, Rohr K, Stiehl HS. Performance of 3D differential operators for the detection of anatomical point landmarks in MR and CT images in: K.M. Hanson (Ed.), Proceedings of the SPIE's International Symposium on Medical Imaging 1999: Image Processing, San Diego, CA, USA vol. 3661, SPIE Press, Bellingham, WA, pp. 32-43, 1999.

[29] Frantz S, Rohr K, Stiehl HS. Development and validation of a multi-step approach to improved detection of 3D point landmarks in tomographic images. Image Vis Comput, 23(11):956-971, 2005.

[30] Frantz S, Rohr K, Stiehl HS. In: K.M. Hanson (Ed.), Refined localization of three-dimensional anatomical point landmarks using multi-step differential approaches. Proceedings of the SPIE's International Symposium on Medical Imaging: Image Processing, San Diego, CA, USA, vol. 3338, SPIE Press, Bellingham, WA, pp. 28-38, 1998.

[31] Wörz S, Rohr K. Localization of anatomical point landmarks in 3D medical images by fitting 3D parametric intensity models. Medical Image Analysis, 10(1):41-58, 2006.

[32] Alker M, Frantz S, Rohr K, Stiehl HS. Improving the robustness in extracting 3D point landmarks from 3D medical images using parametric deformable models. In: Proc. MICCAI'01, Utrecht, The Netherlands, Lect Notes Comp Sci 2208, Springer, Berlin, pp. 582-590, 2001.

[33] Frantz S, Rohr K, Stiehl HS. Localization of 3D anatomical point landmarks in 3D tomographic images using deformable models. In: Proc. MICCAI'00, Pittsburgh, Pennsylvania/USA, Lect Notes Comp Sci 1935, Springer, Berlin, pp. 492-501, 2000.

[34] Ehrhardt J, Handels H, Plötz W, Pöppl SJ. Atlas-based recognition of anatomical structures and landmarks and the automatic computation of orthopedic parameters. Methods Inf Med, 43(4):391-397, 2004.

[35] Seim H, Kainmueller D, Heller M, Lamecker H, Zachow S, Hege H-C. Automatic segmentation of the pelvic bones from CT data based on a statistical shape model. Eurographics Workshop on Visual Computing for Biomedicine (VCBM), Delft, Netherlands, pp. 93-100, 2008.

[36] Seim H, Kainmueller D, Heller, M, Zachow S, Hege H-C. Automatic extraction of anatomical landmarks from medical image data: An evaluation of different methods. Proceedings of IEEE International Symposium on Biomedical Imaging (ISBI): From Nano to Macro, Boston, MA, USA, pp. 538-541, 2009.

[37] Liu X, Kim W, Drerup B. 3D characterization and localization of anatomical landmarks of the foot by FastSCAN. Real-Time Imaging, 10(4):217-228, 2004.

[38] Subburaj K, Ravi B, Agarwal MG. 3D shape reasoning for identifying anatomical landmarks. Comput Aided Des Appl, 5(1-4):153-160, 2008.

[39] Li K, Tashman S, Fu F, Harner C, Zhang X. Automating analyses of the distal femur articular geometry based on three-dimensional surface data. Ann Biomed Eng, 38(9):2928-2936. 2010.

[40] Mahaisavariya B, Sitthiseripratip K, Tongdee T, Bohez EL, Vander Sloten J, Oris P. Morphological study of the proximal femur: a new method of geometrical assessment using 3-dimensional reverse engineering. Med Eng Phys, 24(9):617-622, 2002.

[41] Jun Y, Choi K. Design of patient-specific hip implants based on the 3D geometry of the human femur. Advances in Engineering Software, 41(4):537-547, 2010.

[42] Kim JS, Park TS, Park SB, Kim JS, Kim IY, Kim SI. Measurement of femoral neck anteversion in 3D. Part 2: 3D modelling method. Med Biol Eng Comput, 38(6):610-616, 2000.

[43] Miranda DL, Rainbow MJ, Leventhal EL, Crisco JJ, Fleming BC. Automatic determination of anatomical coordinate systems for three-dimensional bone models of the isolated human knee. J Biomech, 43(8):1623-1626, 2010.

[44] Subburaj K, Ravi B, Agarwal M. Computer-aided methods for assessing lower limb deformities in orthopaedic surgery planning. Comput Med Imaging Graph, 34(4):277-288, 2010.

[45] Gargouri I, De Guise JA. Automated method for clinic and morphologic analysis of bones using implicit modeling technique. Conf Proc IEEE Eng Med Biol Soc, pp. 5095-5098, 2007.

[46] Sholukha V, Chapman T, Salvia P, Moiseev F, Euran F, Rooze M, Van Sint Jan S. Femur shape prediction by multiple regression based on quadric surface fitting. J Biomech, 44(4):712-718, 2011.

3

Automatic approaches to 3D landmark extraction

This chapter provides an overview of the algorithms that are used in this thesis to analyse the skull and femur models. Some mesh operations to simplify, smooth and refine the 3D models and several automatic approaches for landmark extraction are discussed. As demonstrated in chapter 2, several landmark extraction methods have already been proposed by other authors. In addition, quality improving mesh operations have been widely described in the literature. Therefore, this thesis focuses on implementing and employing a variety of pre-existing mesh processing and landmark localisation tools, rather than on developing new mathematical strategies for these operations. In this chapter, the main mathematical background of the algorithms is given and each operation is illustrated using examples on the skull and femur models. When applying the automatic landmark extraction tools, however, a priori knowledge about the shape and location of the specific anatomical structures and landmarks is required. Moreover, a specific strategy needs to be developed for the (semi-)automatic analysis of each bone. This includes orienting the model in a standardised way, selecting the anatomical structures on which the landmarks are located, extracting the positions of the points and axes and deriving clinically relevant measurements. Such strategies are presented in chapters 4 and 5 for the skull and femur, respectively.

The landmark localisation techniques studied in this research are implemented using the pyFormex software (http://www.pyformex.org). pyFormex is an open-source program under development at the IBiTech-bioMMeda research group of Ghent University and is intended for generating, manipulating and operating on 3D geometrical models. The models obtained from medical images are usually triangulated surface meshes. They are defined by a set of nodes, edges and triangular faces, describing the contour of the object. The algorithms described in this chapter are developed for this particular type of geometrical models.

3.1 General mesh operations

In this section, several operations to obtain a simplified, refined or smoothed approximation of the original surface mesh are discussed. To verify that the new mesh is a good approximation of the original geometry, the error between the two triangular meshes should be measured. Therefore, a tool to quantify their geometric difference was also implemented.

3.1.1 Geometric error between triangulated surfaces

A commonly used method is to approximate the Hausdorff distance between the surfaces [1, 2]. Given points p_1 on surface S_1 and p_2 on surface S_2, the one-sided distance between the two surfaces S_1 and S_2 is defined as

$$d(S_1, S_2) = \underbrace{max}_{p_1 \in S_1} d(p_1, S_2) = \underbrace{max}_{p_1 \in S_1} [\underbrace{min}_{p_2 \in S_2} d(p_1, p_2)] \tag{3.1}$$

The two-sided Hausdorff distance is then the maximum of the non-symmetrical one-sided distances:

$$d_H(S_1, S_2) = max[d(S_1, S_2), d(S_2, S_1)] \tag{3.2}$$

A mean distance measurement between surfaces S_1 and S_2 can be obtained using the mean error of all triangle faces of S_1:

$$d_m(S_1, S_2) = \frac{\sum_{i=1}^{N} \frac{|e_{i1}|+|e_{i2}|+|e_{i3}|}{3} A_i}{\sum_{i=1}^{N} A_i} \tag{3.3}$$

where e_{ij} are the distances of the triangle's vertices to S_2 and A_i is the area of the triangle. To find the distance from S_1 to S_2, the surface S_1 is sampled and the distance $d(p_1, S_2)$ of each sample p_1 to the surface S_2 is calculated as the minimum of the distances between p_1 and all the faces F_2. The point to triangle distance $d(p_1, F_2)$ is found by first projecting the point p_1 onto the plane of F_2 and determining the position of the projected point p_1' with respect to the triangle (see

Figure 3.1) [3]. To check if p_1' lies inside or outside the triangle, it is expressed as a barycentric combination of the triangle vertices (V_0, V_1, V_2):

$$p_1' = rV_0 + sV_1 + tV_2 \tag{3.4}$$

As the barycentric coordinates (r, s, t) sum to one, this can be written as

$$p_1' = V_0 + s(V_1 - V_0) + t(V_2 - V_0) \tag{3.5}$$

Figure 3.2 and Table 3.1 give an overview of the position of p_1' with respect to the triangle for different combinations (s, t) and of the corresponding position of the closest point on the triangle. When the barycentric coordinates are not negative $(s \geq 0, t \geq 0, s + t \leq 1)$, p_1' lies in the convex hull of (V_0, V_1, V_2), i.e. inside the triangle, which corresponds to region 0. It this case, the point to triangle distance is equal to the point to plane distance (Figure 3.1 (left)). If p_1' falls outside the triangle, it is the distance to the closest edge or vertex of F_2 (Figure 3.1 (right)). Finally, a signed distance can be obtained using the normal vector N_{p_1} to S_1 in p_1. If p_1' is the closest point in S_2, the sign of the distance is the sign of $N_{p_1} \cdot (p_1' - p_1)$.

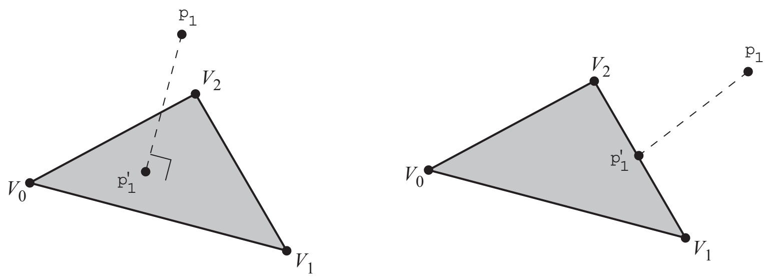

Figure 3.1: Distance between a point and a triangle: the closest point is equal to the projected point if it lies inside the triangle (left); otherwise, the closest point lies on an edge (right) or is one of the vertices, adapted from [3].

The sampling resolution of the triangles will influence the precision of the distance calculation. The sampling method is illustrated in Figure 3.3, where each side is sampled with $n = 5$ points and a regular grid is built over the triangle. As shown in the following equation, the sampling frequency n is calculated from the triangle's area A and the sampling step δ, which is expressed as a percentage of the diagonal length of the surface's bounding box [2].

$$n = \sqrt{\frac{1}{4} + \frac{2A}{\delta^2}} - \frac{1}{2} \tag{3.6}$$

The number of samples in the triangle is then

$$n_{samples} = \frac{n(n+1)}{2} = \frac{A}{\delta^2} \tag{3.7}$$

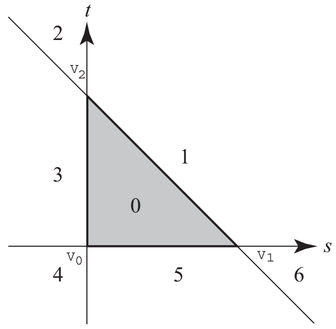

Figure 3.2: Partitioning of the triangle plane for different combinations of barycentric coordinates (s, t) of the projected point, adapted from [3].

Table 3.1: Distance between a point and a triangle: position of the projected point and closest point for different combinations of barycentric coordinates (s, t).

(s,t)	projected point	closest point
$(s \geq 0, t \geq 0, s+t \leq 1)$	in region 0	inside triangle
$(s \geq 0, t \geq 0, s+t > 1)$	in region 1	on edge V_1V_2
$(s < 0, t \geq 0, s+t > 1)$	in region 2	on edge V_1V_2 or V_2V_0
$(s < 0, t \geq 0, s+t \leq 1)$	in region 3	on edge V_2V_0
$(s < 0, t < 0, s+t \leq 1)$	in region 4	on edge V_2V_0 or V_0V_1
$(s \geq 0, t < 0, s+t \leq 1)$	in region 5	on edge V_0V_1
$(s \geq 0, t < 0, s+t > 1)$	in region 6	on edge V_0V_1 or V_1V_2

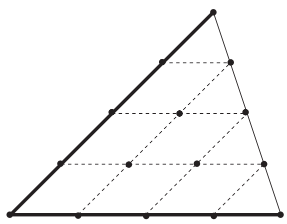

Figure 3.3: Sampling of a triange: each side is sampled with 5 points, a regular grid is built over the triangle and 15 samples are created [2].

Calculating the distance of a sample p_1 to all faces F_2 would tremendously slow down the computation for large meshes. This extensive computation can be avoided by creating a voxel grid in the bounding box of $S_1 \cup S_2$ [1, 2], which allows iterative processing of the faces. After the voxel grid is created, it is determined for each point p_1 and face F_2 in which voxel(s) they are contained, resulting in a list of points and faces for each voxel. Finally, the minimum distance between each point and the faces is calculated using the voxel information. For each point the faces contained in the same voxel are first tested and subsequently, adjacent voxels in an increasing neighbourhood are processed, until all not tested voxels are farther than the current nearest face, i.e. the minimum distance between the voxel holding p_1 and the not tested voxels is greater than the distance between p_1 and its current nearest face.

The algorithm is applied on two triangulated spheres to show the influence of the sampling step δ on the distance calculation. The mean face distance (see Equation 3.3) of a simplified mesh with 640 faces to the original mesh with 1280 faces for different sampling steps is depicted in Figure 3.4. Both the sampling step and the distance are expressed as a percentage of the diagonal length of the simplified surface's bounding box. The number of samples ranges between 322 ($\delta = 10\,\%$) and 1049411 ($\delta = 0.1\,\%$). The computation time increases from 1 to 52 seconds. Sampling steps below 0.5 % result in a stable distance measurement. The signed sample distances for $\delta = 0.1\,\%$ are shown on the mesh in Figure 3.5. Figure 3.6 shows the two surfaces, the original mesh in red and the sampled simplified mesh in grey, and illustrates that positive (negative) distances are obtained where the original mesh lies outside (inside) the simplified one.

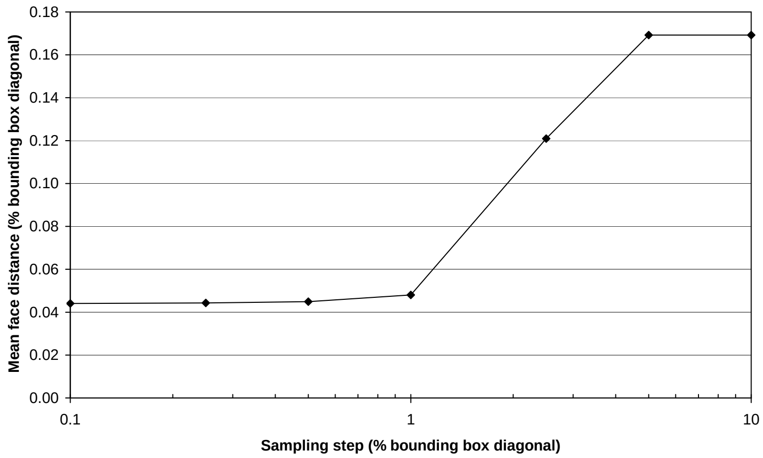

Figure 3.4: Mean face distance of a simplified sphere to the original surface as a function of the sampling step δ.

3.1.2 Simplification

Surface mesh simplification (or coarsening) is the process of reducing the number of faces in the mesh while keeping the overall shape, volume and boundaries

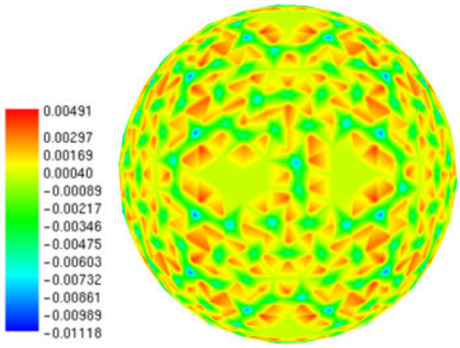

Figure 3.5: Distribution of signed sample distance (mm) on the sphere for $\delta = 0.1\,\%$.

Figure 3.6: The original mesh (red) and sampled simplified mesh (grey) plotted onto each other.

preserved as much as possible. It reduces the level of detail in the mesh, resulting in a simplified geometry that requires less processing time. A simplication algorithm proposed by Lindstrom & Turk [4], which is available in the GNU Triangulated Surface Library (GTS), is used. GTS is an open source free software library providing a set of useful functions to deal with triangulated surface models (http://gts.sourceforge.net). The GTS functions can be invoked from pyFormex by running external commands.

The algorithm uses edge collapse, as demonstrated in Figure 3.7. It iteratively replaces an edge with a single vertex, thereby removing one vertex, three edges and two faces. The ordering of the edges to be collapsed as well as the position of the new vertices are determined using volume, boundary and shape optimisation. Inserting a new vertex causes a volume change that is equal to the sum of the volumes of the tetrahedra formed by each original triangle and the new vertex (see Figure 3.7 (bottom)). A vertex placed along the outer normal of the triangle produces a positive volume change, while a vertex on the inside produces a negative volume change. Volume preservation is obtained by setting the volume change due to edge collapse to zero. In addition, the vertex position is constrained by minimizing the unsigned volume of each tetrahedron, called volume optimisation. Analogous to volume preservation and optimisation, the area enclosed by the surface boundaries is taken into account for collapsing a boundary edge. In addition, the shape of the triangles can be optimised (e.g. if no single solution is found using the previous constraints), with equilateral triangles being preferred. The cost of collapsing an edge is a weighted sum of the functions that are minimized in the volume and boundary (and shape) optimisation. The algorithm repeatedly selects the edge with minimum cost, collapses this edge, and then re-evaluates the cost of edges affected by this edge collapse.

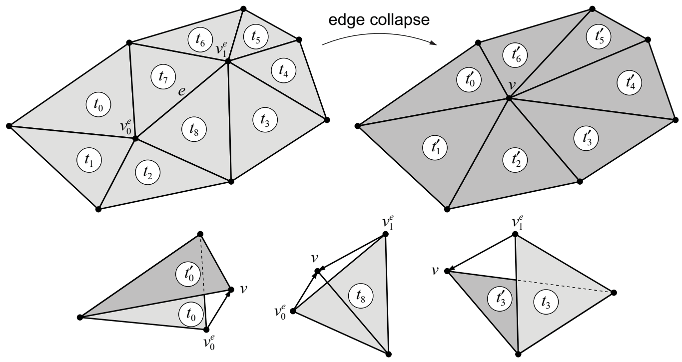

Figure 3.7: Mesh simplification using edge collapse: the edge e is collapsed and replaced with a vertex v (top); the volume change is determined from the tetrahedra formed by the triangles t_0, t_8 and t_3 and the vertex v (bottom) [4].

It has been demonstrated by the authors that their algorithm is computationally efficient and results in smaller mean geometric errors than many other published techniques [5]. In their studies, shape optimisation is only used if the solution is underconstrained after volume and boundary optimisation. However, for some landmark extraction algorithms it might be desirable to have equilateral triangles as the vertices are more uniformly spaced. By choosing a non-zero weight for the shape optimisation, the creation of elongated triangles is better avoided.

To study the effect of the simplification tool for different parameters, the algorithm was applied on a femur model with 482280 edges. The 95th percentile of the sample distance and Hausdorff distance between the original and simplified mesh was calculated and is displayed as a function of the number of edges in the simplified model in Figures 3.8 and 3.9. The model size as well as the distances are shown on a logarithmic scale. For both measures, the maximum of the one-sided values was used. The distances between the meshes were calculated using a sampling step of 0.1 %. Two different weights for the triangle shape quality were chosen: 0 and 1/3. Both figures demonstrate that a larger geometric error is introduced when the shape quality of the triangles is taken into account. The largest difference between the graphs is found for the first simplification (1/2 of the original number of edges). For a small reduction of the model size, the volume optimisation seems to result in a close match between the original and simplified meshes everywhere in the mesh (Hausdorff distance = 0.10 mm), while the shape optimisation already causes larger geometric errors (Hausdorff distance = 0.61 mm). The difference becomes smaller as the model size decreases and both volume and shape optimisation produce larger errors. The 95th percentile distances are on average 2 times larger for the 1/3 shape weight compared to the zero weight.

Figure 3.10 shows that the shape quality of the mesh is greatly improved by using

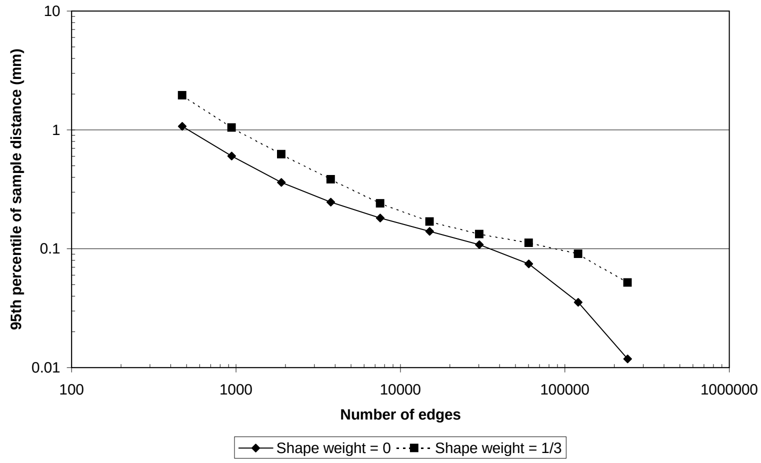

Figure 3.8: 95th percentile of the sample distance between a femur model with 482280 edges and simplified model as a function of the number of edges in the simplified mesh.

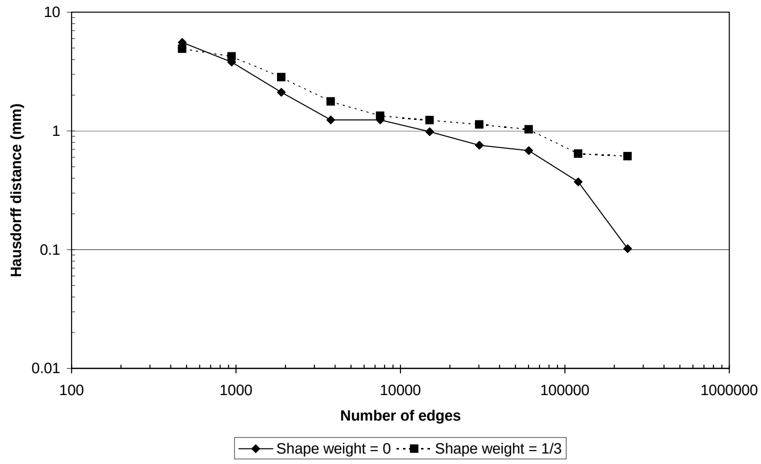

Figure 3.9: Hausdorff distance between a femur model with 482280 edges and simplified model as a function of the number of edges in the simplified mesh.

the non-zero weight for shape optimisation. A quantitative comparison is made by calculating the aspect ratio of the triangles, which is defined as the ratio of the longest edge over the smallest altitude, with equilateral triangles having the smallest value ($2/\sqrt{3} = 1.15$). The 50th and 95th percentile values are 2.61 and 8.52 for the zero shape weight versus 1.94 and 4.15 for the non-zero shape weight. These values demonstrate that the aspect ratio is greatly reduced for the majority of the triangles.

The original model and a series of meshes obtained with the shape optimisation approach are shown in Figure 3.11. The Hausdorff distance is around 1 mm for the model with 60285 edges. The 95th percentile distance however is approximately ten times smaller, which means that only a small part of the samples have a geometric error of more than 0.1 mm. The volume change for all models is below 0.002 %, which demonstrates the volume preservation constraint. The simplification time ranges between 31 and 52 seconds. These results show that the simplification tool proposed by Lindstrom & Turk allows to create simplified meshes with small geometric errors and a good triangle shape quality and has a relatively low computation time.

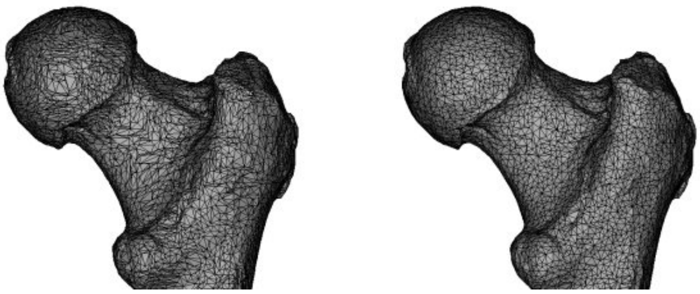

Figure 3.10: Simplified meshes with 60285 edges: zero weight for shape optimisation (left), non-zero weight for shape optimisation (right).

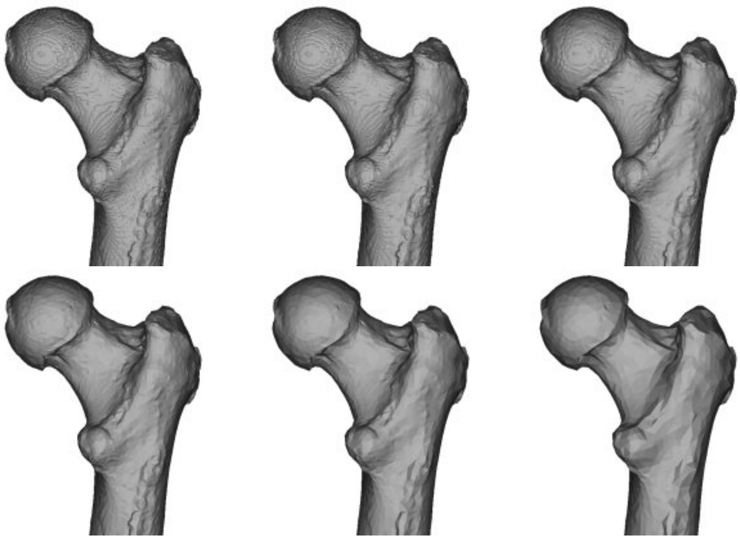

Figure 3.11: Original femur model with 482280 edges and simplified meshes with 241140, 120570, 60285, 30144 and 15072 edges.

3.1.3 Smoothing

The goal of smoothing is to remove noise and useless details from the mesh. A smoothed mesh allows to capture the most important geometrical features by filtering out the small scale features. Most smoothing algorithms modify the position of the vertices, while preserving the topology of the mesh.

3.1.3.1 Fourier analysis on meshes

The principles of smoothing can be explained by the concepts of signal processing, as shown by Taubin [6, 7]. The mesh geometry is represented by a discrete signal $x = (x_1, \ldots, x_n)$ of 3 spatial dimensions defined on the vertices of the mesh. When looking at its frequency domain representation instead of space domain representation, noise (or rapidly changing geometries) can be distinguished as high frequency components. A smoother geometry is obtained by changing the frequency contents of the mesh, i.e. by removing the highest frequency components.

The mathetical operation that decomposes a signal into its frequency components, is called the Fourier transform and is defined as

$$\mathcal{F}(k) = \int_{-\infty}^{\infty} f(x)\, e^{-i2\pi kx}\, \mathrm{d}x \tag{3.8}$$

where $f(x)$ is a continuous signal and k is the frequency. To analyze the frequencies contained in a discrete (or sampled) signal on a finite domain, such as the polygonal mesh, the discrete Fourier transform (DFT) can be employed. The DFT can be computed efficiently using a fast Fourier transform (FFT) algorithm.

$$\mathcal{F}(k) = \sum_{x=0}^{N-1} f(x)\, e^{-i\frac{2\pi}{N}kx} \tag{3.9}$$

Taubin's work is based on the observation that computing the DFT of a signal defined on a closed polygon of n vertices is equivalent to decomposing the signal as a linear combination of the eigenvectors of the Laplacian operator $\Delta f = \nabla^2 f$, where the vector of coefficients is the DFT. This is explained as follows. The one-dimensional (1D) discrete Laplacian of a polygon $x = (x_1, \ldots, x_n)$ of n vertices is given by

$$\Delta x_i = \frac{1}{2}(x_{i-1} - x_i) + \frac{1}{2}(x_{i+1} - x_i) \tag{3.10}$$

Analogously, the discrete Laplacian of a surface signal is defined as

$$\Delta x_i = \sum_{j=0}^{n-1} w_{ij}(x_j - x_i) \tag{3.11}$$

where x_j are the neighbours of x_i and the weights w_{ij} are non-negative numbers that add up to one for each vertex x_i. If we define the matrix $K = I - W$, with I the identity matrix and $W = (w_{ij})$ the matrix of weights, the Laplacian operator can be written in matrix form as

$$\Delta x = -Kx \tag{3.12}$$

Since K is symmetric, it has real eigenvalues $(k_1, \ldots, k_n)$ and a set of orthonormal eigenvectors $(e_1, \ldots, e_n)$, which form a basis. Any vector of size n can be expressed as a linear sum of these basis vectors. In particular, the mesh signal x can be written as

$$x = \sum_{i=1}^{n} \hat{x}_i \, e_i \tag{3.13}$$

As mentioned above, it has been shown that the eigenvectors of the 1D discrete Laplacian coincide with the complex exponential basis functions used in the DFT, i.e. the vector of coefficients $\hat{x}_i$ form the DFT of x [8]. The eigenvectors can be considered as the natural vibration modes of the discrete surface signal, and the corresponding eigenvalues as the associated natural frequencies. A vibration mode of high natural frequency then corresponds to a rapid oscillation in the space domain. The first 8 eigenvectors of the 1D discrete Laplace operator for $n = 401$ are shown in Figure 3.12. As the eigenvalue increases, the eigenvectors start to oscillate as sinusoidal curves at higher and higher frequencies [9].

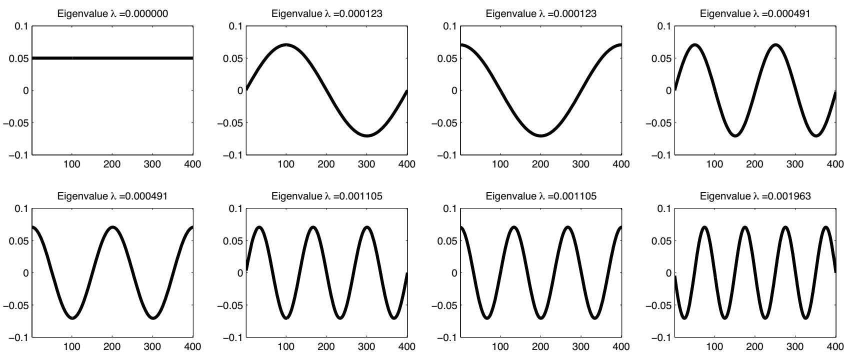

Figure 3.12: Decomposition of the mesh signal in the frequency domain: plots of the first 8 eigenvectors of the 1D discrete Laplace operator (n = 401) [9].

Fourier analysis thus allows to denoise the signal by decomposing it according to Equation 3.13 and discarding its high frequency coefficients. But for large meshes, there are no analytic expressions for the eigenvalues and eigenvectors of K and it is almost impossible to reliably compute them [7]. However, for filtering operations it is not necessary to compute the eigenvectors explicitly. The signal can be filtered by changing its frequency distribution according to an analytical transfer function

$f(k)$ that can be evaluated in the matrix K:

$$x' = \sum_{i=1}^{n} f(k_i)\,\hat{x}_i\,e_i = f(K)\,x \tag{3.14}$$

where $f(K)$ is a matrix with the same eigenvectors as K, but with eigenvalues $(f(k_1), \ldots, f(k_n))$. If this process is repeated N times, the output signal can be expressed as

$$x^N = f(K)^N x \tag{3.15}$$

3.1.3.2 Laplacian smoothing

A common method for smoothing polygonal meshes is Laplacian smoothing, which iteratively moves each vertex towards a weighted average of its neighbouring vertices:

$$x_i' = x_i + \lambda \Delta x_i = x_i + \lambda \sum_{j=0}^{n-1} w_{ij}(x_j - x_i) \tag{3.16}$$

where Δx_i is the discrete Laplacian, x_j are the neighbours of x_i (i.e. vertices connected to it by an edge), n is the valence (number of edges connected to x_i), w_{ij} are non-negative weights that add up to one and λ is a scale factor ($0 < \lambda < 1$). However, Laplacian smoothing produces shrinkage and in the limit all the vertices of the mesh converge to one point. The shrinkage problem can be explained by the concepts of signal processing. Based on Equations 3.16 and 3.12, the Laplacian smoothing step can be described in matrix form as follows

$$x' = x + \lambda \Delta x = (I - \lambda K)x \tag{3.17}$$

which means that the transfer function of the Laplacian filter is the polynomial $f(k) = 1 - \lambda k$. In Figure 3.13 (left), the Laplacian filter for $\lambda = 0.5$ and $N = 2$ is shown. For certain choices of weights (e.g. inverse of the valence, inverse of the edge length), the eigenvalues are $0 \leq k_1 \leq k_2 \leq \ldots \leq k_n \leq 2$. The filter produces shrinkage because all the frequency components, other than the zero component, are attenuated ($|f(k)^N| < 1$ for $0 < k \leq 2$).

3.1.3.3 $\lambda|\mu$ algorithm

Taubin [6] proposed the following second degree transfer function to solve the problem of shrinkage:

$$f(k) = ((1 - \lambda k)(1 - \mu k))^{1/2} \tag{3.18}$$

This filter alternates between two steps of Laplacian smoothing: a shrinking step with positive scale factor λ and an unshrinking step with negative scale factor μ,

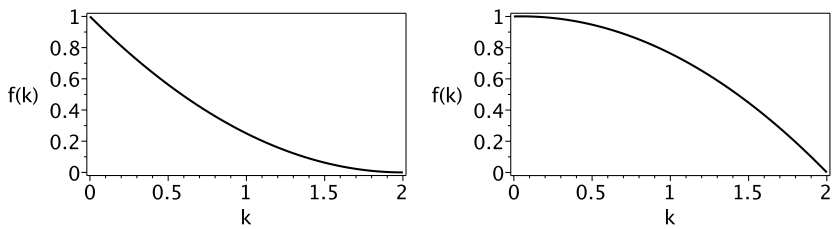

Figure 3.13: Transfer functions that change the frequency distribution of the mesh signal: Laplacian smoothing (left) and $\lambda|\mu$ algorithm (right); the scale factor $\lambda = 0.5$ and the number of iterations $N = 2$.

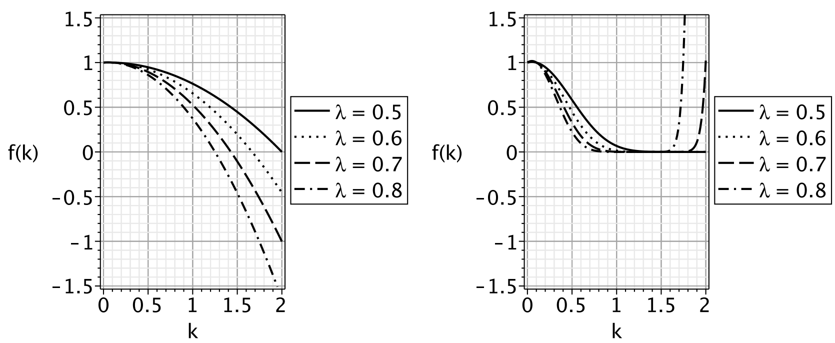

Figure 3.14: Transfer function of the $\lambda|\mu$ algorithm for different scale factors λ: $N = 2$ (left) and $N = 20$ (right).

greater than λ in absolute value ($\mu < -\lambda < 0$). Since $f(0) = 1$ and $\mu + \lambda < 0$, there is a positive value k_{PB}, such that $f(k_{PB}) = 1$, which is called the pass-band frequency and is given by

$$k_{PB} = \frac{1}{\lambda} + \frac{1}{\mu} \tag{3.19}$$

A typical value for k_{PB} is 0.1 [7]. The transfer function for $k_{PB} = 0.1$, $\lambda = 0.5$ and $N = 2$ is shown in Figure 3.13 (right). The filter preserves low frequency components ($(f(k)^N \approx 1$ in the pass-band region $0 \leq k \leq k_{PB}$) and attenuates higher frequency components ($|f(k)^N| < 1$ in the stop-band region $k_{PB} < k \leq 2$) and is therefore called a low-pass filter. The faster the transfer function decreases in the stop-band region, the better. As illustrated in Figure 3.14, a sharper filter can be obtained by increasing the scale factor λ or the number of iterations N. However, in order to have a low-pass filter, it is necessary that $f(2) > -1$, which results in the following constraint:

$$\lambda < \frac{-k_{PB} + \sqrt{(2 - k_{PB})^2 + 4}}{2(2 - k_{PB})} \tag{3.20}$$

For $k_{PB} = 0.1$, λ should be below 0.7 to avoid that high frequencies are enhanced instead of attenuated. This can also be observed in Figure 3.14, where instability starts to develop at the highest frequencies if λ exceeds this value.

The algorithm was again applied on a femur model to compare the Laplacian smoothing and $\lambda|\mu$ algorithm and to study the influence of the number of iterations on the geometric error and volume change. The femur mesh has a model size of 33336 vertices, 100002 edges and 66668 faces. The pass-band frequency k_{PB} was set to 0.1, as proposed by Taubin. A scale factor λ of 0.5 was chosen, which means that higher frequencies are better attenuated as the filters go to zero for $k = 2$. The scale factor μ can then be calculated from Equation 3.19 and is -0.526. The weights w_{ij} were calculated as the inverse of the valence. The 95th percentile of the sample distance and Hausdorff distance for the $\lambda|\mu$ algorithm is shown in Figure 3.15. The number of smoothing iterations ranges between 2 and 20. The maximum calculation time is 6 seconds. The graph illustrates that small geometric errors are obtained using this algorithm. For 20 iterations, the Hausdorff and 95th percentile distances are 1.02 mm and 0.15 mm.

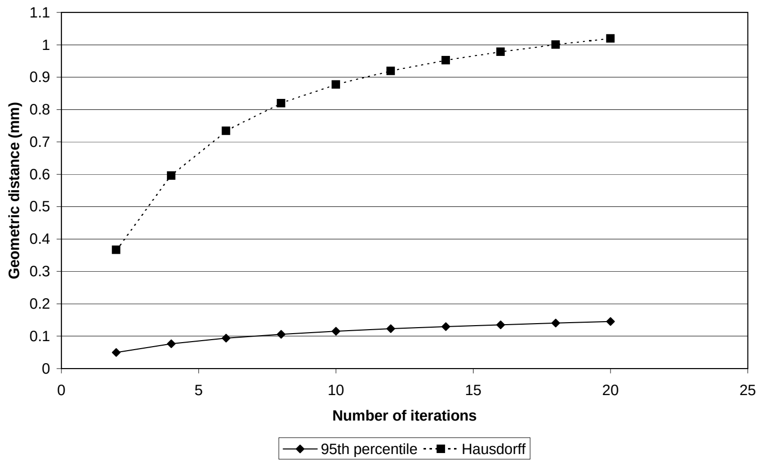

Figure 3.15: 95th percentile and Hausdorff distance between the original and $\lambda|\mu$ smoothed mesh as a function of the number of smoothing iterations.

A comparison between the two smoothing filters is made in Figures 3.16 and 3.17. Both the 95th percentile distance and the volume change are much larger for the Laplacian smoothing algorithm. While Laplacian smoothing causes severe shrinking, Taubin's low-pass filter slightly expands the mesh, because the frequencies in the pass-band region are actually enhanced. This can also be seen from the fact that the negative scale factor μ is greater in absolute value than the positive scale factor λ. The volume change will increase as the pass-band frequency gets larger and the absolute value of μ increases. For the parameters chosen above, the volume change is below 0.08 %.

The appearance of the mesh after different numbers of iterations of the $\lambda|\mu$ algorithm (0, 4, 8, 12, 16, 20) is shown in Figure 3.18. It can be seen that the effect of additional smoothing decreases as the number of iterations gets larger. The

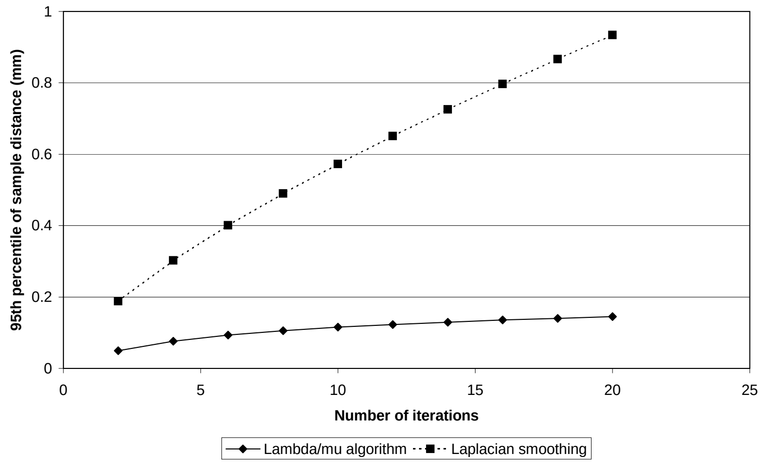

Figure 3.16: 95th percentile distance between the original and smoothed mesh for the $\lambda|\mu$ algorithm and Laplacian smoothing algorithm.

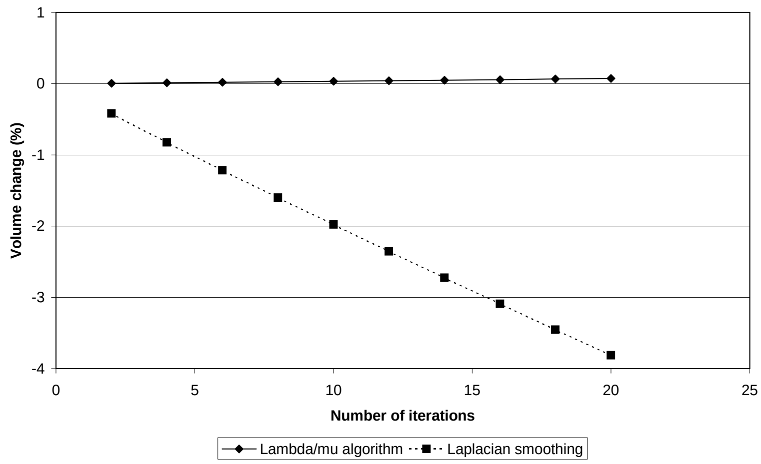

Figure 3.17: Volume change between the original and smoothed mesh for the $\lambda|\mu$ algorithm and Laplacian smoothing algorithm.

smoothness can be evaluated quantitatively using the edge angle, i.e. the angle between the normal vectors of the two faces adjacent to an edge. The 50th percentile angles are 5.12°, 3.22°, 2.77°, 2.60°, 2.55° and 2.50° respectively. The greatest improvement is found for the first iterations and the edge angle is reduced by 50 % after 16 iterations.

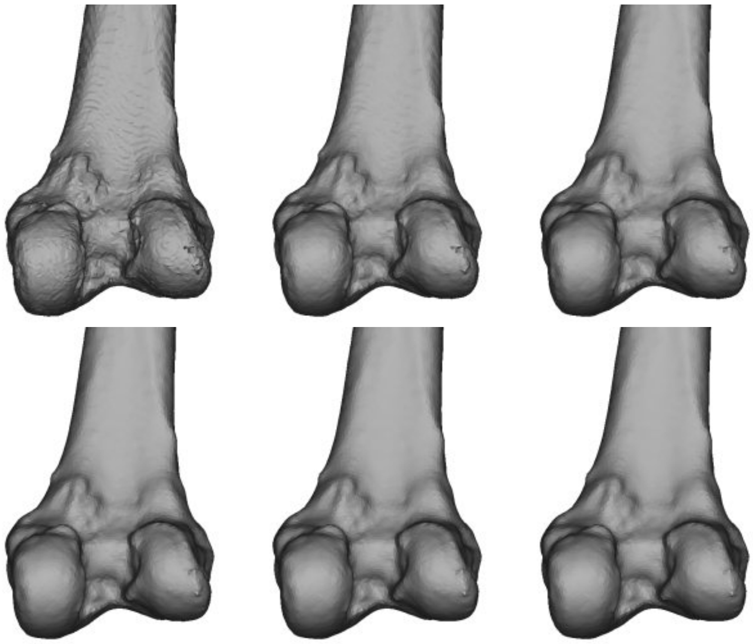

Figure 3.18: Original femur model and $\lambda|\mu$ smoothed meshes after 4, 8 ,12, 16 and 20 iterations.

3.1.3.4 Gaussian smoothing

Laplacian smoothing is sometimes called Gaussian smoothing, a method which is commonly used to smooth or blur a 2D image. Gaussian smoothing is applied by convolving the signal with a Gaussian function. The convolution of f and g is defined as the integral of the product of the two functions, one being reflected and shifted

$$(f * g)(x) = \int_{-\infty}^{\infty} f(t)\, g(x-t)\, \mathrm{d}t \tag{3.21}$$

For a discrete function, this becomes

$$(f * g)(x) = \sum_{t=-\infty}^{\infty} f(t)\, g(x-t) \tag{3.22}$$

The convolution of the input signal $f(x)$ with a filter or kernel $g(x)$ will thus calculate the output signal at each point as a weighted average of the input signal's values. The weights are defined by the filter $g(x)$. A similar strategy is applied during Laplacian mesh smoothing, where each vertex is computed using a weight $1-\lambda$ for the vertex itself and a weight λw_{ij} for the neighbouring vertices (see Equation 3.16).

The Gaussian filter, in one dimension, is defined as

$$G(x,\sigma) = \frac{1}{\sqrt{2\pi}\sigma}\, e^{-\frac{x^2}{2\sigma^2}} \tag{3.23}$$

where σ is the standard deviation, which determines the width of the kernel. Figure 3.19 (left) shows the graphs of the Gaussian kernel for $\sigma = 1$, $\sigma = 2$ and $\sigma = 3$. The constant $\frac{1}{\sqrt{2\pi}\sigma}$ normalizes the kernel (its integral over the full domain is one), which ensures that the average signal's value remains the same. In the Gaussian filter, the highest weight is assigned to the original point and the weight decreases as the distance of the neighbouring point to the original point increases. While in theory the entire input signal should be included in the calculation of each output value, in practice, the weights of the points at a distance of more than 3σ are small enough to be considered zero. This is also observed in Figure 3.19 (left). In N dimensions, the Gaussian filter is formed by the product of the Gaussians in each dimension

$$G(\vec{x},\sigma) = \frac{1}{(\sqrt{2\pi}\sigma)^N}\, e^{-\frac{|\vec{x}|^2}{2\sigma^2}} \tag{3.24}$$

The effect of the convolution can be easily understand using the frequency domain. The Fourier transform of a Gaussian with variance σ^2 is another Gaussian with

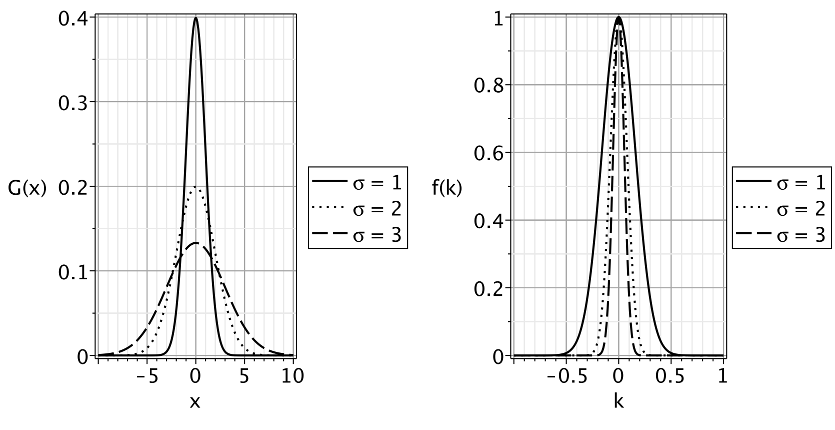

Figure 3.19: Gaussian function and transfer function for different values of the standard deviation σ.

variance $1/\sigma^2$:

$$f(k,\sigma) = e^{-2\pi^2\sigma^2 k^2} \tag{3.25}$$

As convolution in the time domain is equivalent to multiplication in the frequency domain, the frequencies are filtered with a Gaussian function, which reduces the high frequency components, as shown in Figure 3.19 (right). A sharper filter is obtained by increasing the standard deviation, as a wider kernel in the spatial domain gives a smaller kernel in the frequency domain (and vice versa). Because Gaussian smoothing also produces shrinkage, it was not used to smooth the surface meshes. However, the Gaussian convolution can be applied to compute smoothed derivatives of the input signal, and therefore also smoothed curvature values, as shown later on in this chapter.

3.1.4 Subdivision

Subdivision is the process of producing successive refinements of an initial polygonal control mesh that converges to a smooth limit surface. In each step, new vertices and faces are created that better approximate the smooth surface. New vertices are computed as weighted sums of nearby vertices. While interpolating schemes match the original data exactly, approximating schemes will adjust the original position of the vertices.

Dyn, Levin and Gregory introduced an interpolating scheme, named the Butterfly scheme, to generate a smooth surface over a regular triangular mesh (all vertices have valence 6) [10]. The scheme recursively transforms each triangular face of the control mesh into a patch consisting of four triangular faces interpolating the old vertices (see Figure 3.20). A new vertex is inserted on each edge using the weights in an eight-point stencil (Butterfly scheme), which was later extended to a ten-point rule [12], as depicted in Figure 3.21. The weights are given by

$$a = \frac{1}{2} - w, b = \frac{1}{8} + 2w, c = -\frac{1}{16} - w, d = w \tag{3.26}$$

The weights are chosen so that the limit surface is C^1 continuous, i.e. has continuous tangent planes, if $w \in [-\frac{1}{16}, 0]$. The parameter w serves as a tension parameter: as w decreases, the limit surface is more tightened toward the control mesh.

Because the Butterfly scheme only leads to C^1 surfaces for vertices of valence 6, this work was extended by Zorin, Schröder and Swelden [13]. They modified the scheme so that it guarantees C^1 continuity for triangulations which are not topologically restricted [14], including the proper handling of boundaries. They distinguish between ten cases, depending on the characteristics of the edges that are subdivided (boundary or interior edge, boundary or interior vertices, valence of the vertices) and proposed seven types of rules [15].

Figure 3.22 shows how a smooth sphere is obtained after three iterations of the subdivision algorithm. A quantitative evaluation of the C^1 continuity can be made

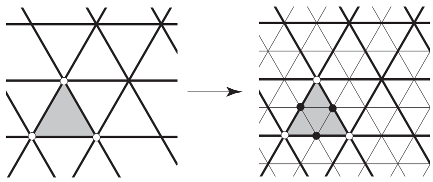

Figure 3.20: Subdivision of triangular faces: each triangle is split into a patch consisting of four triangles [11].

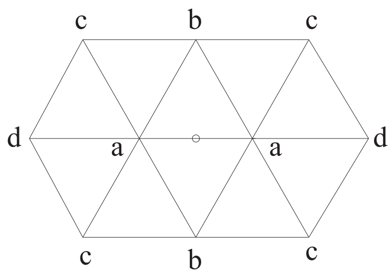

Figure 3.21: Subdivision rule for regular vertices: ten-point stencil [13].

using the edge angle. The 50th and 95th percentile values are 5.43° and 5.73° for the original sphere versus 0.65° and 0.80° after three subdivision iterations. The algorithm thus allows for a smooth refinement of the surface mesh. The computation time for the sphere with 1280 faces is 23 seconds.

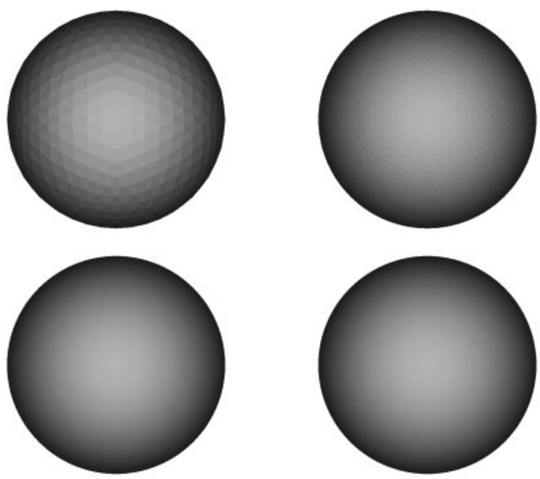

Figure 3.22: Original sphere model and subdivided meshes after 1, 2 and 3 iterations.

3.2 Extreme point

A straightforward method to extract landmarks is to find the extreme point of a certain anatomical structure using the anatomical directions. Many landmarks have been described in literature using such a definition. Such extreme points may lie in a convex- or concave-shaped anatomy, such as a large prominence on the bone. Figure 3.23 shows an example for the mastoid process, a conical prominence on the temporal bone of the skull, which holds the landmark mastoid on its inferior end. Several saddle-shaped structures are also found in the human bones, which follow a convex curve along one axis and a concave curve along another perpendicular axis. An example is given in Figure 3.24 for the frontonasal suture, which is the junction of the frontal and nasal bones of the skull. The landmark nasion is the central point of this suture, where the anatomy has a convex shape along the transverse axis and a concave shape along the longitudinal axis.

3.2.1 Convex- and concave-shaped anatomy

For convex/concave structures, the extreme point along one of the anatomical directions is computed as the mesh vertex for which the length of the projection on the direction vector is maximal. However, it should be noticed that using this method the accuracy of the landmark extraction will depend on the size of the triangle faces. A fine mesh should be used to increase the number of candidates for the landmark point. But reducing the face size of the complete bone model may drastically increase the processing time and is inefficient as only a fine grid in the neighbourhood of the landmark is needed. Therefore, it is chosen to select the anatomical structure that holds the landmark on the coarser mesh of the bone and then refine the mesh of the anatomical structure before calculating the landmark. The same method can be used for the smoothing operation as for large models, such as those of the skull, this will reduce the computation time. The vertices are smoothed using Taubin's $\lambda|\mu$ algorithm, which has shown to result in only small geometric errors. The triangles are subdivided according to the algorithm proposed by Dyn et al. and modified by Zorin et al., which allows for a smooth interpolation between the mesh vertices. The mastoid process with coarse mesh is shown in the top left panel of Figure 3.23. The meshes after 20 smoothing iterations and 3 subdivision iterations are shown in the right and bottom panels. The mean length of the edges in the final model is around 0.1 mm. As shown in the bottom panel, the landmark mastoid is calculated as the most inferior point of the structure.

3.2.2 Saddle-shaped anatomy

As mentioned above, saddle-shaped anatomies are curved differently along different directions. Two orthogonal axes can be found along which the surface is respectively convex- and concave-shaped. Therefore, a series of intersections along

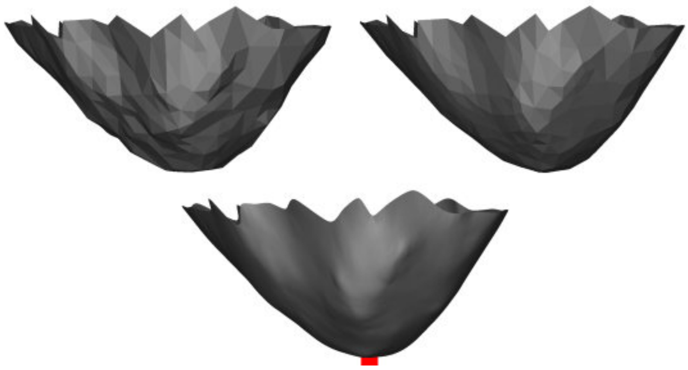

Figure 3.23: Extraction of extreme point of the mastoid process: coarse mesh (top left), smooth mesh (top right), refined mesh and most inferior point (bottom).

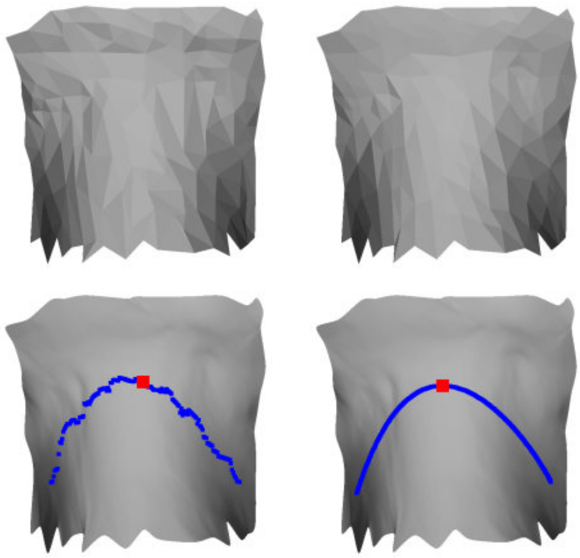

Figure 3.24: Extraction of extreme point of the frontonasal suture: coarse mesh (top left), smooth mesh (top right), refined mesh, frontonasal suture and most anterior point using discrete points (bottom left) and splines (bottom right).

one of these directions is first made and the extreme points of the cross sections are calculated. Next, the landmark is found as one of these extreme points. This is illustrated in Figure 3.24 for the frontonasal junction, where a series of intersections along the transverse axis is made and the most posterior points of these 2D cross sections are calculated (blue points in bottom left panel). The landmark nasion is then found as the most anterior point of this suture. However, it can be seen in the figure that using this method a number of discrete points are obtained and that there are some gaps between the points because of the limited smoothness of the model. If such gaps occur in the neighbourhood of the landmark, its position may largely depend on how the surface was discretised in the initial mesh. Therefore, another approach was added, where a smooth spline is calculated from the points (blue curve in bottom right panel). First, multiple natural cubic splines are generated using different series of equidistant points. The splines consist of multiple curves that are joined together with C^2 continuity at the points. Then, a mean curve is computed from all these splines. Using this method the influence of outliers is reduced as the result does not depend on a small selection of sagittal cross sections.

3.2.3 Standardised orientation

When using the extreme point method, it should be taken into account that the landmark point will depend on the orientation of the surface mesh. Because the bones are not oriented in a standardised way during CT scanning, the coordinate axes of the model do not coincide with the anatomical directions. To account for this random orientation, a standardised coordinate system should be set up from the surface mesh. If the coordinate system itself is defined based on extreme landmark points, an iterative approach should be used. The orientation of the bone (or corresponding anatomical directions) is adjusted based on the extracted landmarks and then the landmarks are recalculated using the new coordinate system. This process is repeated until the landmark coordinates are stable.

3.3 Curvature

Landmarks are often found as a prominence rather than as a discrete point. Such prominences can sometimes be seen as regions of high curvature compared to the nearby anatomy. The curvature characteristic measures how fast the geometry is changing direction at a given point. Sharp corners or ridges will thus have high curvature values. From this intuitive definition, it can be seen that the curvature does not depend on the orientation of the object. This allows determining the landmarks without setting up a standardised coordinate system. This section describes several methods to compute and process the curvature values of 3D curves and surfaces.

3.3.1 3D curves

The curvature at a given point p on a smooth 2D curve is defined as the inverse of the radius of the osculating circle at p (circle that best approximates the curve near

p). It is a measure of how fast the unit tangent vector to the curve rotates. For a 3D curve, the osculating circle in the plane containing the tangent and normal vector (osculating plane) should be considered. If $\gamma(s)$ is the arclength parametrisation of the curve $\gamma(u)$, then the unit tangent vector $T(s)$, curvature $k(s)$ and unit normal vector $N(s)$ are given by

$$T(s) = \dot{\gamma}(s) \tag{3.27}$$

$$k(s) = ||\dot{T}(s)|| = ||\ddot{\gamma}(s)|| \tag{3.28}$$

$$N(s) = \frac{\dot{T}(s)}{||\dot{T}(s)||} \tag{3.29}$$

A more general expression for the curvature of $\gamma(u)$, where the parameter u does not need to be the arclength, is

$$k(u) = \frac{||\dot{\gamma}(u) \times \ddot{\gamma}(u)||}{||\dot{\gamma}(u)||^3} \tag{3.30}$$

This definition of curvature can for example be applied on the 2D polylines that are obtained when the mesh is intersected with or projected onto a plane. An example is shown in Figure 3.25, where the femur is projected onto the transverse plane (top left). A cubic Bezier spline interpolating the polyline vertices with C^1 continuity could be created. After computing the derivatives of the third degree function, Equation 3.30 can then be evaluated at the polyline vertices. A disadvantage of this method is that if the polyline parts are small, so will the Bezier parts and the resulting curvature values will contain a lot of noise. This is illustrated in the top right panel, where the color scale was clipped to remove outliers. A better solution would be to fit a spline with a limited number of Bezier parts to the polyline vertices. Such fitting algorithm would produce a smoother spline and thus smoother curvature values. However, this method requires that the control points are estimated and optimised during the fitting algorithm.

A simpler approach is to use the properties of the convolution operator to smooth the curvature values. It was already shown that the Gaussian convolution kernel can be applied to obtain a set of smoothed points. Moreover, the convolution operator commutes with differentiation, which means that smoothed derivatives can be calculated by convolution with the derivative of the Gaussian filter:

$$\frac{d}{dx}(f * G) = \frac{df}{dx} * G = f * \frac{dG}{dx} \tag{3.31}$$

This property can be used to calculate a smoothed curvature for a 3D parametric curve $\gamma(u) = (x(u), y(u), z(u))$. The derivates of $\gamma(u)$ are obtained by convolution with the derivatives of the Gaussian kernel $G(u, \sigma)$:

$$\dot{x}(u, \sigma) = x(u) * \dot{G}(u, \sigma) \tag{3.32}$$

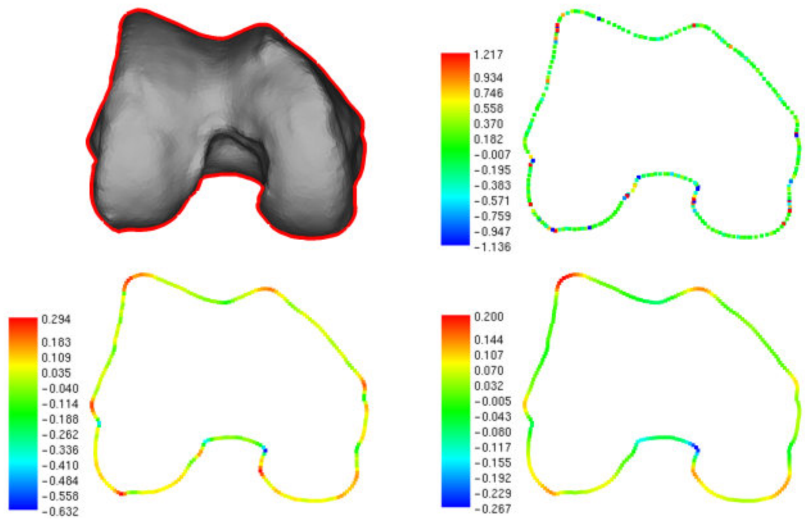

Figure 3.25: Curvature of 2D projection of the femur onto the transverse plane (top left): using Bezier spline interpolating the vertices (top right), Gaussian filter with $\sigma = 1$ (bottom left) and Gaussian filter with $\sigma = 3$ (bottom right).

$$\ddot{x}(u, \sigma) = x(u) * \ddot{G}(u, \sigma) \tag{3.33}$$

Analogous expressions are used for the y and z coordinates. The smoothed curvature is then calculated as

$$k(u, \sigma) = \frac{||\dot{\gamma}(u, \sigma) \times \ddot{\gamma}(u, \sigma)||}{||\dot{\gamma}(u, \sigma)||^3} \tag{3.34}$$

The 1D Gaussian filter implemented in the SciPy library (http://www.scipy.org) is used, which works on a 1D array of data. Therefore, a series of equidistant points is first calculated from the polyline. The amount of smoothing depends on the standard deviation σ. In the bottom part of Figure 3.25 the result for $\sigma = 1$ and $\sigma = 3$ is shown. The points are approximately 1 mm apart. Positive curvature values correspond to convex parts, while negative values represent concave parts. It can be seen that $\sigma = 3$ produces a smooth colormap, where the most convex and concave regions can be clearly distinguished.

The next step in the landmark extraction process is to quantitatively determine the points of maximum or minimum curvature. It can be seen in Figure 3.25 that some local extrema are present in the 2D curve. These can be found by calculating the minimum/maximum in a symmetric region around each point. The extrema are located where the output local minimum/maximum value is equal to the input value. The number of extrema and their location depends on the size of the neighbourhood that is considered around each point. By imposing additional constraints on where the point should approximately be located, the landmark lying in a certain anatomical region can be found. An example is given in Figure 3.26 for the lateral and medial epicondyles and the deepest point of the trochlea.

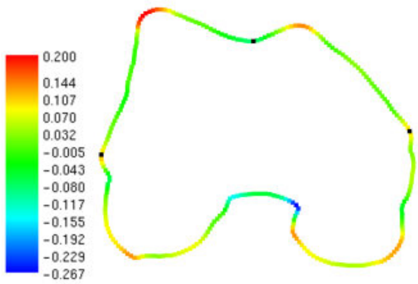

Figure 3.26: Extraction of landmarks as points with local maximum or minimum curvature: lateral and medial epicondyles and deepest point of trochlea.

3.3.2 3D surfaces

As mentioned in the previous section, a 3D surface is usually curved differently in different directions. The normal curvature k_n along a given direction t in the tangent plane is defined as the curvature of the normal curve, obtained by intersecting the surface with the plane spanned by t and the surface normal vector n. The principal curvatures k_1 and k_2 are defined as the maximum and minimum normal curvatures and the principal curvature directions are the corresponding directions in the tangent plane. The normal curvature for the direction t forming an angle θ with the first principal curvature direction is then given by the Euler curvature formula:

$$k_n(\theta) = k_1 cos^2(\theta) + k_2 sin^2(\theta) \tag{3.35}$$

The principal curvature values and directions of the surface $\gamma(u, v)$ can be calculated as the eigenvalues and eigenvectors of the matrix of second order partial derivatives or Hessian matrix:

$$H = \begin{bmatrix} \gamma_{uu} & \gamma_{uv} \\ \gamma_{vu} & \gamma_{vv} \end{bmatrix} \tag{3.36}$$

3.3.2.1 Curvature estimation on triangular meshes

Dong and Wang [16] described a method to calculate curvature values at the vertices of a triangulated surface mesh. The normal curvature is estimated based on the adjacent surface normal information and the principal curvatures are determined using the Euler curvature formula. For a vertex p with unit surface normal

N and a nearby vertex p_i with unit surface normal N_i, the normal curvature is approximated as

$$k_n(t_i) = \frac{(p_i - p) \cdot (N_i - N)}{||p_i - p||^2} \tag{3.37}$$

where t is the unit length projection of the vector $p_i - p$ onto the tangent plane:

$$t_i = \frac{(p_i - p) - ((p_i - p) \cdot N)N}{||(p_i - p) - ((p_i - p) \cdot N)N||} \tag{3.38}$$

The unit surface normal at a vertex is calculated as a weighted average of the normals to the triangular faces adjacent to that vertex. They illustrate this approximation for a sphere with radius R, where the vectors $p_i - p$ and $N_i - N$ are parallel, as shown in Figure 3.27, and the normal curvature is equal to the inverse of the radius:

$$k_n(t_i) = \frac{(p_i - p) \cdot (N_i - N)}{||p_i - p||^2} = \frac{||N_i - N||}{||p_i - p||} = \frac{1}{R} \tag{3.39}$$

The points p_i are the vertices connected to p via a shortest path of n edges, which is also called the n-ring neighbourhood of p. If the edges are short, the 1-ring neighbourhood might result in a very local and noisy curvature map and it might thus be useful to take a larger neighbourhood to obtain better results.

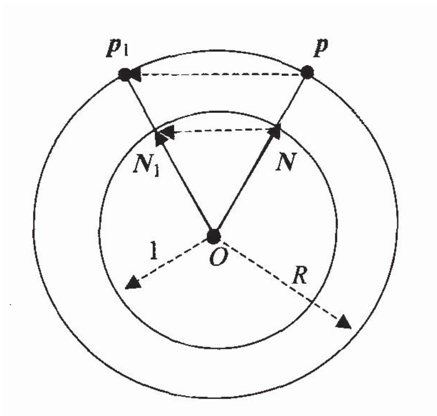

Figure 3.27: Normal curvature calculation for a triangular mesh: illustration for a sphere with radius $1/R$ *[16].*

To calculate the principal curvatures, a coordinate system $\{\hat{e}_1, \hat{e}_2\}$ on the tangent plane is chosen so that $\hat{e}_1$ is the direction corresponding to the maximum value of the normal curvatures $k_n(t_i)$. If θ_0 is the angle between $\hat{e}_1$ and the first principal direction and θ_i is the angle between $\hat{e}_1$ and t_i, then the normal curvature is given by the Euler curvature formula:

$$k_n(t_i) = k_1\, cos^2(\theta_i - \theta_0) + k_2\, sin^2(\theta_i - \theta_0) \tag{3.40}$$

This formula can be rewritten as

$$k_n(t_i) = a\,cos^2(\theta_i) + b\,cos(\theta_i)sin(\theta_i) + c\,sin^2(\theta_i) \tag{3.41}$$

where the constants a, b, c are given by

$$\begin{cases} a = k_1\,cos^2(\theta_0) + k_2\,sin^2(\theta_0) \\ b = 2(k_2 - k_1)\,cos(\theta_0)sin(\theta_0) \\ c = k_1\,sin^2(\theta_0) + k_2\,cos^2(\theta_0) \end{cases} \tag{3.42}$$

As a is chosen to be the normal curvature in the direction $\hat{e}_1$, b and c can be calculated by elimination from

$$\sum_{i=1}^{m} k_n(t_i) - a\,cos^2(\theta_i) = \sum_{i=1}^{m} b\,cos(\theta_i)sin(\theta_i) + c\,sin^2(\theta_i) \tag{3.43}$$

Finally, the angle θ_0 and the principal curvatures and corresponding directions can be calculated from these constants.

3.3.2.2 Shape classification

While landmarks on a curve can be determined based on local maximum or minimum values of the curvature, landmarks on a 3D surface are obtained by looking at the combination of both principal curvatures. The surface points can then be classified into different shapes:

- Elliptic ($k_1\,k_2 > 0$): both principal curvatures have the same sign. The surface is locally convex or concave.
- Umbilic ($k_1\,k_2 > 0$, $k_1 = k_2$): both principal curvatures have the same sign and are equal. Every tangent vector can be considered a principal direction. The surface is locally spherical.
- Hyperbolic ($k_1\,k_2 < 0$): the principal curvatures have opposite signs. The surface is locally saddle shaped.
- Minimal ($k_1\,k_2 < 0$, $k_1 = -k_2$): the principal curvatures have opposite signs and equal magnitude.
- Parabolic ($k_1 = 0$, $k_2 \neq 0$): one of the principal curvatures is zero. The surface is locally flat in one direction. Parabolic points generally lie on the boundaries between elliptical and hyperbolic regions.
- Flat ($k_1 = k_2 = 0$): both principal curvatures are zero. Every tangent vector can be considered a principal direction. The surface is locally flat.

In addition, other curvature parameters that allow for shape classification can be calculated from the principal curvature values.

Gaussian (K) and mean (H) curvatures
These quantities can be calculated using the following equations:

$$K = k_1 \, k_2 \tag{3.44}$$

$$H = \frac{k_1 + k_2}{2} \tag{3.45}$$

Also, K can be calculated as the determinant of the Hessian matrix and H is equal to half of the trace of this matrix. While K classifies the surface as locally elliptic, hyperbolic or parabolic, H allows to measure the convexity and concavity of the surface. This is illustrated in Table 3.2. As it is practically impossible to have zero H and K values in the mesh, thresholds should be used to decide whether the values are zero or not [17]. Both parameters are orientation invariant, as they depend solely on the principal curvatures. However, since the principal curvatures change when the surface is scaled, they are not scale invariant.

Table 3.2: Shape classification based on Gaussian (K) and mean (H) curvatures.

	$K < 0$ (hyperbolic or minimal)	$K = 0$ (parabolic or flat)	$K > 0$ (elliptic or umbilic)
$H < 0$	saddle valley	valley	concave
$H = 0$	minimal	plane	not possible
$H > 0$	saddle ridge	ridge	convex

Figure 3.28 demonstrates the curvature calculation on the junction between the frontal and nasal bones. This region is concave-shaped along the longitudinal axis and convex-shaped along the transverse axis. Usually, the curvedness is larger along the longitudinal axis, which means that it is shaped as a saddle valley. The colormap for the mean curvature H on the mesh obtained after 20 smoothing iterations and 3 subdivision iterations is shown in the left part of the figure. An 8-ring neighbourhood of vertices was used to calculate the curvature values for each vertex. For this ring the mean 3D distance to the neighbouring vertices is 2.60 mm. The curvature is clipped between the 10 and 90th percentile values to remove outliers from the colormap. As the frontonasal suture is shaped as a saddle valley, the H values are negative in this region. On the right part it is illustrated that smoother curvature values can be obtained if the mesh is also smoothed after each subdivision iteration. The colormap for the Gaussian curvature K is shown in the bottom left figure for the same clipping interval. The 90th percentile value is close to zero, which means that almost the complete geometry is saddle-shaped. By selecting the triangles with negative H values (e.g. <-0.01) and splitting them

in connected regions, part of the frontonasal suture is displayed (see blue region in bottom right figure). The nasion point could then be determined as the most anterior point of this region (shown in red). While in this case the landmark seems to lie in the midsagittal plane, it is hard to obtain good results for each dataset using the same threshold values for the curvature. Also, the selection of the suture may span several triangles in the vertical direction and thus result in a landmark position above or below the desired one and outside the midsagittal plane. Finally, the suture might be less curved in some patients and the curvature values are very sensitive to noise in the 3D model.

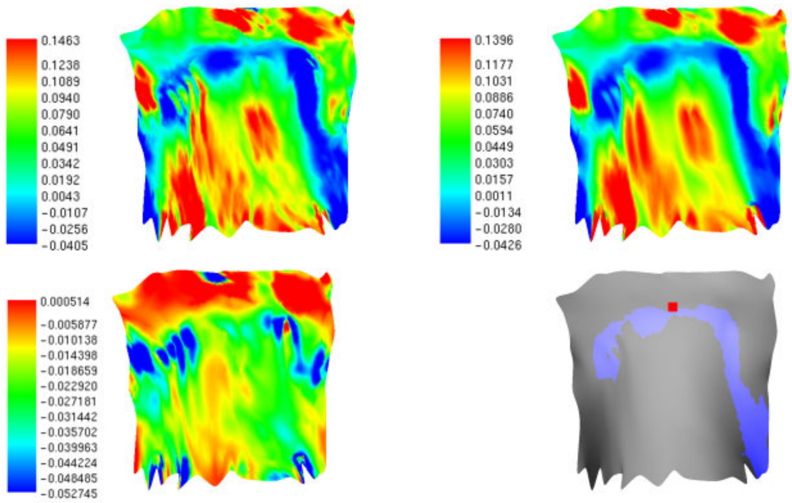

Figure 3.28: Curvature of the 3D surface mesh at the junction between the frontal and nasal bones: original mean curvature (tof left), smooth mean curvature (top right), Gaussian curvature (bottom left) and extracted frontonasal suture (bottom right).

Shape index (S) and curvedness (C)

These measures were introduced by Koenderink and van Doorn [18]. The curvedness ranges from 0 to infinity and specifies the amount of curvature. It is orientation, but not scale invariant. The shape index is a number in the range $[-1, +1]$ and is orientation as well as scale invariant:

$$S = \frac{2}{\pi} arctan \left(\frac{k_1 + k_2}{k_1 - k_2} \right) (k_1 \geq k_2) \tag{3.46}$$

$$C = \sqrt{\frac{k_1^2 + k_2^2}{2}} \tag{3.47}$$

As shown in Table 3.3, it covers all shapes except for the planar shape. However, this can be detected using the curvedness, which will be close to zero for planar regions. A graphical representation of the shapes as a function of S and C is given in Figure 3.29. While the HK method uses two thresholds to detect zero values, the SC method uses one threshold for the C values to classify planar regions [17].

Table 3.3: Shape classification based on shape index (S).

Shape	Index range
convex	$S \in [5/8, 1]$
ridge	$S \in [3/8, 5/8]$
hyperbolic	$S \in [-3/8, 3/8]$
valley	$S \in [-5/8, -3/8]$
concave	$S \in [-1, -5/8]$

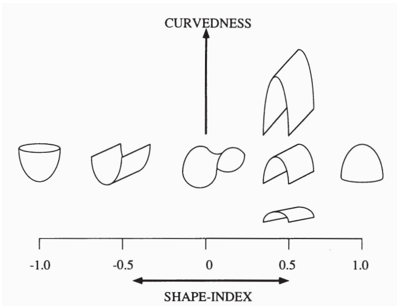

Figure 3.29: Graphical representation of shapes based on shape index (S) and curvedness (C): $S = -1$: concave umbilic, $S = -0.5$: valley, $S = 0$: minimal, $S = 0.5$: ridge, $S = 1$: convex umbilic [19].

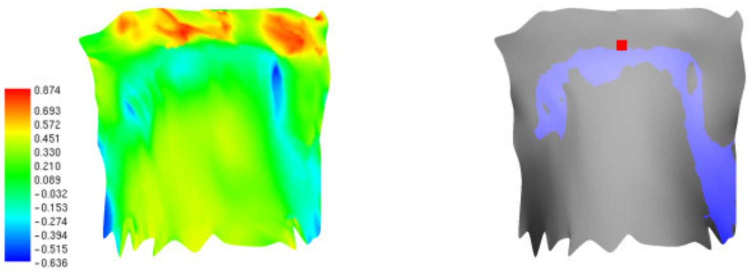

Figure 3.30: Curvature of the 3D surface mesh at the junction between the frontal and nasal bones: shape index (left) and extracted frontonasal suture (right).

The left part of Figure 3.30 shows the colormap for the shape index of the junction between the frontal and nasal bones. The saddle-valley-shaped region is found by selecting triangles with $S \in [-3/8, 0]$. The extracted frontonasal suture and nasion point are shown in the right figure. The distance from the previously extracted point using the mean curvature is 0.28 mm. The two methods thus seem to result in similar landmark positions.

3.4 Geometrical entity fitting

This section gives an overview of landmark extraction by fitting geometrical entities to a set of points. Several anatomical points and axes are defined using quadric surfaces, such as the centre of the best-fit sphere to the anatomy or the longitudinal axis of the best-fit cylinder. Compared to the extreme point and curvature method, which have been applied to locate landmarks as discrete points, this allows for a more global approach. The mesh data are used as input for the fitting algorithm to find a smooth surface that locally approximates the mesh. Besides quadric surfaces, other shapes can be used, such as lines and conic sections (e.g. a circle).

The fitting problem can be described as finding the set of parameters that minimizes some distance measure between the input points and the geometrical entity. One method is to measure the algebraic distance for each point, i.e. the deviation of the function value from the expected value. Because the algebraic distance is linear to the algebraic parameters, this approach has a low computing cost. However, its physical interpretation is usually not clear as it has no geometrical meaning. A more natural method is to use the orthogonal or geometric distance, which is defined as the shortest distance from the given point to the geometrical entity. Two types of parameters can be used to describe the geometry. The first one defines its size(s) (e.g. radius of a sphere) and the second one defines its position. The optimal parameters are found by minimizing the sum of squares of the distances using the nonlinear Levenberg-Marquardt least-squares optimisation [20, 21] routine of the SciPy library. Since the Levenberg-Marquardt algorithm only finds a local minimum, an initial guess should be provided for the parameter set.

3.4.1 Line fitting

A line can be described by a point q and vector m. The orthogonal distance of a point x from this line can then be calculated using Pythagoras' theorem:

$$d = \sqrt{|q - x|^2 - |\frac{(q - x) \cdot m}{|m|}|^2} \tag{3.48}$$

3.4.2 Quadric surface fitting

A quadric surface, or simply quadric, is described by a second degree equation in three variables:

$$l_1x^2 + l_2y^2 + l_3z^2 + l_4xy + l_5yz + l_6zx + l_7x + l_8y + l_9z + l_{10} = 0 \quad (3.49)$$

Typical examples of quadrics are spheres and cylinders. The equation can be written in matrix notation as

$$\begin{bmatrix} x & y & z \end{bmatrix} \begin{bmatrix} l_1 & \frac{l_4}{2} & \frac{l_6}{2} \\ \frac{l_4}{2} & l_2 & \frac{l_5}{2} \\ \frac{l_6}{2} & \frac{l_5}{2} & l_3 \end{bmatrix} \begin{bmatrix} x \\ y \\ z \end{bmatrix} + \begin{bmatrix} l_7 & l_8 & l_9 \end{bmatrix} \begin{bmatrix} x \\ y \\ z \end{bmatrix} + l_{10} = 0$$

$$xAx^T + bx^T + c = 0 \quad (3.50)$$

For a general quadric, calculating the orthogonal distance from a point x requires solving the following set of equations, which states that the line connecting the point x and its closest point x_c on the quadric Q should be orthogonal to Q in x_c:

$$\begin{cases} Q(x_c) = x_cAx_c^T + bx_c^T + c = 0 \\ x - x_c = t\nabla Q(x_c) = t(2x_cA + b) \end{cases} \quad (3.51)$$

The closest point x_c can then be eliminated:

$$x_c = (x - tb)(I + 2tA)^{-1} \quad (3.52)$$

$$(x - tb)(I + 2tA)^{-1}A(I + 2tA)^{-1}(x - tb)^T + \\ b(I + 2tA)^{-1}(x - tb)^T + c = 0 \quad (3.53)$$

If we use the eigendecomposition $A = R\Lambda R^T$ of A, where R is an orthonormal matrix (since A is real and symmetric) whose columns are the eigenvectors of A and Λ is a diagonal matrix whose entries are the eigenvalues, the above formulas can be written as

$$x_c = (x - tb)R(I + 2t\Lambda)^{-1}R^T \quad (3.54)$$

$$(x - tb)R(I + 2t\Lambda)^{-1}\Lambda(I + 2t\Lambda)^{-1}R^T(x - tb)^T + \\ bR(I + 2t\Lambda)^{-1}R^T(x - tb)^T + c = 0 \quad (3.55)$$

As the inverse matrix $(I + 2t\Lambda)^{-1}$ has three diagonal values $1/(1 + 2t\lambda_i)$, it can be seen that by multiplication with $(1 + 2t\lambda_1)^2(1 + 2t\lambda_2)^2(1 + 2t\lambda_3)^2$, a polynomial equation of at most sixth degree is obtained [3]. Quadric surface fitting using the exact orthogonal distances thus requires to find the roots of a (at most) sixth degree polynomial for every point in each iteration of the minimization algorithm. This computationally expensive method is avoided by calculating approximate geometrical distances for each point x. These are found by intersecting the quadric with the normal vector n of the surface mesh at x. This problem is described by the following equations

$$\begin{cases} Q(x_c) = x_c A x_c^T + b x_c^T + c = 0 \\ x - x_c = tn \end{cases} \tag{3.56}$$

The parameter t is easily solved from the second degree polynomial

$$(x - tn)A(x - tn)^T + b(x - tn)^T + c = 0 \tag{3.57}$$

and the smallest distance is retained. When no intersection with the mesh normal is found, the tetrahedron height vector is used. This method was proposed by Sappa and Rouhani [22] and is illustrated in Figure 3.31. If r, s and t are the intersection points along three orthogonal directions, creating a triangular planar patch, the quadric normal vector is approximated by the normal to this planar patch, also called the tetrahedron height vector. When intersections with some of the directions cannot be found, this method results in a 2D case (triangle height vector), 1D case or outlier.

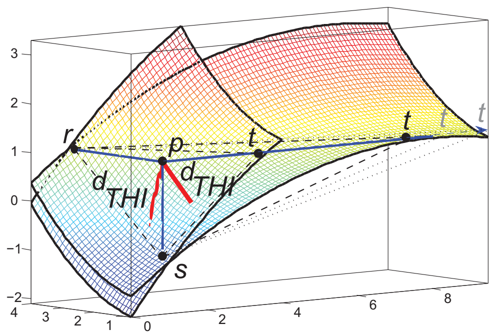

Figure 3.31: Estimation of the quadric surface normal using the tetrahedron height vector (red) for two surfaces: the vector is perpendicular to the plane formed by the intersection points r, s and t along three orthogonal axes [22].

An example of the quadric surface fitting method is given in Figure 3.32. The face centroids and normal vectors of the femoral head, shown in the left panel, are used as input to find the best-fit sphere to the anatomy. The result of the fitting algorithm is shown on the right. As the 50th and 95th percentiles of the distance values are 0.26 and 1.03 mm, the femoral head is well-approximated by the sphere. The centre of the sphere corresponds to the femoral hip centre, shown in red. A second example is shown in Figure 3.33 for the mastoid process of the skull. This structure is approximated with an elliptic paraboloid and the mastoid point is extracted as the centre of the quadric surface. The 50th and 95th percentile values of the distance for this case are 0.11 and 0.35 mm.

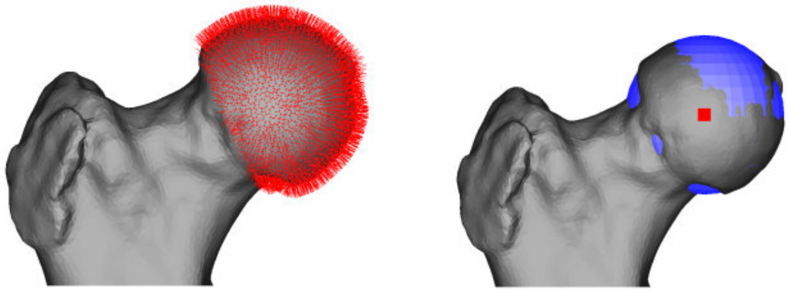

Figure 3.32: Example of quadric surface fitting: face centroids and normal vectors on the femoral head (left) and sphere fitted to the data (right).

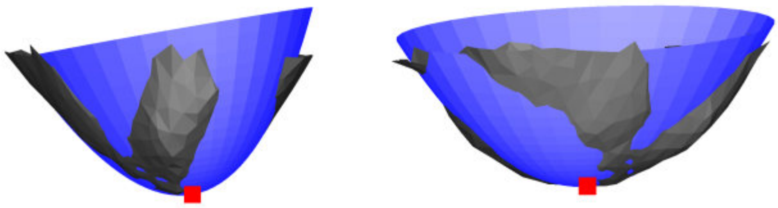

Figure 3.33: Example of quadric surface fitting: elliptic paraboloid fitted to the mastoid process: front view (left) and right view (right).

3.4.3 Error norm

As stated above, the fitting problem is solved by minimizing the sum of squares of the distances of the points to the geometrical entity. This method uses a quadratic error norm, as shown in Figure 3.34 (left). As the error gets large for points lying far from the optimal geometry, a single outlier in the point set may bias the solution. A Gaussian error norm [23] was therefore added, which is more robust to the presence of outliers by limiting the influence of the large errors on the minimization. The Gaussian error norm is given by the following equation and is shown in Figure 3.34 (right):

$$f(x) = 1 - e^{\frac{-x^2}{2\sigma^2}} \tag{3.58}$$

The scale parameter controls how quickly points are treated as outliers. It can be seen that the error asymptotically approaches 1 for values above 3σ.

The effect of the Gaussian error norm is illustrated using the example of the femoral head. Figure 3.35 shows a new set of input points, with outliers that do not lie on the femoral head. The results for the quadratic (left) versus Gaussian (right) error norm with $\sigma = 1$ demonstrate that using the first method the sphere is pushed towards the outlier points, while using the second method the influence of the outliers is limited and a much better fit is obtained.

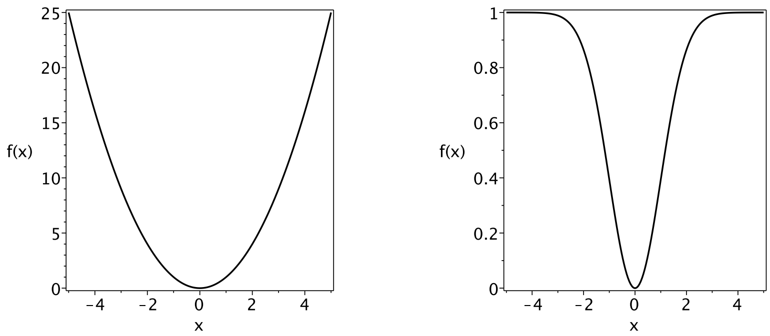

Figure 3.34: Graphs of the error function applied on the fitting distance: quadratic error norm (left) and Gaussian error norm for $\sigma = 1$ (right).

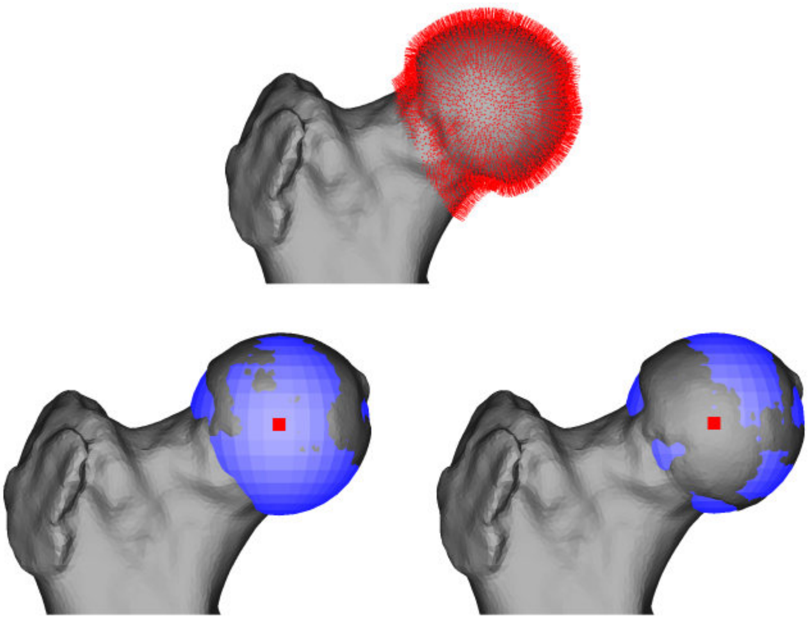

Figure 3.35: Effect of the error norm when outliers are present (top): quadratic error norm (bottom left) and Gaussian error norm (bottom right).

3.5 Cross-sectional area

The cross-sectional area of the mesh could be measured to determine the isthmus or narrowest part of a bony canal. Optimisation tools can be used to vary the position and orientation of a slicing plane that results in the smallest area. Analogously, the largest cross-section in a certain anatomical region could be determined. The slicing of the 3D mesh with a plane results in a 3D polygon. The area can then be computed using the following formula:

$$A = N \cdot \sum_{i=0}^{n-1} \frac{P_i \times P_{i+1}}{2} \tag{3.59}$$

where P_i are the vertices and N is the normal vector of the polygon. The optimal slicing plane is found using the Nelder-Mead Simplex algorithm of the SciPy library.

Figure 3.36 shows the smallest cross-section in the neck of the femur. The red line is the normal vector to the slicing plane, positioned at the centre of the cross-section, and may represent the femoral neck axis.

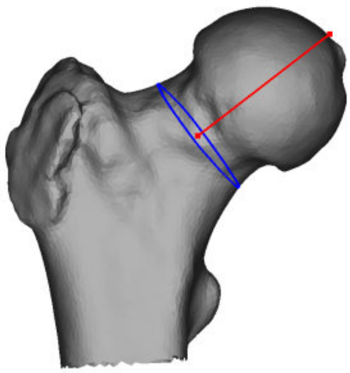

Figure 3.36: Smallest cross-section in the femoral neck region (blue) and normal vector of the slicing plane (red).

3.6 Rotational inertia

Rotational inertia or moment of inertia (MOI) of an object around a given axis is a measure of its resistance to changes in angular motion around that axis. It is the rotational analogy of mass, which describes the resistance to changes in linear motion. The MOI of a rigid body of n point masses around an axis through its centre of gravity can be calculated as the sum of the MOI's of each point mass:

$$I = \sum_{i=1}^{n} m_i r_i^2 \tag{3.60}$$

where m_i is the mass of the point and r_i is its orthogonal distance to the rotation axis. For a continuous rigid body, this is replaced by an integral expression. From the above equation it can be seen that the MOI depends on the distribution of mass and geometry (shape) of the object. If we assume that the mass is uniformly distributed, the MOI of the surface contour could be used as a measure of how much the geometry is spread around that axis. Any asymmetrical rigid body has two perpendicular axes of rotation around which the MOI is largest and smallest and which, together with their perpendicular vector, are called principal axes of inertia. In addition, any symmetry axis is a principal axis of inertia. The inertial properties of the surface mesh could thus be used to determine the axes around which the geometry is most or least spread and to find symmetry axes of the object. To account for non-uniform face sizes, the surface contour is discretised as a collection of point masses, where the points and masses are defined by the centroids and areas of the mesh faces.

The principal axes can be calculated from the MOI tensor I, which describes the relationship between the angular momentum vector L and the angular velocity vector ω of a rigid body rotating around some fixed axis:

$$L = I\omega \tag{3.61}$$

$$I = \begin{bmatrix} I_{xx} & I_{xy} & I_{xz} \\ I_{yx} & I_{yy} & I_{yz} \\ I_{zx} & I_{zy} & I_{zz} \end{bmatrix} \tag{3.62}$$

where I_{jk} is the MOI around the k-axis (j-axis) when the object is rotated around the j-axis (k-axis), e.g.:

$$\begin{aligned} I_{xx} &= \sum_{i=1}^{n} m_i(y_i^2 + z_i^2) \\ I_{xy} &= \sum_{i=1}^{n} m_i(-x_i y_i) \end{aligned} \tag{3.63}$$

and the scalar MOI I_ω around a given axis ω can be calculated from the tensor I as

$$I_\omega = \omega^T I \omega \tag{3.64}$$

Since I is real and symmetric, it has three orthonormal eigenvectors, which form a Cartesian coordinate system. These eigenvectors are the principal axes of inertia. From the definition of an eigenvector, it can be seen that if the axis of rotation is a principal axis, the angular momentum and angular velocity vectors are parallel:

$$L = I\omega = \lambda\omega \tag{3.65}$$

where λ is the corresponding eigenvalue, which is called a principal MOI.

In addition, the geometric centre of the surface contour can be found using the definition of the centre of gravity on the triangles' centroids X_i and areas m_i:

$$X = \frac{\sum_{i=1}^{n} m_i X_i}{\sum_{i=1}^{n} m_i} \tag{3.66}$$

Figure 3.37 shows the calculation of the geometric centre and principal axes of inertia of a femur model. The red and blue lines are the axes around which the moment of inertia is maximal and minimal. It can be seen that the mesh is least spread along the red axis and most spread along the blue axis. Also, the principal axes of the femur model seem to be a good first estimate for the anatomical directions. If the bone model would be oriented in a random way, this is a good start point for determining certain anatomical regions and setting up a standardised coordinate system.

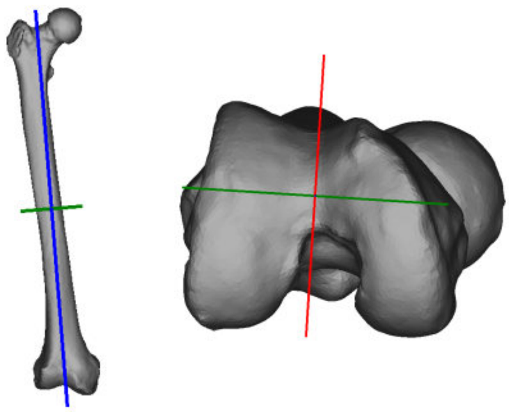

Figure 3.37: Principal axes of inertia of a femur model (front and bottom view): the axes can be used as a first estimate for the anatomical directions.

3.7 2D projection contour

While our main goal is to extract 3D landmarks from the surface mesh, a method to project the mesh on an arbitrary plane and compute its outer contour allows to extract 2D characteristics of the superimposed anatomy. This might be useful to compare some 3D measurements to 2D measurements, as currently obtained using radiographic images or CT slices. An approach proposed by Qin et al. [24] to find the 2D contour of a closed surface mesh was implemented and is illustrated in Figure 3.38. First, the possibly visible triangles are detected based on the angle of their normal vector with the projection axis. If this angle is greater than 90°, the normal points away from the projection axis and the triangle will be covered since the surface is closed. The edges possibly belonging to the 2D outer contour are found as the boundary edges between visible and invisible triangles. These edges form a set of closed polygons, which are then projected onto the given plane (see top left part of Figure 3.38). Each polygon surrounds a set of triangles, which may lie completely or partially in front of or behind another set of triangles. The next step is thus to determine which polygons or polyline pieces surround the front structures and to join them together to one outer contour. According to Qin et al. the contour is found by first deleting the inner polygons (lying completely inside another polygon) (bottom left) and then inserting vertices at the intersections of two polygons and removing the pieces that are inside the other polygon (bottom right). However, an extra step was added to our algorithm to account for self-intersecting polygons, which are first split into non-intersecting polygons (top right).

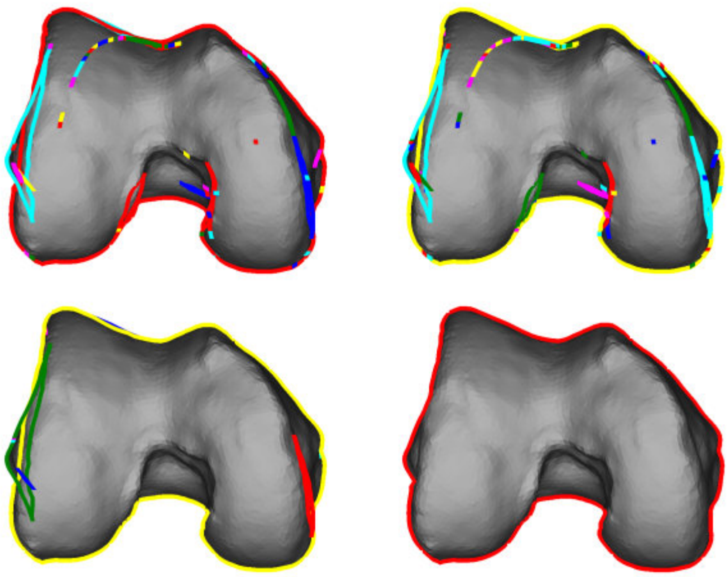

Figure 3.38: Example of 2D projection contour calculation: boundary between visible and invisible triangles (top left), self-intersecting polylines are split (top right), inner polylines are removed (bottom left), remaining polylines are intersected and outer parts are joined (bottom right).

3.8 Conclusions

Various mesh operations to process the original 3D model were presented in this chapter. The simplification method proposed by Lindstrom & Turk allows to reduce the model size and thus create meshes that require a smaller processing time. Using Taubin's $\lambda|\mu$ algorithm, the mesh vertices, and thus also the normal vectors, are smoothed, thereby removing noise from the model. The subdivision technique of Dyn et al. and Zorin et al. allows to interpolate between the mesh vertices by smoothly refining the triangular faces. Also, by implementing an algorithm to measure the distance between two triangulated surfaces it was shown that the mesh operations can be performed without introducing large geometric errors.

Different methods to automatically identify landmark features were implemented. The local extreme point approach is relatively straightforward, but of great interest as many landmarks have been defined as the extreme point of a certain anatomical structure in literature. Convex-, concave- as well as saddle-shaped structures can be processed using this method and by applying the subdivision algorithm the number of candidate points is increased to allow for more precise results. Two curvature algorithms to process 3D curves and surfaces were tested. The Gaussian smoothing method seems to be very useful to obtain a smooth curvature colormap over a curve. Points of extreme curvature can then be detected by searching for local minima or maxima. The 3D surfaces are more difficult to deal with. While several orientation (and scale) invariant measures can be used to select a region corresponding to a particular shape, it is hard to obtain good results for each dataset using the same threshold values for the curvature. The result might also be greatly affected by the mesh quality and morphology of the bone. It could be interesting to apply a 2D Gaussian smoothing filter to the mesh vertices to further reduce the influence of noise and small scale features. Nevertheless, it might not be obvious to extract a single, stable point from the extracted landmark region. The semi-global geometry fitting approach is more robust to noise compared to the local techniques as it approximates an anatomical structure with a predefined geometrical shape. In addition, the influence of outliers on the solution can be reduced using the Gaussian error norm. Furthermore, the smallest or largest cross-section of the mesh can be computed by searching for an optimal slicing plane. This method could for example be combined with circle fitting to find the smallest circular profile. The rotational inertia method allows to obtain the principal directions of the surface mesh. It gives an idea of how much the geometry is spread in a certain direction and can be used to extract initial estimates for relevant anatomical axes. Finally, the 2D projection algorithm can be applied to create a 2D contour from the 3D surface mesh. Using this method, some of the traditional 2D measurements can be determined in any plane.

As shown in the previous chapters, many different types of landmark definitions have been presented in literature. It is thus of great importance that various landmark extraction techniques are available and that the best possible method is chosen for each landmark. The methods presented in this chapter can be applied for different types of landmark features and bones. In the following chapters, they will be employed to analyse the skull and femur.

References

[1] Cignoni P, Rocchini C, Scopigno R. Metro: measuring error on simplified surfaces. Computer Graphics Forum, 17(2):167-174, 1998.

[2] Aspert N, Santa-Cruz D, Ebrahimi T. MESH: measuring errors between surfaces using the Hausdorff distance. Proceedings of the IEEE International Conference in Multimedia and Expo (ICME), Lausanne, Switzerland, 1:705-708, 2002.

[3] Schneider PJ, Eberly DH. Geometric tools for computer graphics. The Morgan Kaufmann Series in Computer Graphics and Geometric Modeling, Elsevier Inc, 2003.

[4] Lindstrom P, Turk G. Fast and memory efficient polygonal simplification. Proceedings of IEEE Visualization, pp. 279-286, 1998.

[5] Lindstrom P, Turk G. Evaluation of memoryless simplification. IEEE Transactions on Visualization and Computer Graphics, 5(2):98-115, 1999.

[6] Taubin G. A signal processing approach to fair surface design. Proceedings of the 22nd Annual Conference on Computer Graphics (SIGGRAPH), Los Angeles, California, USA, pp. 351-358, 1995.

[7] Taubin G. Geometric signal processing on polygonal meshes. Eurographics State of the art report, 2000.

[8] Jain AK. Fundamentals of digital image processing. Prentice Hall, 1989.

[9] Levy B, Zhang HR. Spectral mesh processing. ACM SIGGRAPH ASIA Course Notes, 2009.

[10] Dyn N, Levin D, Gregory JA. A butterfly subdivision scheme for surface interpolation with tension control. ACM Transactions on Graphics, 9(2):160-169, 1990.

[11] Zorin D, Schröder P. Subdivision for modeling and animation. Course notes of the 27th Annual Conference on Computer Graphics (SIGGRAPH), New Orleans, Louisiana, USA, 2000.

[12] Dyn N, Hed S, Levin D. Subdivision schemes for surface interpolation. Workshop on Computational Geometry, World Scientific Publications, pp. 97-118, 1993.

[13] Zorin D, Schröder P, Sweldens W. Interpolating subdivision for meshes with arbitrary topology. Proceedings of the 23rd Annual Conference on Computer Graphics (SIGGRAPH), New Orleans, LA, USA, pp. 189-192, 1996.

[14] Zorin D. Subdivision and multiresolution surface representations. PhD thesis, California Institute of Technology, Pasadena, California, USA, 1997.

[15] Zorin D, Subdivion on arbitrary meshes: algorithms and theory. IMS Lecture notes series, Mathematics and Computation in Imaging Science and Information Processing, 11:1-46, 2007.

[16] Dong CS, Wang GZ. Curvatures estimation on triangular mesh, Journal of Zhejiang University SCIENCE 6A Suppl.I: 128-136, 2005.

[17] Akagunduz E. 3D object recognition using scale space of curvatures. PhD thesis, Middle East technical university, 2011.

[18] Koenderink JJ, Doorn AJ van. Surface shape and curvature scales. Image Vision Comput, 10(8):557-565, 1992.

[19] van Damme WJM, Oosterhoff FH, van de Grind WH. Discrimination of 3D shape and 3D curvature from motion in active vision. Percept Psychophys, 55(3):340-349, 1994.

[20] Levenberg K. A method for the solution of certain non-linear problems in least squares. Quart Appl Math, 2(2):164-168, 1944.

[21] Marquardt W. An algorithm for least-squares estimation of nonlinear parameters. SIAM J Appl Math, 11(2):431-441, 1963.

[22] Sappa A, Rouhani M. Efficient distance estimation for fitting implicit quadric surfaces. IEEE Int Conf on Image Processing, Cairo, Egypt, pp. 3521-3524, 2009.

[23] van den Boomgaard R, van de Weijer J. Least squares and robust estimation of local image structure. IJCV, 64(2/3):143-155, 2005.

[24] Qin Z, Jia J, Li T, Lu J. Extracting 2D projection contour from 3D model using ring-relationship-based method. Inform Technol J, 6(6):914-918, 2007.

4

3D analysis of the skull

In this chapter, two studies about landmark localisation on the skull are presented. First, a method for semi-automatic localisation of landmarks on the virtual skull is proposed[1]. The new approach is evaluated by assessing the intra- and interobserver variability for measurements performed on one image of each skull. The second study presents the extraction of a larger number of landmarks and evaluates the method by determining the intraobserver variability for measurements performed on multiple images of the same skull[2].

[1]This study was published: Van Cauter S, Okkerse W, Brijs G, De Beule M, Braem M, Verhegghe B. A new method for improved standardisation in three-dimensional computed tomography cephalometry. Computer Methods in Biomechanics and Biomedical Engineering, 13(1): 59-69, 2010.

[2]Parts of this study were published: Van Cauter S, Okkerse W, Brijs G, De Beule M, Verhegghe B, Braem M. Reproducibility of landmark identification on different CT images of the head in three-dimensional cephalometry. Proceedings of the 9th international symposium on Computer Methods in Biomechanics and Biomedical Engineering, Valencia, 2010.

4.1 Semi-automatic approach for landmark localisation - intra- and interobserver reproducibility

4.1.1 Introduction

Cephalometry is the scientific study of the measurement of the head in relation to specific reference points. Based on these points, which are called anatomical landmarks, various distances, angles, lines and planes are traced and calculated. Since its introduction by Broadbent [1] and Hofrath [2] in 1931, cephalometry is a widely used measurement tool for diagnosis, treatment planning and outcome evaluation of dentofacial disharmonies in orthodontics and craniofacial surgery.

Traditionally, the landmarks are identified on tracings of 2D cephalometric radiographs. However, conventional radiographs are characterised by overlap effects due to superimposition of anatomical structures and by magnification and distortion errors depending on the distances between the X-ray source, the object and the film [3–5]. Moreover, it has been found that tracing variance is an important source of error [6–8]. Another disadvantage is that facial asymmetry in the frontal plane induces error in the evaluation of the lateral cephalogram as bilateral structures do not align or superimpose [9]. Because of these limitations, three-dimensional (3D) analyses using multiplanar radiography have been proposed [10, 11], which show better accuracy and reproducibility when compared to 2D cephalometry [12]. In this case the landmarks should be visible on images obtained from two or more different points of view and the difference in magnification of the various anatomical structures should be corrected.

Three-dimensional computed tomography (3D CT) cephalometry has gained popularity over the last two decades due to the progress in CT imaging and the increased interest for computer-assisted planning of surgery. It has been shown that CT data can provide additional useful information to standard radiography for patient management and that in most of the cases 2D CT scan slices are not as useful without 3D rendered images [13, 14]. Furthermore, distance measurements are more exact using reformatted 3D images than using original 2D slice data [15, 16]. With the aid of 3D CT, the model can be viewed from any angle, the inner structures can be visualised and various organ parts (e.g. bone and soft tissue) can be observed independently [17]. In addition, 3D CT cephalometry allows evaluation of complex abnormal anatomies such as asymmetrical cases since 3D images and measurements are assessed [18, 19]. Finally, compared to 2D radiographic cephalometry intra- and interobserver reproducibility are significantly superior following the 3D CT method [20].

The anatomical landmarks or cephalometric points are commonly determined by manual point-picking on these surface renderings. Because of the variability in head position during scanning, orientation of the image is required. This is done either by manual (subjective) alignment of anatomical structures or by automatic set-up of a reference system based on previously determined landmarks. Consequently, reproducibility depends mainly on the judgement and experience of the examiner.

Cephalometric analysis could be used to evaluate the outcome of orthognathic surgery, in which the position of one or more jawbones is corrected. Reproducibility of the landmark coordinates should be high to allow for correct comparison of data such as pre- and postoperative images. Otherwise, the variability in measurement values could lead to misinterpretation of the data. In this paper, new methods for landmark identification and image orientation are investigated, which aim to improve reproducibility of cephalometric measurements. The approach which is used is twofold: advance standardisation in cephalometry and limit the input of the examiner.

4.1.2 Materials and methods

The new methods for improved standardisation in 3D CT cephalometry were developed using pyFormex (http://www.pyformex.org), which is an open-source program under development at IBiTech. This software is intended for generating, manipulating and operating on large geometrical models of 3D structures. A module for cephalometric analysis was created combining general features of pyFormex and newly implemented tools for landmark identification and image orientation. All operations are performed on a triangular model of the skull.

4.1.2.1 Landmark identification

The cephalometric points determined in this study are summarised in Table 4.1. Two types of points can be distinguished: biological (type B) and constructed (type C) landmarks. Biological landmarks are situated on a certain anatomical structure of the body. In this work they are identified by calculating the extreme point in a specified direction of the structure. This is illustrated in Figure 4.1 for the point orbitale right (OrR), which is defined in literature as the most inferior point of the right infraorbital rim. The following procedure is carried out to determine OrR:

- *The examiner selects a surface region on the triangular model of the skull.* For this operation a picking procedure was developed which allows the user to (de)select triangles, remove unconnected parts from the selection and refine the selection in a new picking operation. For the landmark OrR the surface region is the lower part of the right orbit (see Figure 4.1 (a)).

- *The quality of the surface region is improved.* As shown in Figure 4.1 (b), the triangular surface model is quite coarse. Therefore, some quality improving techniques are performed.

Table 4.1: Landmarks used in this study. Biological landmarks (type B) are defined by a surface and/or line region and direction. Constructed landmarks (type C) are defined by their construction method. The landmarks are visualised in Figure 4.3.

Landmark	Type	Surface region	Line region	Direction/Construction
Clinoid anterior left (CAL)	B	Left posterior angle of lesser wing		Posterior
Clinoid anterior right (CAR)	B	Right posterior angle of lesser wing		Posterior
Clinoid posterior left (CPL)	B	Left anterior angle of dorsum sellae		Anterior
Clinoid posterior right (CPR)	B	Right anterior angle of dorsum sellae		Anterior
Nasion (N)	B	Part of nasal and frontal bone	Deepest points of sagittal profiles	Anterior
Orbitale left (OrL)	B	Lower part of left orbit	Highest points of sagittal profiles	Inferior
Orbitale right (OrR)	B	Lower part of right orbit	Highest points of sagittal profiles	Inferior
Sella (S)	C			Mean of SS and SI
Sella inferior (SI)	B	Hypophyseal fossa	Sagittal profile through SS	Inferior
Sella superior (SS)	C			Mean of clinoid points

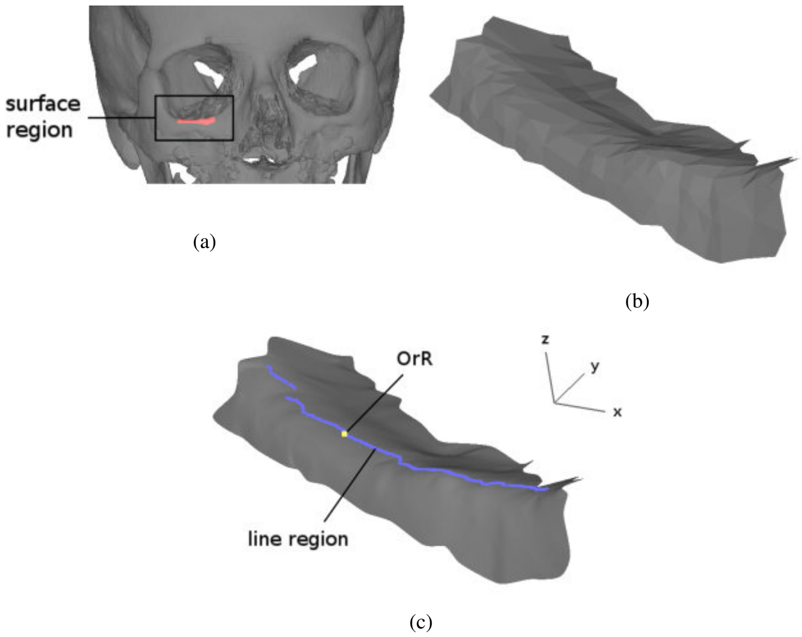

Figure 4.1: Landmark determination illustrated for the point OrR. (a) The user picks a surface region on the triangular model. (b) The original surface region is quite coarse. (c) The surface region is smoothed and refined, a line region is calculated and the landmark is determined.

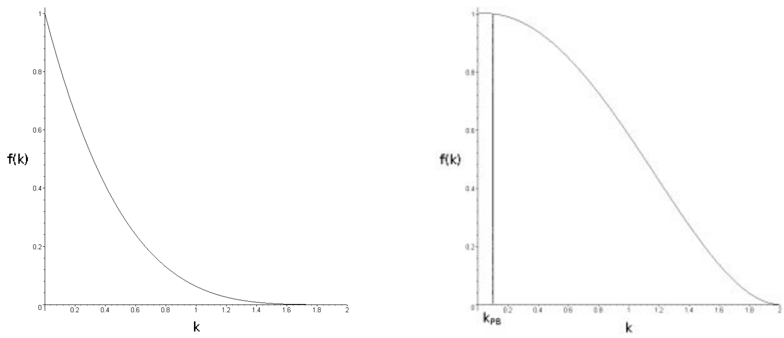

Figure 4.2: Different smoothing filters: k are the frequencies of the surface signal ($0 \leq k \leq 2$) and f(k) is the transfer function of the filter. Low frequencies correspond to low curvatures, while high frequencies correspond to high curvatures.
Left: Laplace filter: $f(k) = (1 - \lambda k)^n$ ($\lambda = 0.5$, $n = 4$).
Right: low-pass filter: $f(k) = ((1 - \lambda k)(1 - \mu k))^{n/2}$ ($\lambda = 0.5$, $n = 4$, $k_{PB} = 0.1$).

– *The surface region is smoothed to remove noise and to obtain a more uniform curvature.* The vertices (corner points of the triangles) are submitted to a low-pass filter algorithm [21, 22], which is a combination of two Laplace filters. During Laplacian smoothing the vertex coordinates are recalculated according to Equation 4.1, in which p are the original coordinates, n is the valence (number of edges connected to p), q_i are the adjacent points (points that share an edge with p) and λ is a scale factor ($0 < \lambda < 1$):

$$p' = p + \frac{\lambda}{n} \sum_{i=0}^{n-1} (q_i - p) \tag{4.1}$$

However, the object tends to shrink drastically after applying the Laplace filter iteratively a large number of times. In Figure 4.2 (left), the Laplace filter for a scale factor λ of 0.5 and four iterations is shown. In this figure, k are the frequencies of the surface signal ($0 \leq k \leq 2$) and f(k) is the transfer function of the filter. Low frequencies correspond to low curvatures, while high frequencies correspond to high curvatures. The Laplace filter produces shrinkage because all the frequency components, other than the zero component are attenuated ($|f(k)| < 1$ for $0 < k \leq 2$).

To prevent shrinkage, the low-pass filter alternates between two steps of Laplacian smoothing: a shrinking step with positive scale factor λ and an unshrinking step with negative scale factor μ, greater than λ in absolute value ($\mu < -\lambda < 0$). As shown in Figure 4.2 (right), this filter preserves low frequency components ($0 \leq k \leq k_{PB}$) and attenuates higher frequency components ($k_{PB} < k \leq 2$). The boundary is the pass-band frequency k_{PB} ($f(k_{PB}) = 1$). If the scale factor λ and the pass-band frequency k_{PB} are known, μ can be calculated from Equation 4.2:

$$\frac{1}{\lambda} + \frac{1}{\mu} = k_{PB} \tag{4.2}$$

As suggested by Taubin, a pass-band frequency of 0.1 was chosen. The surface region is smoothed using four iterations of a low-pass filter with a scale factor λ of 0.5. For this combination of parameters, the transfer function f(k) decreases to zero, as k increases from $k = k_{PB}$ to $k = 2$ (see Figure 4.2 (right)).

The surface regions of one skull model before and after low-pass filtering were compared to evaluate the error induced by smoothing. Since the regions are not closed, the volume change could not be used as an appropriate measure for shrinkage and the change in surface area was used instead. The area change varied between -0.23% and -1.16% and is therefore negligible. As a comparison, the analogous Laplace filter would result in an area change between -0.82% and -13.46%.

– *The surface region is refined to allow for interpolation between the original vertices of the model.* For this step, a subdivision algorithm based on the modified butterfly scheme [23, 24] was implemented. This algorithm splits every triangle into four new triangles by inserting one vertex per edge. The new vertex is calculated as a weighted sum of vertices adjacent to the edge. The weights depend on the characteristics of the edge (boundary or interior edge, boundary or interior vertices, valence of the vertices) and in total seven types of rules can be distinguished. The modified butterfly scheme guarantees that the limit surface is C^1 continuous, i.e. has continuous tangent planes [25]. The surface region is refined using three iterations of the subdivision algorithm.

The model resulting from the smoothing and refinement operation is shown in Figure 4.1 (c).

- *A line region is calculated.* In this case, the line region approximates the infraorbital rim. It is defined as the highest points of sagittal (yz) profiles through the surface region (see Figure 4.1 (c)). The distance between these profiles is approximately 0.05 mm. Since not all landmark definitions include a line region, this step is optional.

- *The landmark coordinates are determined.* For the point OrR the lowest point of the line region is calculated (see Figure 4.1 (c)). For landmarks which do not have a line region, the extreme point of the surface region is calculated.

This approach restricts the input of the user to the selection of the surface region on the triangular model of the skull. All following steps are performed automatically.

Other biological landmarks used in this study are points orbitale left (OrL), nasion (N), clinoid (CAR, CAL, CPR, CPL) and sella inferior (SI). As shown in Table 4.1, these points are defined by the anatomical structure (surface and/or line region) on which they are situated and by the direction in which they are calculated as the extreme point. The position of all the semi-automatically extracted landmarks is depicted in Figure 4.3.

Constructed landmarks are defined using a combination of other landmarks. As an example, the construction of point sella (S) is explained. This landmark is traditionally defined as the centre of the sella turcica, which is a saddle-shaped concavity in the sphenoid bone (see Figure 4.3 (b) and (c)). It is computed by the following procedure:

- Four clinoid points are determined: two on the lesser wing and two on the dorsum sellae (see Table 4.1 and Figure 4.3 (b)).
- Landmark sella superior (SS) is calculated as the mean of the four clinoid points (see Figure 4.3 (c)).
- Landmark sella inferior (SI) is determined as the lowest point of the intersection of the hypophyseal fossa (seat of the sella turcica) with a sagittal plane through sella superior (see Figure 4.3 (b) and (c)).
- Landmark sella (S) is calculated as the mean of sella superior and sella inferior (see Figure 4.3 (c)).

Both constructed points used in this study, sella superior and sella, are again calculated automatically.

4.1.2.2 Image orientation

To orientate the model, a reference system based on four landmarks is set up: orbitale right (OrR), orbitale left (OrL), sella (S) and nasion (N). During image orientation four requisites are taken into account, which correspond to three rotations and one translation (see Table 4.2). The rotation in the frontal and transversal plane aims to obtain an orientation in which similar anatomical structures are positioned symmetrically relative to the midsagittal (yz) plane. This is the natural head position, which in addition will result in landmarks which are most clinically meaningful. For example, point nasion will be situated more in the middle of the nasal bone along the transversal (x) axis if the skull is positioned symmetrically. To obtain such an orientation, orbitale right and orbitale left are placed at the same height and sella and nasion are positioned in the same sagittal plane. Rotation in the sagittal plane puts the anterior cranial base (S-N line) 6° above the horizontal plane. This transformation is based on the two- to nine-degree average orientation of the S-N line from true horizontal [26]. Finally, sella is positioned at the origin. The reference system is visualised in Figure 4.4. Since all transformations

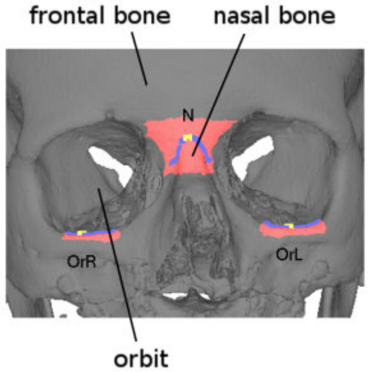

(a)

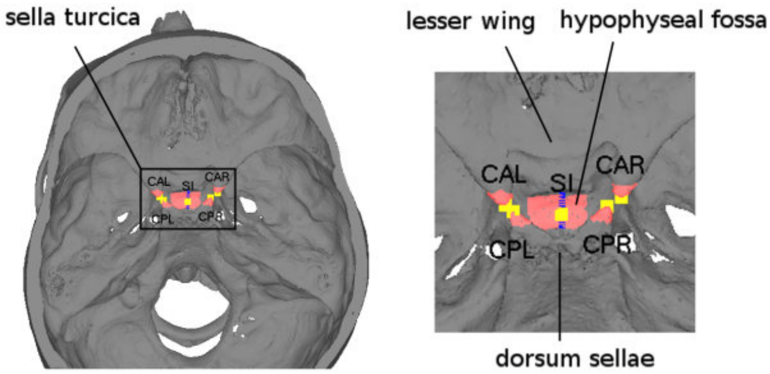

(b)

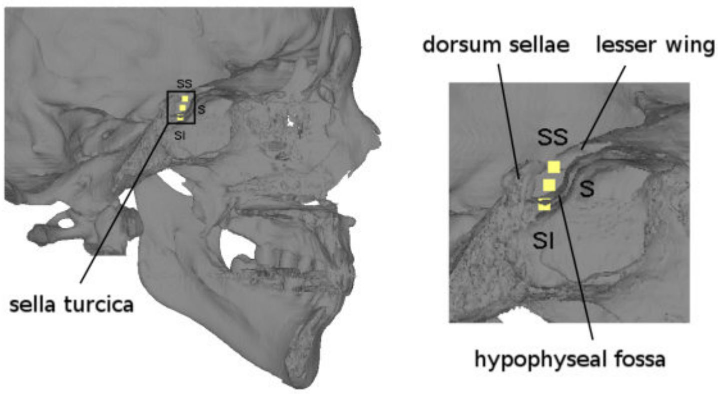

(c)

Figure 4.3: Landmarks used in this study. The surface regions (red), line regions (blue) and points (yellow) are visualised. (a) Anterior view: landmarks OrR, OrL and N. (b) Superior view: landmarks CAL, CAR, CPL, CPR and SI. (c) Paramedian sagittal view: landmarks SS, SI and S.

Table 4.2: Orientation requisites used to set up the reference system.

Transformation	Requisite
Rotation in the frontal plane	OrR and OrL at the same height
Rotation in the transversal plane	S-N line in a sagittal plane
Rotation in the sagittal plane	S-N line 6° above the horizontal plane
Translation	S at the origin

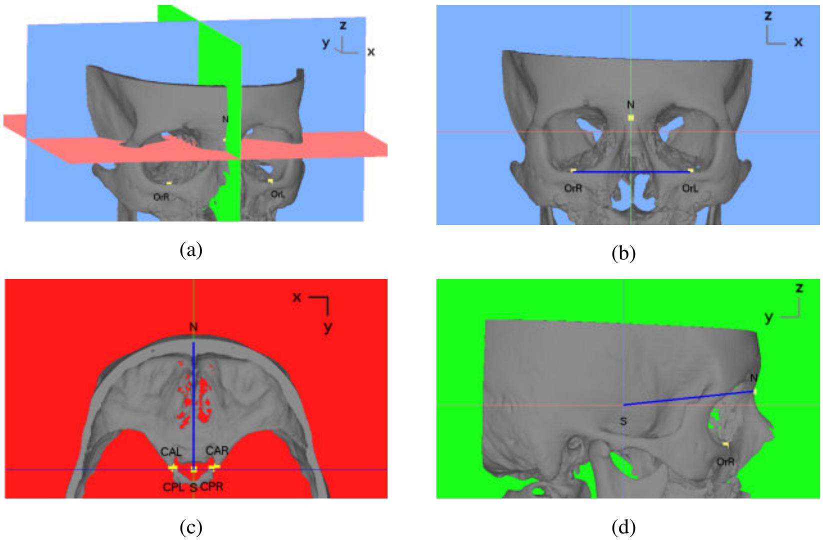

Figure 4.4: The reference system used to orientate the skull (x, transversal axis; y, sagittal axis; z, longitudinal axis). (a) 3D view. (b) Anterior view: OrR and OrL are at the same height. (c) Superior view: the S-N line is positioned in the midsagittal plane. (d) Lateral view: the S-N line is situated 6° above the horizontal plane.

are based on previously determined landmarks, the orientation procedure can be performed automatically.

Because after rotating the skull the extreme points may have changed, the line regions and landmark coordinates have to be recalculated. Since this may result in a different reference system, image orientation has to be repeated as well. Hence, an iterative procedure is used. During each iteration, the skull is re-orientated and the line regions and landmarks are recalculated. After each iteration, the four orientation requisites of Table 4.2 are evaluated. The orientation procedure stops when all requisites are fulfilled. In this case, the three rotation angles associated with these requisites have converged to zero. However, due to the character of the model, only a finite number of vertices can be taken into account. As a result, it is possible that the orientation procedure does not converge, i.e. that one or more rotation angles do not converge to zero. Instead, consecutive angles which have the same absolute value but different sign can be observed. Therefore, the procedure stops after equal rotation angles are detected in three iterations. To decrease the deviation from a converged referenced system, a last iteration is performed, in which the skull is rotated over angles that are half of the recurrent rotation angles in absolute value. In this case, a warning message is shown to the user and the final deviation (the deviation of the current reference system from the reference system set up by the final landmark coordinates) can be viewed.

4.1.2.3 Evaluation of the new methods

To study the performance of the new methods, three sets of CT scans were used. All images had an intra-slice resolution of 0.48 mm and inter-slice resolution of 0.6 mm. Segmentation and 3D reconstruction of the skull was done using Mimics® (Materialise NV, Leuven, Belgium). The predefined threshold interval for bone in CT images (226–3071 HU) was chosen to identify the skull and the optimal quality parameters were selected to calculate a triangular surface mesh. Then, the 3D surface model was loaded into pyFormex.

Using the cephalometry module, two examiners each performed five analyses for the three skull models, with a minimum time interval of two days. One examiner was a dentist who is experienced in using 3D cephalometry, while the other was an engineer who implemented the semi-automatic landmark identification tool. Based on these data, the orientation of the skull models and the reproducibility of the landmark coordinates were investigated. To evaluate the orientation method, a quantitative judgement of the symmetrical appearance of the models was made. Since all data were obtained from patients undergoing orthognathic surgery, the jaws are likely to have an asymmetrical position and thus they were removed from the skull model. Next, the model was split into two parts, separated by the midsagittal (yz) plane. The positive vertices were mirrored against the midsagittal plane and the minimum distance of each mirrored positive vertex from the negative vertices was calculated. Finally, the percentage of mirrored positive vertices lying within a certain distance from the negative vertices was determined. Intraobserver reproducibility was examined by means of the standard deviation of the five analyses of each user. Interobserver reproducibility was evaluated by calculating the difference between the mean values of the five analyses of each observer.

4.1.3 Results

4.1.3.1 Orientation

The orientation of the skull models after calculation of the reference system is shown in Figure 4.5. A symmetrical orientation relative to the midsagittal (yz) plane can be observed for the three models. The percentage of mirrored positive vertices lying within a certain distance from the negative vertices is shown in Figure 4.6. 50% of the mirrored positive vertices lies within 0.8 mm, 75 % within 1.3 mm and 90% within 2.2 mm of the negative vertices. The mean calculation time for the orientation procedure was approximately six minutes. Two calculations did not converge, but this did not result in a significant error since the maximum deviation of the final reference system from the reference system set up by the final landmark coordinates was -0.03°.

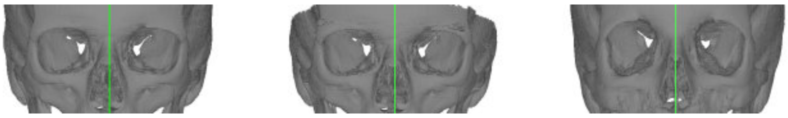

(a) (b) (c)

Figure 4.5: The skull models after the calculation of the reference system. A symmetrical orientation relative to the midsagittal (yz) plane is obtained. (a) model 1, (b) model 2 and (c) model 3.

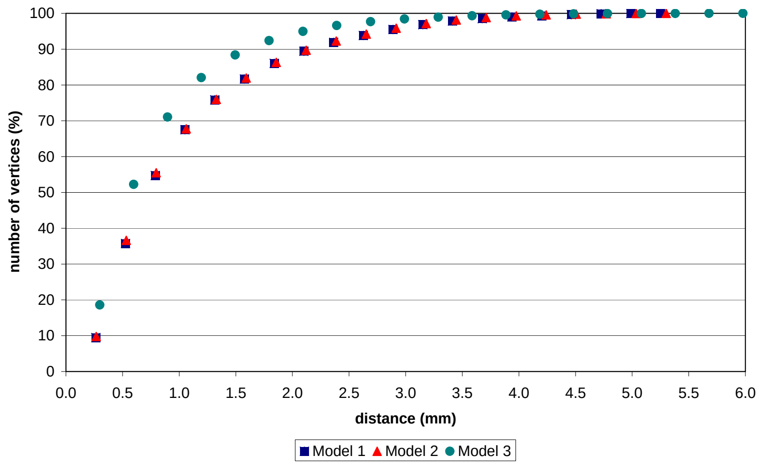

Figure 4.6: Quantitative evaluation of the symmetrical appearance of the models: the percentage of mirrored positive vertices lying within a certain distance from the negative vertices.

4.1.3.2 Intraobserver reproducibility

Intraobserver reproducibility is depicted in Figures 4.7 and 4.8. The standard deviations of the 10 landmarks along the transversal (x), sagittal (y) and longitudinal (z) axis before and after the orientation procedure were calculated.

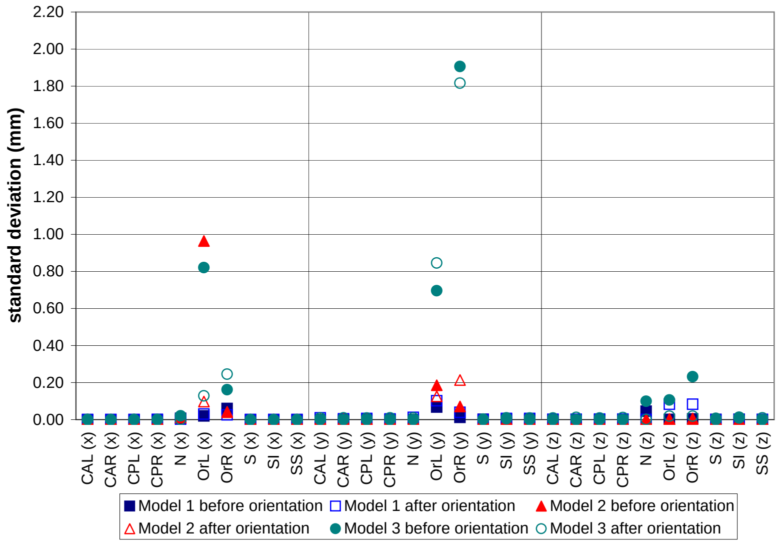

Figure 4.7: Intraobserver reproducibility for examiner 1: standard deviation of five analyses along the transversal (x), sagittal (y) and longitudinal (z) axis.

For the first examiner, all landmarks except OrL and OrR have standard deviations below 0.1 mm, which indicates high reproducibility. The higher values for the orbitale points can be explained as follows. In the second model the line region for OrL is rather horizontal in the neighbourhood of the lowest point before orientation. As a result, a higher standard deviation (0.96 mm) was obtained for the x-coordinate of the landmark. After orientation, however, all values are below 0.22 mm. The results for the third model show high variability for the points OrL and OrR, before as well as after calculation of the reference system. This is caused by the fact that the infraorbital rim can not be readily distinguished. If the surface region does not clearly go up and down in the sagittal (y) direction (see Figure 4.1 (c)), then the result for the line region, which was defined as the highest points of sagittal (yz) profiles through the surface region, will depend on the area to which the surface region extends in the sagittal direction. Consequently, high standard deviations occur in the sagittal direction for the points OrL and OrR (0.85 mm and 1.82 mm after orientation).

Similar results are obtained for the second examiner. In the first and second model eight of ten landmarks have standard deviations below 0.1 mm, while points OrL and OrR have standard deviations below 0.46 mm and 0.29 mm. The highest variability is again observed for the third model, in particular for points OrL and OrR (3.40 mm and 1.70 mm after orientation).

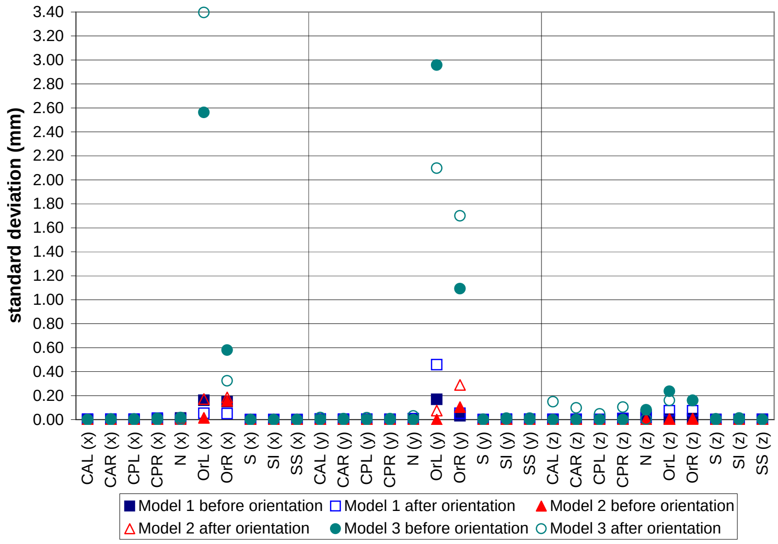

Figure 4.8: Intraobserver reproducibility for examiner 2: standard deviation of five analyses along the transversal (x), sagittal (y) and longitudinal (z) axis.

4.1.3.3 Interobserver reproducibility

Interobserver reproducibility is shown in Figure 4.9. The difference between the mean values of both examiners is below 0.1 mm for all landmarks except OrL and OrR in the three models. The highest values for OrL and OrR are 0.43 mm and 0.05 mm in the first model, 0.49 mm and 0.34 mm in the second model and 1.46 mm and 2.81 mm in the third model.

4.1.4 Discussion

Many studies regarding 3D CT cephalometry have been performed, presenting various methods for landmark identification, image orientation [17, 27–29] and cephalometric analysis [17, 30, 31] and showing the need for improved standardisation and for investigation of the accuracy and reproducibility of cephalometric measurements. Several studies about reproducibility of 3D CT cephalometry have been published. Some of them investigated correlation coefficients, while others calculated standard deviations. Intraobserver intraclass correlation coefficients between 0.970 and 0.998 for ten subjects and four landmarks [28] and between 0.941 and 0.993 for 23 subjects and 20 linear distances [32] have been reported. Intra- and interobserver intraclass correlation coefficients for 26 subjects and nine linear distances were obtained with 3D CT cephalometry and 2D radiographic cephalometry [20]. The 3D method proved to be significantly superior, showing

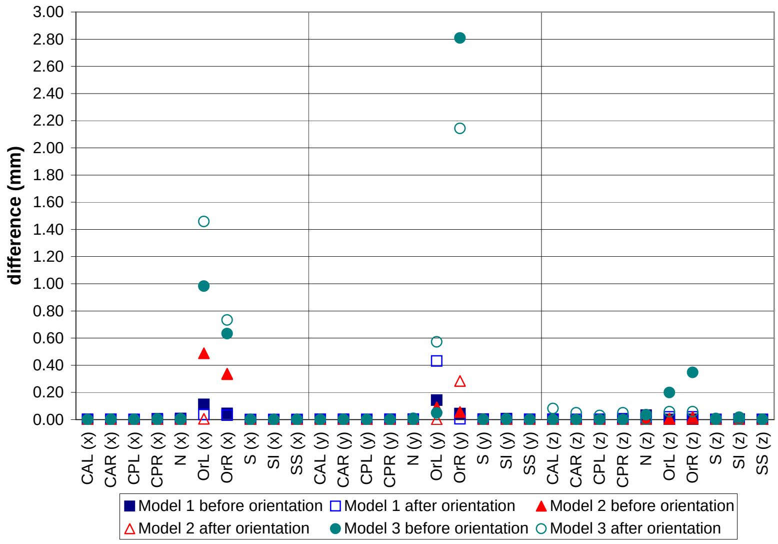

Figure 4.9: Interobserver reproducibility: difference between the mean values of both examiners along the transversal (x), sagittal (y) and longitudinal (z) axis.

intraobserver correlation coefficients between 0.972 and 0.998 and interobserver correlation coefficients between 0.936 and 0.997. Maximal intraobserver standard deviations of 0.86, 0.93 and 1.67 mm for the transversal, sagittal and longitudinal direction for one subject and 19 landmarks [17] have been reported. Mean intraobserver standard deviations were 0.39, 0.45 and 0.74 mm.

These studies rely on the examiner to manually point-pick the landmarks and/or orientate the skull. The method for landmark determination presented in this paper limits the input of the user to the selection of a surface region on the skull model. Since this operation is less user-dependent, higher reproducibility can be achieved. In this study, intraobserver standard deviations and interobserver differences lower than 0.1 mm were obtained for most landmarks. When compared to the intraobserver standard deviations reported by Park et al. [17], these results indicate that a significant improvement can be achieved with the new methods. Nevertheless, some landmarks perform poor if the feature that distinguishes them is not present in the geometry. This is for example the case for the orbitale points, if the infraorbital rim can not be approximated using the definition of the line region. When using the manual point-picking method however, the user has to deal with the absence of characteristic features on the surface rendering as well. Such landmarks require further investigation. An automated procedure is used to orientate the skull based on four landmarks. Taking into account the method used for landmark determination, an iterative procedure is required to compensate for variations due to rotating the skull. The results obtained in this study show that a symmetrical orientation is achieved with the presented reference system. The distance between the mirrored left part and the right part of the skull is less than 2.2 mm for 90% of the vertices. When evaluating the orientation of the skull models, it should be kept in mind that some skulls may have asymmetrical features, that no skull is completely symmetrical and that the reproducibility of the orientation should be the most determining factor for choosing the reference system.

Cephalometric measurements can be used to evaluate the outcome of a treatment if a correct interpretation of the data is possible. If the observed values of a clinical study are, however, smaller than the reported error, it cannot be concluded that the observed effect is due to therapy [8]. This study shows that the error in landmark determination on 3D surface models can be limited. Moreover, the set-up of a standardised reference system should contribute to the comparison of data, such as pre- and postoperative images from orthognathic patients.

Although interesting preliminary results were obtained in this study, some limitations remain. The number of patient data and landmarks used in this work was rather small. Reproducibility should be tested for a larger amount of data and other landmarks should be investigated. Because of the lower reproducibility of the orbitale points, other reference systems should be evaluated as well. The accuracy of the landmark coordinates was not studied. In future, landmark coordinates measured on 3D CT models could be compared to direct measurements on the dry skulls to study the accuracy of the new methods. The number of smoothing and subdivision steps applied on the surface regions was chosen arbitrarily. The influence of smoothing and subdivision on the accuracy of the landmark coordinates could be used to determine an optimal number of iterations. The main drawback of CT imaging is the increased radiation exposure compared to conventional radiography, but it is shown that with cone-beam CT the radiation dose can be significantly reduced [33]. Therefore, cone beam CT will probably enhance the use of 3D CT cephalometry in orthodontic and craniofacial applications.

4.1.5 Conclusions

The number of studies concerning 3D CT cephalometry show that this technique will become an important measurement tool in both orthodontics and craniofacial surgery. The methods proposed in this study, namely landmark calculation and image orientation, contribute to an improved standardisation in cephalometry. Because the region-picking operation is less user-dependent, high reproducibility can be achieved for most of the investigated landmarks. Along with the set-up of a standardised reference system, this approach could allow for improved comparison of patient data.

4.2 Semi-automatic approach for landmark localisation - precision for multiple CT images

4.2.1 Introduction

In the previous study, it was shown that the new method for 3D landmark localisation results in high precision for several landmarks when multiple analyses are performed on the same 3D model of the skull (intraobserver SD ≤ 0.15 mm and interobserver difference between the mean values of each operator ≤ 0.10 mm for eight out of ten landmarks). However, all the steps that are performed to generate the final model introduce some geometrical error: the anatomy is discretised in voxels, the bony structures are segmented, a 3D reconstruction is generated, the model size is reduced and the mesh is smoothed. Also, when the process is repeated using different parameters, another surface mesh is obtained. As mentioned in chapter 1, the landmark position may change if the anatomy is discretised in a different way and it is thus important to compare the results for different models of the same anatomy. In this study, the effect of using different smoothing parameters and multiple CT images of the same skull on the landmark positions is investigated.

4.2.2 Materials and methods

4.2.2.1 Skull models

Pre- and postoperative CT images of 12 patients that underwent jaw surgery were used to construct two triangulated meshes of each skull. All images had an intra-slice resolution of 0.48 mm and an inter-slice resolution of 0.60 mm. Segmentation and 3D reconstruction of the skull was done using Mimics® (Materialise NV, Leuven, Belgium), by applying the predefined threshold interval for bone (226-3071 HU) and the optimal 3D reconstruction quality parameters (contour interpolation, two iterations of Laplacian smoothing and three iterations of triangle reduction).

4.2.2.2 Landmark identification

The surface models were imported into pyFormex and for each model, 15 landmark regions, situated on the non-operated part of the skull, were identified. The analyses were performed once by one investigator: the engineer who implemented the semi-automatic landmark identification tool and who is experienced in using the software. Table 4.3 gives an overview of the 3D landmark definitions and Figure 4.10 shows the landmark positions. The methods described in the previous study were used to localise the points, but some improvements to the procedure were made:

- The direction for the extreme point extraction was modified for some of the anatomical structures. For example, the infraorbital rim was found to be slightly oriented in the anterior direction and therefore, an AP component was added for the localisation of this ridge.
- Sella was previously defined as a point lying inside the sella turcica and was obtained using two other landmarks, lying at the top and bottom of the sella turcica: sella superior and sella inferior. However, the hypophyseal fossa or floor of the sella turcica is a thin bony structure and can be hard to distinguish on the CT scans. As a result, especially using thresholding for the segmentation, holes might be present in the fossa of the 3D model. Therefore, it was chosen to use sella superior as the reference point of the sella turcica in this study.
- In the previous study, the ridge and valley regions were calculated as a discrete set of extreme points (e.g. the most superior points of the lower orbit region). As illustrated in chapter 3, however, a smooth spline can be created from the points. Using this new method, the landmark position is less affected by small changes in the orientation of the model.

Table 4.3: Landmark definitions. The landmarks are visualised in Figure 4.10.

Landmark	Definition
Basion (Ba)	Most anterior point of great foramen
Clinoid anterior left (CAL)	Most posterior point of left posterior angle of lesser wing
Clinoid anterior right (CAR)	Most posterior point of right posterior angle of lesser wing
Clinoid posterior left (CPL)	Most anterior point of left anterior angle of dorsum sellae
Clinoid posterior right (CPR)	Most anterior point of right anterior angle of dorsum sellae
Mastoid left (MaL)	Most inferior point of left mastoid process
Mastoid right (MaR)	Most inferior point of right mastoid process
Nasion (N)	Most anterior point of frontonasal suture
Orbitale left (OrL)	Most inferior point of left infraorbital rim
Orbitale right (OrR)	Most inferior point of right infraorbital rim
Porion left (PoL)	Most superior point of left external auditory meatus
Porion right (PoR)	Most superior point of right external auditory meatus
Sella superior (SS)	Mean position of CAL, CAR, CPL & CPR
Zygion lateral left (ZyL)	Most lateral point of left zygomatic arch
Zygion lateral right (ZyR)	Most lateral point of right zygomatic arch

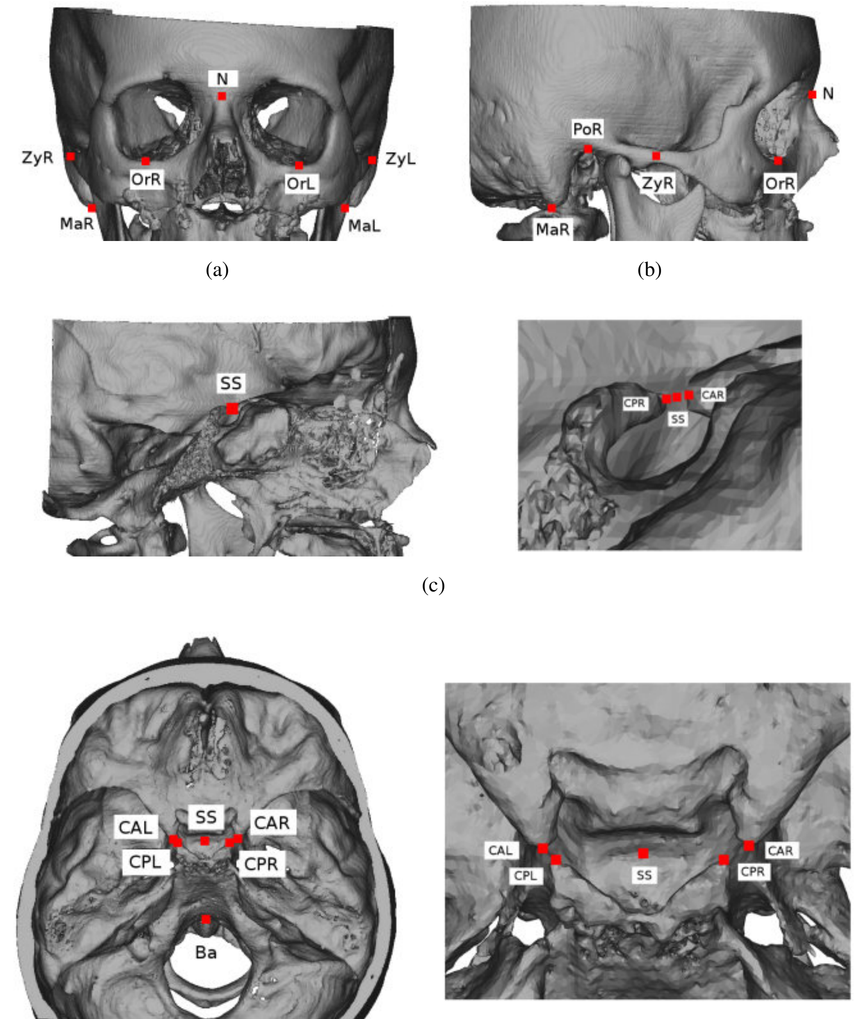

Figure 4.10: Landmarks determined in this study: (a) anterior view, (b) right view, (c) paramedian sagittal view, (d) top view.

4.2.2.3 Reference system

As in the previous study, a standardised coordinate system was set up from the landmarks (see Figure 4.11):

- the MaL-MaR line is parallel to the horizontal plane;
- the Ba-N line is positioned in the midsagittal plane;
- the Ba-N line lies 23° above the horizontal plane;
- the origin is positioned at Ba.

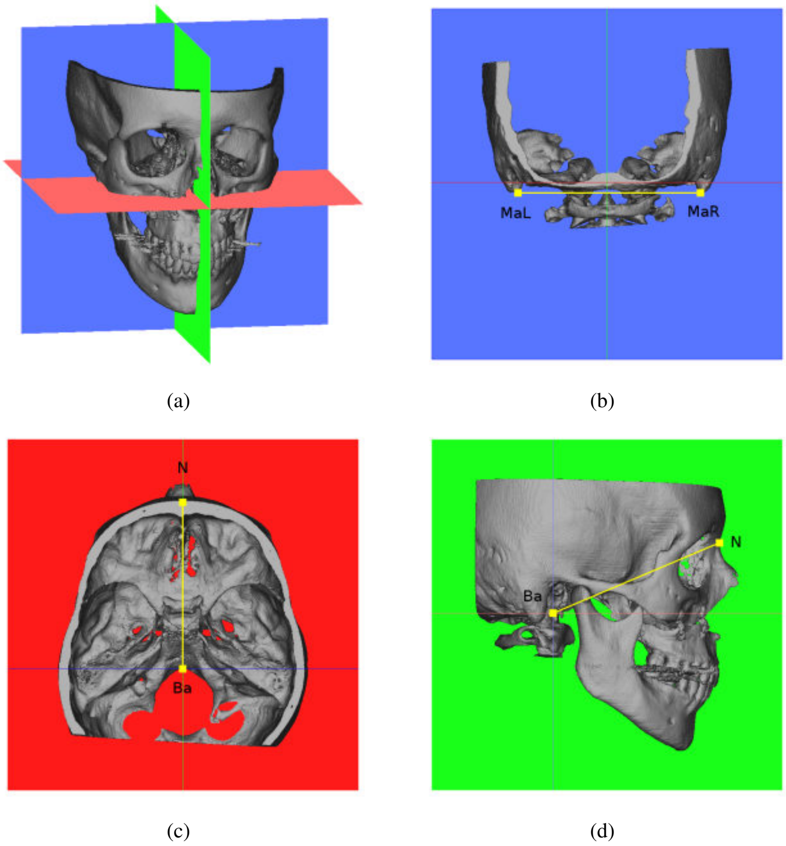

Figure 4.11: Reference system based on landmarks: (a) 3D view, (b) posterior view: the MaR-MaL line is parallel to the horizontal plane, (c) superior view: the Ba-N line is positioned in the midsagittal plane, (d) lateral view: the Ba-N line is situated 23° above the horizontal plane.

The coordinate system is based on the bilateral mastoid points and midsagittal points basion and nasion. Madsen et al. [26] reported a two- to nine-degree average orientation of the sella-nasion line from true horizontal, while the data reported by Kuroe et al. [34] suggest that the mean angle between the sella-nasion and basion-nasion lines is around 17°. Based on these values, it is proposed to put the basion-nasion line 23° above the horizontal plane.

4.2.2.4 Landmark precision

Smoothing
The landmarks were computed from the selected landmark regions using four different numbers of smoothing iterations (0, 4, 10, 20). The influence of smoothing on the landmark coordinates was then studied by calculating the distance between the points obtained without smoothing and the points obtained with smoothing.

Image
Next, the influence of the different triangulated meshes, obtained from each pair of CT images, on the landmark positions was investigated. The pre- and postoperative models were first oriented in the same way using an image registration function in the Mimics software. A coordinate system was then set up using the postoperative landmarks (as described above) and both models were transformed to the new reference frame. Finally, the distance between the pre- and postoperative landmarks was calculated. This process was repeated for the four different numbers of smoothing iterations.

Orientation
The 3D analysis of the skull requires to set up a reference system for each skull model. However, a slightly different orientation might be obtained for two models of the same skull as the reference system depends on the landmark coordinates. The effect of the differences in orientation was investigated by setting up a separate reference system for the pre- and postoperative models. The landmark positions on both models, transformed to their respective reference frames, were compared for one particular number of smoothing iterations.

4.2.3 Results

Smoothing
Figure 4.12 shows the 3D distance between the points obtained without smoothing and the points obtained with smoothing. The mean values across the 24 skull models for three different numbers of smoothing iterations (n) are displayed. All values are below 0.7 mm. The mean values across the landmarks are 0.19 mm (n=4), 0.28 mm (n=10) and 0.33 mm (n=20). In general, the distance increases as the number of smoothing iterations gets larger. However, the variation resulting from additional smoothing iterations decreases (i.e. the first iterations contribute

the most). The effect of smoothing on the landmark coordinates is largest for zygion and mastoid (>0.5 mm).

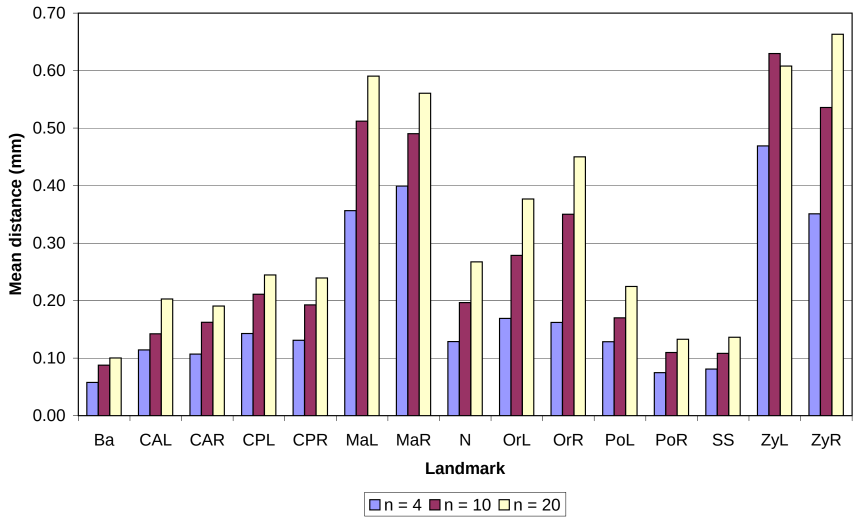

Figure 4.12: Effect of smoothing: mean 3D distance between points obtained without smoothing and with smoothing for different numbers of smoothing iterations (n).

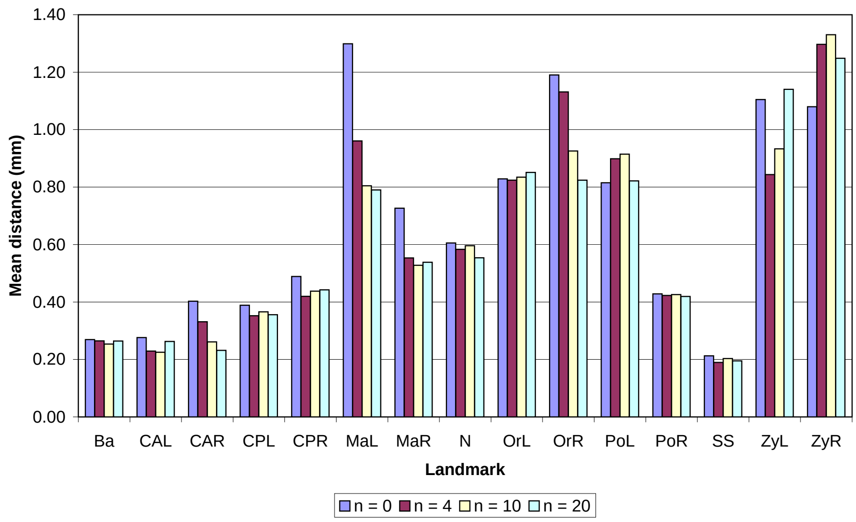

Figure 4.13: Comparison of landmarks calculated on different triangulated meshes, obtained from pre- and postoperative CT images: mean 3D distance for different numbers of smoothing iterations (n).

Image

The mean 3D distance between the 12 pre- and postoperative points for the four smoothing parameters is shown in Figure 4.13. All values are below 1.4 mm. The mean values across the landmarks are 0.67 mm (n=0), 0.62 mm (n=4), 0.60 mm (n=10) and 0.60 mm (n=20). The distance decreases between 0 and 4 iterations for most landmarks, especially for mastoid left, mastoid right and zygion left, while the distance increases for zygion right.

The results for n=10 are displayed in Figures 4.14 (mean values) and 4.15 (maximum values). The distances are split up along the three coordinate axes. A high precision is found for all points, as the mean 3D distance ranges between 0.20 and 1.33 mm. The most reliable landmarks are sella superior, basion and the clinoid points, while zygion, orbitale, porion and mastoid are less reliable. The maximum values of the 3D distances range between 0.33 and 3.57 mm. The maximum 3D distance is smaller than 1 mm for basion, clinoid and sella superior and smaller than 2 mm for 12 out of 15 points. The distance is below 1 mm for nasion in the AP direction, for mastoid, orbitale and porion in the SI direction and for zygion in the ML and SI directions.

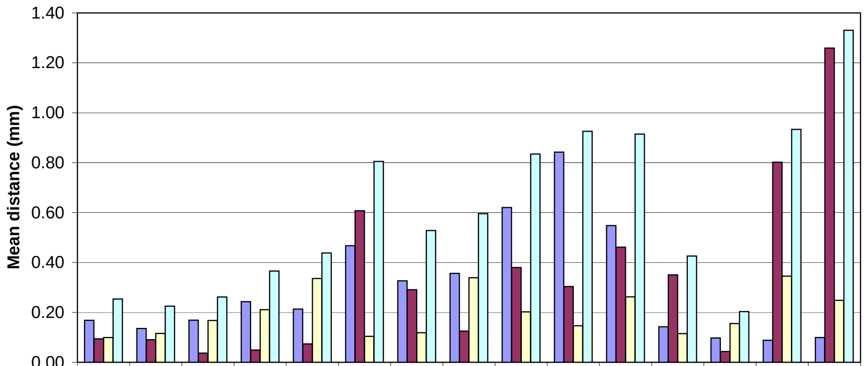

	Ba	CAL	CAR	CPL	CPR	MaL	MaR	N	OrL	OrR	PoL	PoR	SS	ZyL	ZyR
ML	0.17	0.14	0.17	0.24	0.21	0.47	0.33	0.36	0.62	0.84	0.55	0.14	0.10	0.09	0.10
AP	0.09	0.09	0.04	0.05	0.07	0.61	0.29	0.13	0.38	0.30	0.46	0.35	0.04	0.80	1.26
SI	0.10	0.12	0.17	0.21	0.34	0.10	0.12	0.34	0.20	0.15	0.26	0.11	0.16	0.35	0.25
3D	0.25	0.23	0.26	0.37	0.44	0.80	0.53	0.60	0.83	0.93	0.91	0.43	0.20	0.93	1.33

Landmark

ML AP SI 3D

Figure 4.14: Comparison of landmarks calculated on different triangulated meshes, obtained from pre- and postoperative CT images: mean mediolateral (ML), anteroposterior (AP), superoinferior (SI) and total (3D) distance for n = 10.

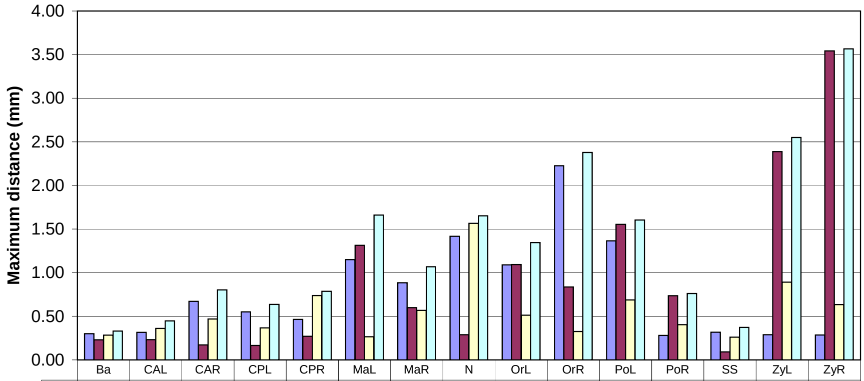

	Ba	CAL	CAR	CPL	CPR	MaL	MaR	N	OrL	OrR	PoL	PoR	SS	ZyL	ZyR
ML	0.30	0.32	0.67	0.55	0.46	1.15	0.88	1.42	1.09	2.23	1.37	0.28	0.32	0.29	0.28
AP	0.23	0.23	0.17	0.17	0.27	1.31	0.60	0.29	1.09	0.84	1.55	0.74	0.09	2.39	3.54
SI	0.28	0.36	0.47	0.37	0.74	0.26	0.57	1.56	0.51	0.33	0.69	0.40	0.26	0.89	0.63
3D	0.33	0.45	0.80	0.64	0.79	1.66	1.07	1.65	1.35	2.38	1.60	0.76	0.37	2.55	3.57

Landmark

ML AP SI 3D

Figure 4.15: Comparison of landmarks calculated on different triangulated meshes, obtained from pre- and postoperative CT images: maximum mediolateral (ML), anteroposterior (AP), superoinferior (SI) and total (3D) distance for n = 10.

Orientation

Figures 4.16 (mean) and 4.17 (maximum) show the distance between the pre- and postoperative points if a reference system is set up for both models separately. Again, the values for n=10 are displayed and split up along the three coordinate axes. The deviation is zero for basion as this is the origin of the coordinate system. Also, nasion is positioned in the midsagittal plane for both models, leading to smaller variations for this point. The precision is relatively similar to that for the registered images, with mean 3D distances up to 1.29 mm and maximum 3D distances up to 4.10 mm. The maximum 3D distance is smaller than 1 mm for basion, clinoid, nasion and sella superior and smaller than 2 mm for 11 out of 15 points. The distance is below 1 mm for mastoid, orbitale and porion in the SI direction and for zygion in the ML direction.

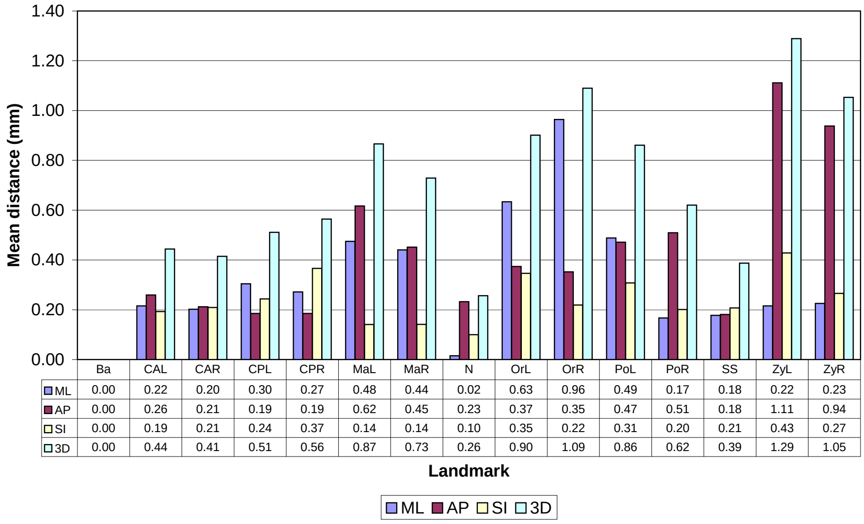

	Ba	CAL	CAR	CPL	CPR	MaL	MaR	N	OrL	OrR	PoL	PoR	SS	ZyL	ZyR
ML	0.00	0.22	0.20	0.30	0.27	0.48	0.44	0.02	0.63	0.96	0.49	0.17	0.18	0.22	0.23
AP	0.00	0.26	0.21	0.19	0.19	0.62	0.45	0.23	0.37	0.35	0.47	0.51	0.18	1.11	0.94
SI	0.00	0.19	0.21	0.24	0.37	0.14	0.14	0.10	0.35	0.22	0.31	0.20	0.21	0.43	0.27
3D	0.00	0.44	0.41	0.51	0.56	0.87	0.73	0.26	0.90	1.09	0.86	0.62	0.39	1.29	1.05

Figure 4.16: Comparison of landmarks calculated on different triangulated meshes, after orienting each mesh separately: mean mediolateral (ML), anteroposterior (AP), superoinferior (SI) and total (3D) distance for n = 10.

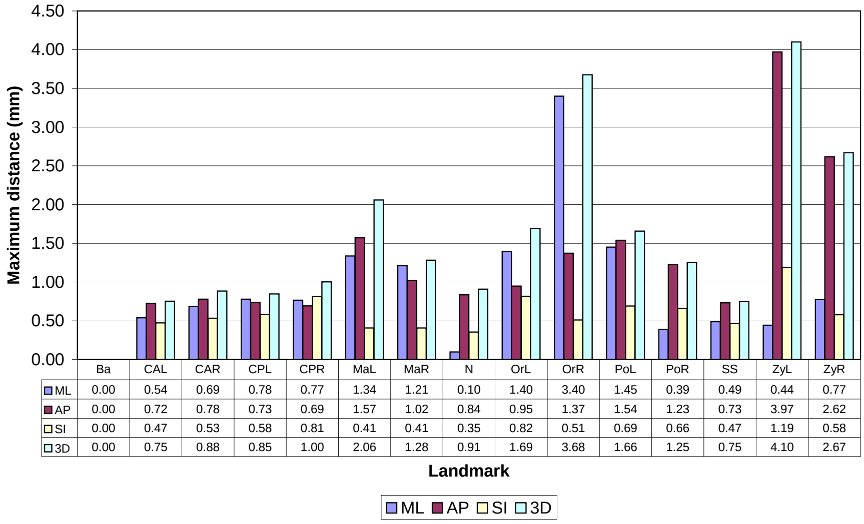

	Ba	CAL	CAR	CPL	CPR	MaL	MaR	N	OrL	OrR	PoL	PoR	SS	ZyL	ZyR
ML	0.00	0.54	0.69	0.78	0.77	1.34	1.21	0.10	1.40	3.40	1.45	0.39	0.49	0.44	0.77
AP	0.00	0.72	0.78	0.73	0.69	1.57	1.02	0.84	0.95	1.37	1.54	1.23	0.73	3.97	2.62
SI	0.00	0.47	0.53	0.58	0.81	0.41	0.41	0.35	0.82	0.51	0.69	0.66	0.47	1.19	0.58
3D	0.00	0.75	0.88	0.85	1.00	2.06	1.28	0.91	1.69	3.68	1.66	1.25	0.75	4.10	2.67

Figure 4.17: Comparison of landmarks calculated on different triangulated meshes, after orienting each mesh separately: maximum mediolateral (ML), anteroposterior (AP), superoinferior (SI) and total (3D) distance for n = 10.

4.2.4 Discussion

The aim of this study was to compare the landmark positions obtained from two CT images of the same skull. In addition, the effect of the number of smoothing iterations on the results was studied. It was found that smoothing up to 20 iterations changes the landmark coordinates by at most 0.7 mm. As also shown in the previous chapter, the smoothing operation does not result in large geometrical errors. The largest variation was obtained for mastoid and zygion. By visualising the landmark positions on the skull models, some local prominences on the mastoid process were seen. By smoothing the model, these prominences become smaller and a different mesh vertex might be selected. The zygomatic arch might be relatively flat at the most lateral part. In this case, a small change in the parameters might result in a different extreme point being detected. The same observation is made for the infraorbital rim.

The precision of the proposed semi-automatic method was evaluated by comparing the pre- and postoperative landmark coordinates. The results for different smoothing iterations show that applying some smoothing improves the precision for most landmarks and the results for ten iterations were further evaluated. It was found that applying additional smoothing does not largely affect the precision of the landmarks. This is in agreement with the observation that the effect of additional smoothing on the edge angles decreases as the number of iterations gets larger, as shown in the previous chapter. In addition, a spline interpolation was used for the ridge and valley regions (Ba, N, Or, Po), which also smooths the geometry.

By looking at the results for ten smoothing iterations, it was found that the points zygion, orbitale, porion and mastoid are least reliable. As observed for the different smoothing iterations, regions that tend to be relatively flat in one of the directions (e.g. ML axis for Or and Po, AP axis for Zy and Po) are more influenced by the exact discretisation of the model. In addition, they are more likely to show larger variations for small changes in the model orientation. Also, as one particular extreme point is extracted from the landmark region, local prominences in the model might increase the variation. The differences in landmark precision correspond to other studies found in literature (see chapter 2), which showed that basion, nasion and sella are among the most reliable points and that zygion, orbitale and porion are usually much more reliable in one of the anatomical directions compared to the other axes.

The mean 3D intraobserver variations were below 1.4 mm, which shows that the precision of all points is clinically acceptable. In chapter 2, mean 3D intraobserver values below 1 mm and interobserver values below 1.5 mm were found for the most reliable points basion, nasion and sella, but 40 % of the mean 3D intraobserver values were above 1.5 mm and 52 % of the mean 3D interobserver values were greater than 2 mm. These results show that the semi-automatic approach allows for an improvement in landmark precision compared to the manual analysis. Moreover, the maximum 3D intraobserver variations are below 2 mm for 11 of the 15 studied landmarks. A major advantage of the automatic analysis might thus be that it is less prone to outlier variations.

Many studies reporting on the precision of landmark localisation do not take into account the variability resulting from setting up a reference system, either manually or based on the landmarks. However, as the head orientation during CT scanning is not standardised, this is an important step of the cephalometric analysis. To split up the movements determined during preoperative planning or postoperative evaluation, the anatomical axes should be determined. In this study, high reproducibility was found for all landmarks if the images are superimposed as well as oriented separately. As the more reliable landmarks or directions are used to set up the reference system, the variability is only slightly increased if the models are oriented separately. While the precision of sella superior was higher than the precision of nasion in this study, the sella turcica region is more prone to have low contrast in the image and was therefore not included in the reference system.

An important limitation of this study is that the landmark regions were identified only once on each skull model by the same observer. Larger variations might be found if the data are processed by different operators or if the time between two analyses is larger. Moreover, only the precision of landmarks on the non-operated part of the skull was determined. Further work should be done to investigate the precision of the landmarks of the maxilla and mandible and the corresponding cephalometric measurements. Finally, the accuracy of the landmark positions should be assessed to further validate the method.

4.3 General discussion and conclusions

A semi-automatic approach for landmark localisation on the 3D virtual skull was developed. Because of the complex anatomy of the skull, it was chosen to let the user select a ROI in which the landmark is located, while the exact position of the point is determined automatically. The literature review of chapter 2 shows that no other studies regarding automatic landmark localisation on the 3D skull model have been presented. The proposed method is novel and allows for a more objective and standardised analysis of the skull.

A new reference frame for cephalometric analysis was presented. In the first study, nasion, sella and orbitale were used to define the coordinate system. However, in the second study, it was found that the points mastoid are more reliable than orbitale. In addition, sella is sometimes difficult to determine because the sella turcica region is more prone to have low contrast in the CT image and can thus be hard to segment, especially using thresholding techniques. Finally, the point basion showed to be very reliable. These observations resulted in a second coordinate system, based on basion, nasion and mastoid. It could be further evaluated if the resulting orientation of the skull is reasonable, i.e. if it allows to determine translations in and rotations around relevant axes. It could be evaluated if bilateral structures are positioned symmetrically relative to the midsagittal plane, as shown in the first study, and if the orientation corresponds to the natural head position. Nevertheless, the precision of the measurements should be the most determining factor for choosing the reference system.

It was shown that the automatic method allows for precise localisation of landmarks on the 3D skull model. The results were compared to studies reporting on manual landmark localisation using 3D images, either multiplanar images or 3D models. Differences in precision between landmarks and anatomical directions were observed and were in agreement with other studies. The mean 3D intraobsever variations are below 1.4 mm and the maximum variations are below 2 mm for 11 of the 15 studied landmarks. A major advantage of the automatic analysis might be that it is less prone to outlier variations.

During the development of the automatic methods, the landmark definitions and landmark computation procedure were optimised to obtain better results. However, some limitations remain. The landmarks are determined through local processing of the surface mesh and by detecting a single extreme point. It was shown that this approach might lead to relatively large variations, especially in the direction where the anatomy is relatively flat. It might thus be better to calculate the landmark position from a larger set of points, e.g. by using the mean value of the most extremal region or by fitting a predefined geometrical shape to the anatomical region. Also, while many cephalometric points are defined as extreme points in one or more anatomical directions, distinct ridges might be better detectable using a curvature analysis in one of the planes. Moreover, the semi-automatic procedure should be employed to detect the landmarks on the jaws, teeth and face and it should be determined which clinically relevant measurements can be obtained to perform a precise 3D cephalometric analysis. Finally, the accuracy of the landmark positions should be assessed to further validate the method.

References

[1] Broadbent BH. A new X-ray technique and its application to orthodontia. Angle Orthod, 1(2):45-66, 1931.

[2] Hofrath H. Die bedeutung der rontgenfern und abstandsaufnahme für die diagnostik der kieferanomalien. J Orofac Orthop, 1(2):232-258, 1931.

[3] Bergersen EO. Enlargement and distortion in cephalometric radiography: compensation tables for linear measurements. Angle Orthod, 50(3):230-244, 1980.

[4] Friedland B. Clinical radiological issues in orthodontic practice. Semin Orthod, 4(2):64-78, 1998.

[5] Dibbets JM, Nolte K. Effect of magnification on lateral cephalometric studies. Am J Orthod Dentofacial Orthop, 122(2):196-201, 2002.

[6] Baumrind S, Frantz RC. The reliability of head film measurements. 1. Landmark identification. Am J Orthod, 60(2):111-127, 1971.

[7] Houston WJ, Maher RE, McElroy D, Sherriff M. Sources of error in measurements from cephalometric radiographs. Eur J Orthod, 8(3):149-151, 1986.

[8] Kamoen A, Dermaut L, Verbeeck R. The clinical significance of error measurement in the interpretation of treatment results. Eur J Orthod, 23(5):569-578, 2001.

[9] Hurst CA, Eppley BL, Havlik RJ, Sadove AM. Surgical cephalometrics: applications and developments. Plast Reconstr Surg, 120(6):92e-104e, 2007.

[10] Grayson B, Cutting C, Bookstein FL, Kim H, McCarthy JG. The three-dimensional cephalogram: theory, technique, and clinical application. Am J Orthod Dentofacial Orthop, 94(4):327-337, 1988.

[11] Mori Y, Miyajima T, Minami K, Sakuda M. An accurate three-dimensional cephalometric system: a solution for the correction of cephalic malpositioning. J Orthod, 28(2):143-149, 2001.

[12] Adams GL, Gansky SA, Miller AJ, Harrell WE Jr, Hatcher DC. Comparison between traditional 2-dimensional cephalometry and a 3-dimensional approach on human dry skulls. Am J Orthod Dentofacial Orthop, 126(4):397-409, 2004.

[13] Alder ME, Deahl ST, Matteson SR. Clinical usefulness of two-dimensional reformatted and three-dimensionally rendered computerized tomographic images: literature review and a survey of surgeons' opinions. J Oral Maxillofac Surg, 53(4):375-386, 1995.

[14] Reuben AD, Watt-Smith SR, Dobson D, Golding SJ. A comparative study of evaluation of radiographs, CT and 3D reformatted CT in facial trauma: what is the role of 3D? Br J Radiol, 78(927):198-201, 2005.

[15] Hildebolt CF, Vannier MW, Knapp RH. Validation study of skull three-dimensional computerized tomography measurements. Am J Phys Anthropol, 82(3):283-294, 1990.

[16] Frühwald J, Schicho KA, Figl M, Benesch T, Watzinger F, Kainberger F. Accuracy of craniofacial measurements: computed tomography and three-dimensional computed tomography compared with stereolithographic models. J Craniofac Surg, 19(1):22-26, 2008.

[17] Park SH, Yu HS, Kim KD, Lee KJ, Baik HS. A proposal for a new analysis of craniofacial morphology by 3-dimensional computed tomography. Am J Orthod Dentofacial Orthop, 129(5):600.e23-600.e34, 2006.

[18] Hwang HS, Hwang CH, Lee KH, Kang BC. Maxillofacial 3-dimensional image analysis for the diagnosis of facial asymmetry. Am J Orthod Dentofacial Orthop, 130(6):779-785, 2006.

[19] Rooppakhun S, Piyasin S, Sitthiseriprati K, Ruangsitt C, Khongkankong W. 3D CT Cephalometric: A method to study cranio-maxillofacial deformities. Papers of Technical Meeting on Medical and Biological Engineering, 6(75-94):85-89, 2006.

[20] Olszewski R, Zech F, Cosnard G, Nicolas V, Macq B, Reychler H. 2007. Three-dimensional computed tomography cephalometric craniofacial analysis: experimental validation in vitro. Int J Oral Maxillofac Surg, 36(9):828-833, 2007.

[21] Taubin G. A signal processing approach to fair surface design. Proceedings of the 22nd Annual Conference on Computer Graphics (SIGGRAPH), Los Angeles, California, USA, pp. 351-358, 1995.

[22] Taubin G. Geometric signal processing on polygonal meshes. Eurographics State of the art report, 2000.

[23] Zorin D, Schröder P, Sweldens W. Interpolating subdivision for meshes with arbitrary topology. Proceedings of the 23rd Annual Conference on Computer Graphics (SIGGRAPH), New Orleans, LA, USA, pp. 189-192, 1996.

[24] Zorin D, Schröder P. Subdivision for modeling and animation. Course notes of the 27th Annual Conference on Computer Graphics (SIGGRAPH), New Orleans, Louisiana, USA, 2000.

[25] Zorin D. Subdivision and multiresolution surface representations. PhD thesis, California Institute of Technology, Pasadena, California, USA, 1997.

[26] Madsen DP, Sampson WJ, Townsend GC. Craniofacial reference plane variation and natural head position. Eur J Orthod, 30(5):532-540, 2008.

[27] Haffner CL, Pessa JE, Zadoo VP, Garza JR. A technique for three-dimensional cephalometric analysis as an aid in evaluating changes in the craniofacial skeleton. Angle Orthod, 69(4):345-348, 1999.

[28] Lagravère MO, Hansen L, Harzer W, Major PW. Plane orientation for standardization in 3-dimensional cephalometric analysis with computerized tomography imaging. Am J Orthod Dentofacial Orthop, 129(5):601-604, 2006.

[29] Swennen GR, Schutyser F, Barth EL, De Groeve P, De Mey A. A new method of 3-D cephalometry Part I: the anatomic Cartesian 3-D reference system. J Craniofac Surg, 17(2):314-325, 2006.

[30] Bettega G, Payan Y, Mollard B, Boyer A, Raphaël B, Lavallée S. A simulator for maxillofacial surgery integrating 3D cephalometry and orthodontia, Comput Aided Surg, 5(3):156-165, 2000.

[31] Olszewski R, Cosnard G, Macq B, Mahy P, Reychler H. 3D CT-based cephalometric analysis: 3D cephalometric theoretical concept and software. Neuroradiology, 48(11):853-862, 2006.

[32] Periago DR, Scarfe WC, Moshiri M, Scheetz JP, Silveira AM, Farman AG. Linear accuracy and reliability of cone beam CT derived 3-dimensional images constructed using an orthodontic volumetric rendering program. Angle Orthod, 78(3):387-395, 2008.

[33] Loubele M, Bogaerts R, Van Dijck E, Pauwels R, Vanheusden S, Suetens P, Marchal G, Sanderink G, Jacobs R. Comparison between effective radiation dose of CBCT and MSCT scanners for dentomaxillofacial applications. Eur J Radiol, 71(3):461-468, 2009.

[34] Kuroe K, Rosas A, Molleson T. Variation in the cranial base orientation and facial skeleton in dry skulls sampled from three major populations. Eur J Orthod, 26(2):201-207, 2004.

5

3D analysis of the femur

In this chapter, two studies about landmark extraction on the femur are presented. The first study deals with the insertion of intramedullary rods and aims at determining the optimal entry point[1]. In addition, the feasibility of a reduced scanning protocol is investigated by applying the method on both full and reduced models of the femur, the latter being obtained by removing specific regions from the model. In the second study, the alignment of the femur in the three anatomical planes is considered by extracting various reference axes.

5.1 Automatic extraction of intramedullary rod entry point

5.1.1 Introduction

Anatomical reference parameters or landmarks are prominent features of an organism. In orthopaedic surgery, landmarks are widely used and mainly employed

[1]This study was published: Van Cauter S, De Beule M, Van Haver A, Verdonk P, Verhegghe B. Automated extraction of the femoral anatomical axis for determining the intramedullary rod parameters in total knee arthroplasty. International Journal for Numerical Methods in Biomedical Engineering, 28(1):158-169, 2012.

for the quantification of morphological parameters (e.g. distances, angles) and the definition of joint coordinate systems. They have proven to be applicable throughout all steps of the patient treatment process: diagnosis [1, 2], preoperative planning [3], surgery [4, 5] and postoperative follow-up [6]. Software programs are available for the manual identification of landmarks on digital medical images and 3D computer models. Moreover, computer methods have been developed to assist the user in landmark identification [7]. Despite these efforts, the manual procedure is time-consuming, requires a high level of expertise, may lack in accuracy and is inherently characterized by observer variability [8–10]. To overcome these drawbacks, techniques for automated landmark extraction are increasingly being developed.

Many studies have shown that accurate prosthetic component positioning is a key factor for the success of joint replacement surgery and recommendations for the joint orientation angles have been presented [11, 12]. One example is total knee arthroplasty (TKA), which aims at restoring the neutral alignment of the mechanical axis of the lower limb (line from the centre of the hip joint through the centre of the knee joint to the centre of the ankle joint). In conventional TKA, however, the femoral anatomical-mechanical angle (FAMA) is used to orient the femoral component with respect to the femoral anatomical axis (FAA). The FAA is defined as the central axis of the diaphysis (or shaft) of the femur and is usually straight in the frontal plane but curved in the sagittal plane. It is determined during surgery by inserting a metal rod into the medullary cavity of the distal femur. A limitation of this procedure is that errors in the entry point location of the intramedullary rod (FIR) may lead to malalignment of the femoral prosthesis [13–15]. An automated preoperative determination of the FAA and, in addition, of the FIR parameters (orientation and entry point), could therefore offer a valuable support to the surgeon and might improve the alignment accuracy in conventional TKA.

Different studies have been performed to automatically determine the FAA on three-dimensional (3D) virtual femur models reconstructed from computed tomography (CT) scans. Mahaisavariya et al. [16] first computed the smallest circular cross section of the medullary canal (shaft isthmus). The proximal and distal FAA were extracted by fitting circles at different levels of the shaft and computing the best fit line to the centre of each circle from the shaft isthmus level in proximal and distal directions. Cerveri et al. [17] applied a Gauss-Newton cylinder fitting algorithm to the middle femoral shaft surface to compute a line approximation of the FAA. Subburaj et al. [18] used a distance-controlled thinning process to extract the medial axis of the femur. This process iteratively removes the outermost surface of the object, while preserving the topology, until a thin medial structure is left. The FAA is then represented by the medial axis of the middle long portion (1/8 to 3/4 of the height) of the femur.

Because of the considerable radiation exposure involved in CT scanning, obtaining scans of the complete femur is not feasible in patient treatment. A new method for computing the FAA and the FIR parameters is therefore proposed, which can be applied to full and reduced 3D models of the femur. The analyses for different reductions of the femur are compared to those of the full femur to study the effect of the scanning reduction.

5.1.2 Materials and methods

5.1.2.1 Bone models

The algorithms were developed and evaluated using CT images of 50 cadaveric femur specimens from the Department of Experimental Anatomy of the Vrije Universiteit Brussel. The images were acquired using a 64-slice CT scanner (LightSpeed VCT, GE Healthcare, Milwaukee, WI) and have a 0.79 x 0.79 mm pixel size and 0.63 mm slice increment. The femurs were segmented with the Mimics® software (Materialise NV, Leuven, Belgium) and 3D triangular surface meshes were created with the gray value interpolation method and without applying smoothing or reduction. The 3D models were then imported into pyFormex (http://www.pyformex.org), which is an open-source program under development at IBiTech-bioMMeda, providing a wide range of operations on surface meshes. All further processing is performed automatically, using some of the general features of pyFormex, combined with newly implemented tools for landmark extraction. First, the GNU Triangulated Surface Library is invoked to reduce the number of edges in the model to 100000, which corresponds to approximately 66668 triangles. The edge reduction algorithm [19] allows for volume, boundary and shape optimisation and equal weights were chosen for these 3 parameters. Next, the model is smoothed with a low-pass filter, which has been shown to preserve the volume of the object [20]. The smoothing filter runs 20 iterations with a scale factor of 0.5.

5.1.2.2 Reference parameters

The presented feature extraction process is intended to be invariant to the orientation of the bone and is therefore started by the determination of a standardised coordinate system for the complete femur. This allows to orient the femurs, which had an arbitrary position during CT scanning, in a standardised way. Next, the femoral middle diaphysis axis (FMDA), which is defined as the straight medial axis of the middle diaphysis, is computed. The FMDA is later on used to simulate a reduced scanning by clipping the femur models along this axis. The procedure then continues by extracting the FAA, which is defined as the curved medial axis of the diaphysis. Finally, the FIR, which is inserted into the distal femur along the FAA, is computed.

Standardised coordinate system
A coarse estimation of the anteroposterior (AP), right-left (RL) and distoproximal (DP) directions of the femur is made by calculating the principal axes of inertia of the outer surface. The centre of gravity (C) of the surface mesh is chosen as the origin. This is illustrated in Figure 5.1. The following step is to select the

correct senses for the axes (e.g. anterior versus posterior) and detect the side of the bone (right or left). Two outer parts are created by cutting the model along the DP direction at 10 and 90 % of its length and the centres of gravity of these parts are calculated. Assuming that C_d and C_p are the centres of gravity of the distal and proximal part, respectively, a number of geometrical conditions are taken into account:

- C_d lies closer to C along the RL axis than C_p (see Figure 5.1 (left));
- C_p is situated anteriorly to C_d (see Figure 5.1 (right));
- C_p lies medially to C (see Figure 5.1 (left)).

The axes (RL,AP,DP) are then modified by rotating the RL axis in the horizontal plane parallel to the posterior condylar line (PCL), which is defined by the most posterior points of the medial and lateral condyles. The coordinate system is shown in Figure 5.2. The posterior condylar points are extracted by creating a right and left distal part, containing the condyles, and computing the most posterior points of these two parts. An iterative process is run to rotate the coordinate system and recalculate the PCL.

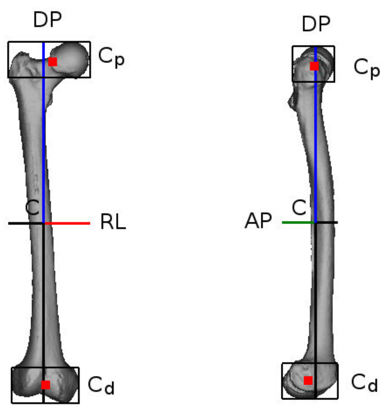

Figure 5.1: Centre of gravity C and principal axes of inertia (RL,AP,DP). C_d and C_p are the centres of gravity of the distal and proximal part.

Geometrical entity fitting

Since the reference parameters that are described in the following sections are determined by fitting geometrical entities (i.e. lines and quadric surfaces), a brief overview of this technique is first given. The fitting problem can be described as finding the set of parameters that minimizes the distance between a set of points and a geometrical entity. Two types of parameters are used. The first one defines

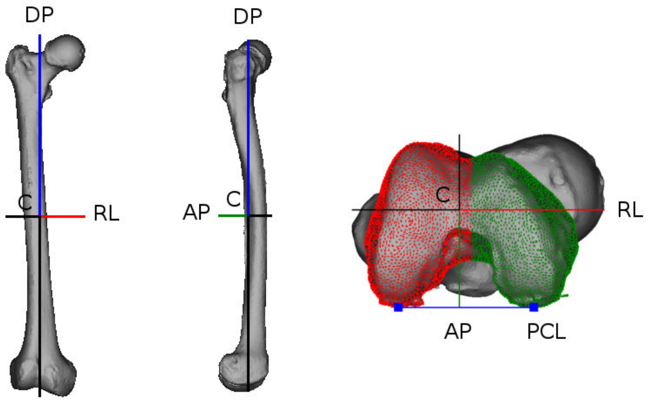

Figure 5.2: The RL axis is rotated in the horizontal plane parallel to the posterior condylar line (PCL).

the size(s) of the geometrical shape (omitted for lines) and the second one defines its position. While the lines are fitted using the exact geometrical distances, approximate geometrical distances are calculated for fitting the quadric surfaces. These distances are found by intersecting the quadric with the average normal vectors of the femur surface at the points. Where the lines do not intersect with the quadric, the distance is computed from the intersection points along three orthogonal axes [21]. The optimal parameters are found by minimizing the sum of squares of the distances using the nonlinear Levenberg-Marquardt least-squares optimisation [22, 23] routine of the SciPy library. Since the Levenberg-Marquardt algorithm finds only a local minimum, an initial guess is provided for the parameter set.

Femoral middle diaphysis axis (FMDA)

The middle shaft is obtained by clipping the surface along DP, symmetric around C, over a height that is equal to half of the femoral length along DP. Next, an elliptic cylinder is fitted to the points of the middle shaft and their corresponding average normal vectors (see Figure 5.3). The centroid of the points and the axes (RL,AP,DP) are used as initial estimates for the centre of the cylinder and its principal axes, respectively. The FMDA is then defined by the longitudinal axis of the cylinder.

Femoral anatomical axis (FAA)

The FAA is computed by fitting a series of elliptic hyperboloids of one sheet to the shaft (see Figure 5.4 (left)). The fitting procedure begins by clipping the diaphysis centrally along DP. The centroid of the selected point set and the axes (RL,AP,DP) are used as starting estimates for the centre of the hyperboloid and its principal

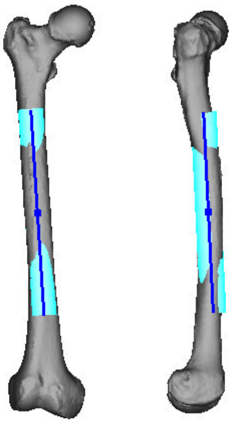

Figure 5.3: Femoral middle diaphysis cylinder and axis (FMDA).

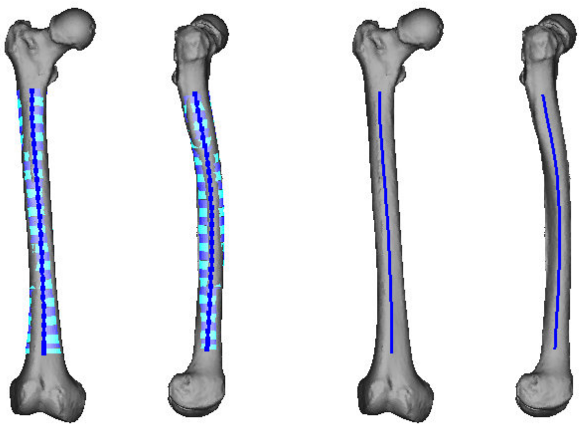

Figure 5.4: Femoral diaphysis hyperboloids and their longitudinal axes (left) and femoral anatomical axis (FAA) (right).

axes, respectively. The procedure is then continued in the proximal and distal directions. Each following point set is generated by clipping the shaft along the longitudinal axis of the previous hyperboloid. The new hyperboloid is initialized by the centroid of the point set and the principal axes of the previous hyperboloid. The longitudinal axis of each hyperboloid is a local linear approximation of the

FAA. The curved medial axis is obtained by computing a cubic Bezier curve, going through the endpoints of the most distal and proximal axes and through the midpoints of the other axes (Figure 5.4 (right)).

A number of prerequisites are implemented to assure a proper outcome for the FAA:

- Each hyperboloid should have a height between 5 and 10 mm. A minimum height is used to provide enough surface points to perform a correct fitting. A maximum height is applied to allow capturing the curved nature of the diaphysis by generating a sufficient number of hyperboloids.

- The angle between the axis along which the shaft is clipped, and the longitudinal axis of the fitted hyperboloid, should not be larger than 5°. Otherwise, there might be a large difference between the point set to which the hyperboloid is fitted and the point set that is generated along the resulting longitudinal axis, and this axis might therefore be a poor representation of the FAA. When the angle is larger than 5°, a new fitting procedure is started, using the axes of the previously fitted hyperboloid as a starting estimate. A maximum number of 5 trials are allowed, assuming that the cross section of the femur is not nearly elliptical in that region if no convergence is achieved.

- To find the distal and proximal endpoints of the FAA, a stop criterion is implemented, stating that the radius change along the axis should not be larger than 10 %. This is evaluated by computing the radius and arc length for each point that defines the FAA and constructing a cubic Bezier curve of the radii versus the arc lengths. The slope of this curve is a measure for the radius change over the FAA. The radius at a point is calculated as the equivalent radius (i.e. radius of the circle with equivalent area) of the polygonal cross section of the femur surface at that point.

Femoral intramedullary rod (FIR)
The orientation of the FIR is obtained by fitting a line to the distal FAA and the entry point of the rod is calculated by intersecting this line with the distal femoral surface. This is shown in Figure 5.5. A series of points at equal distance of approximately 1 mm are first generated along the FAA. The points are equally spread via a polyline approximation of the FAA, which is obtained by subdividing the curve using de Casteljau's algorithm until all Bezier parts are sufficiently flat. An initial guess for the FIR orientation is provided using the principal axis of inertia with the smallest principal value. A rod length of 200 mm is assumed and an iterative process is run to fit a line to the points of the FAA lying within 200 mm from the entry point of the rod.

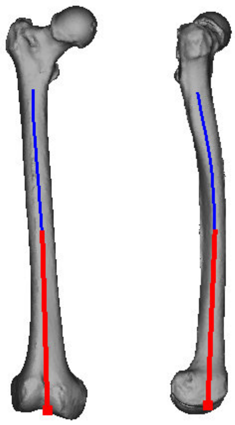

Figure 5.5: Femoral intramedullary rod (FIR).

5.1.2.3 Reduced femur models

To simulate the effect of obtaining a partial scan of the patient's leg, all 50 femur models are reduced along their FMDA. The scan heights are expressed in mm and not as percentages of the total femoral length to allow for a more practical implementation of the scanning protocol. The model is first clipped into a distal, central and proximal part, with heights of 150, 50 and 150 mm, respectively. Figure 5.6 (left) shows the reduced femur model and its FAA. It should be noticed that the FAA is estimated at the non-scanned regions by interpolating between the different parts. Because only the triangles of the surface mesh that fall completely between the clipping planes, are included, an additional prerequisite is implemented for determining the FAA on the reduced models. The triangles and corresponding points to which the hyperboloid is fitted should have a closed cross section over at least 5 mm. This assures that enough surface points are available for a good fitting. The central part of the model is then further reduced to study the effect on the FAA and FIR parameters. Its height is repeatedly decreased by 10 mm until large deviations from the results for the full models are observed. Next, the distal and proximal parts are repeatedly diminished by 10 mm to find the acceptable scanning reduction. The second configuration consists of a distal and proximal part (shown in Figure 5.6 (right)). The analysis starts again with a height of 150 mm for each part, which is then reduced in 10 mm decrements.

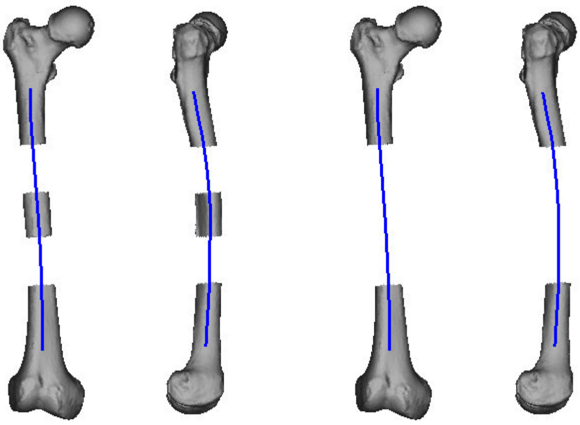

Figure 5.6: FAA computed on a reduced femur model consisting of three parts (left) and two parts (right): the curve is interpolated between the different parts.

5.1.2.4 Evaluation

Full femur models

The performance of the automated techniques is studied on the 50 full femur models. The computation time for extracting the anatomical features is recorded (T). The edge reduction and smoothing operations are performed in advance to the feature extraction procedure and are thus not included in the computation time. The analyses are run on a regular laptop (Dell M4300, processor 2x Intel® Core™2 Duo CPU T9300 @ 2.50GHz, memory 2059MB). Furthermore, the 95th percentiles of the distances of the geometrical entity fittings are calculated for the FMDA cylinder, FAA hyperboloids and FIR lines (FMDA-FIT / FAA-FIT / FIR-FIT). For the FAA, a mean value over all hyperboloids that are fitted to the diaphysis, is used.

In addition, some clinical parameters are studied for the 50 models: the length of the femur along the FMDA (FDP-FPP); the distances of the distal and proximal endpoints of the FAA to the most distal and proximal points of the femur, respectively (FAA-FDP / FAA-FPP); the angle from the FMDA to the FIR in the coronal and sagittal planes (FMDA-FIR-COR / FMDA-FIR-SAG).

Finally, the orientation-invariance of the procedure is evaluated by randomly rotating one femur 100 times (three random angles around the x, y and z-axes) and comparing the results with those of the initial femur.

Comparison between full and reduced models

To determine the effect of the scanning reduction, the analyses of the full and reduced models are compared, by computing the following values: maximum/mean orthogonal distances between the FAA (FAA-max / FAA-mean); 3D distances between the distal/proximal endpoints of the FAA (FAA-DP / FAA-PP); absolute 3D angle between the axes of the FIR (FIR-A); 3D distance between the entry points of the FIR (FIR-EP). To find the orthogonal distances between the curves, a polyline approximation of each curve is first computed. Next, a series of points and corresponding tangent vectors at equal distance of approximately 1 mm are calculated along each polyline. Finally, the distances of each point set from the other polyline, perpendicular to the corresponding tangent vectors, are computed.

5.1.3 Results

Table 5.1 shows the performance parameters for the analyses of the 50 full femur models (mean, standard deviation and range). The feature extraction process is fast and good results are obtained for the geometrical entity fitting (95th percentile distances between 0.48 and 5.47 mm). Comparable results are found for the reduced models.

The results for the clinical parameters are given in Table 5.2. The difference in length between the shortest and largest femur model is 120.63 mm, which resulted in 28.72 and 33.21 mm ranges for the FAA-FDP and FAA-FPP. On average, the FIR is parallel to the FMDA in the coronal plane, while the anterior bow of the femur results in a positive angle between the FMDA and the FIR in the sagittal plane.

Comparing the results of the rotated femurs with those of the initial femur resulted in maximum deviations of 0.05 mm (FAA-max), 0.04 mm (FAA-DP and FAA-PP), 0.02° (FIR-A) and 0.06 mm (FIR-EP), which demonstrates that the feature extraction procedure is indeed orientation-invariant.

Table 5.1: Performance parameters for the 50 full femur models.

	Mean ± SD	Range
T (sec)	20 ± 4	12 - 31
FMDA-FIT (mm)	4.00 ± 0.54	2.83 - 5.47
FAA-FIT (mm)	1.48 ± 0.24	0.96 - 2.05
FIR-FIT (mm)	1.18 ± 0.42	0.48 - 2.69

Table 5.2: Clinical parameters for the 50 full femur models.

	Mean ± SD	Range
FDP-FPP (mm)	448.87 ± 28.53	393.84 - 514.47
FAA-FDP (mm)	72.19 ± 6.74	57.35 - 86.07
FAA-FPP (mm)	87.45 ± 7.97	72.46 - 105.67
FMDA-FIR-COR (°)	0.02 ± 0.94	-2.16 - 2.02
FMDA-FIR-SAG (°)	3.77 ± 0.96	1.65 - 5.75

Figure 5.7 shows the comparison between the full models and the reduced models consisting of a distal, central and proximal part. The length of the outer parts is fixed and equal to 150 mm. The length of the central part varies between 50 and 20 mm. It was found that for a central height of 10 mm, no hyperboloids are fitted to this part. This is caused by the fact that the central part does not have a closed cross section over at least 5 mm.

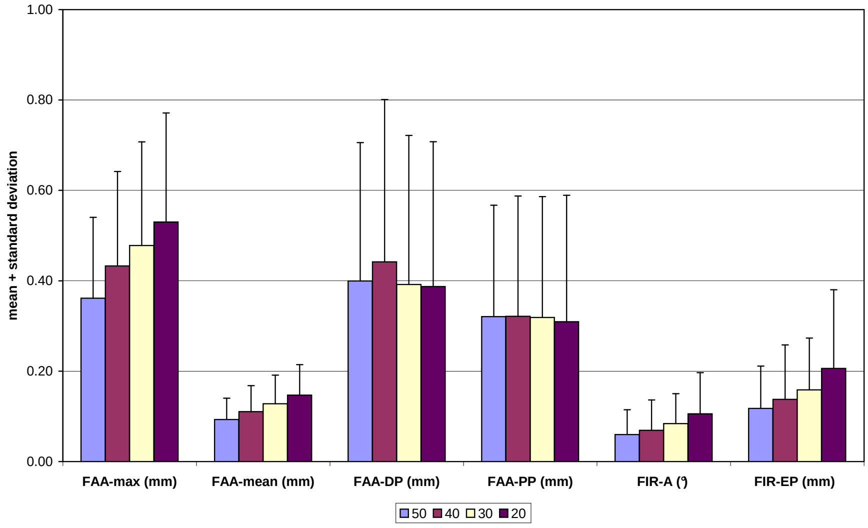

Figure 5.7: Comparison of the analyses of the 50 full models and reduced models consisting of three parts: effect of reducing the central part.

The reduction of the outer parts for a central height of 20 mm is depicted in Figure 5.8. The result for the outer parts of 110 mm shows a large increase for the FAA-DP and FAA-PP. In this case, the maximum values for these distances are 12.37 and 11.14 mm. Using a height of 120 mm gives the following results (mean $\pm$ SD): 0.92 $\pm$ 0.34 mm (FAA-max), 0.32 $\pm$ 0.11 mm (FAA-mean), 0.38 $\pm$ 0.34 mm (FAA-DP), 0.41 $\pm$ 0.45 mm (FAA-PP), 0.17 $\pm$ 0.16° (FIR-A), 0.29 $\pm$ 0.28 mm(FIR-EP). The maximum values are 1.94 mm (FAA-max), 0.59 mm (FAA-mean), 1.70 mm (FAA-DP), 2.77 mm (FAA-PP), 0.66° (FIR-A), 1.25 mm (FIR-EP).

Finally, Figure 5.9 gives the comparison for the reduced models consisting of a distal and proximal part, with lengths between 150 and 110 mm. The results for the FAA-DP and FAA-PP are comparable to those of the models with a central part. A large increase of the values is observed, however, for the 4 other parameters.

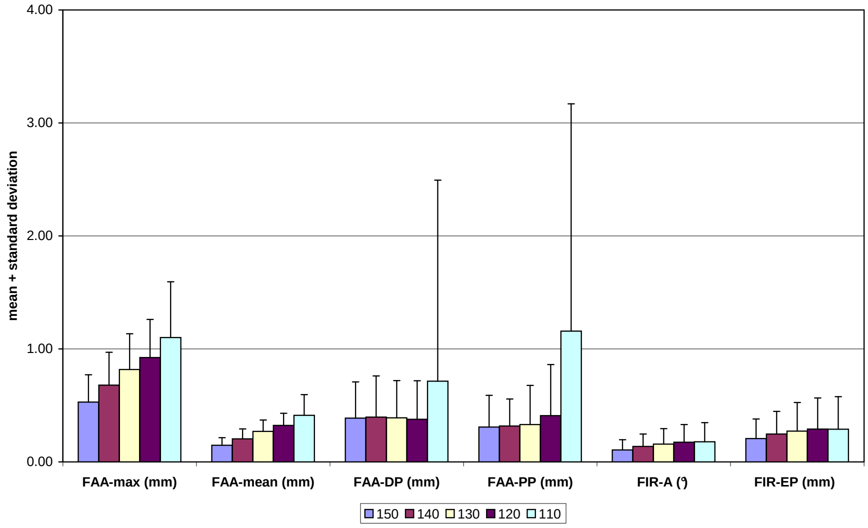

Figure 5.8: Comparison of the analyses of the 50 full models and reduced models consisting of three parts: effect of reducing the outer parts.

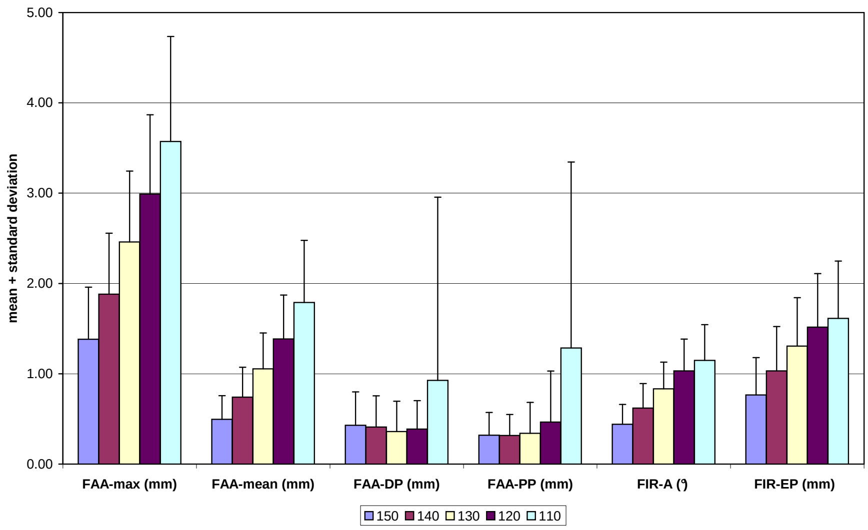

Figure 5.9: Comparison of the analyses of the 50 full models and reduced models consisting of two parts: effect of reducing the parts.

5.1.4 Discussion

Conventional TKA instruments use an intramedullary rod to reference the medullary canal and perform the distal femoral resection usually at a fixed amount of 5 to 6° of valgus to the distal FAA [24, 25]. This puts the femoral component approximately in the desired orthogonal alignment relative to the mechanical axis (FMA), assuming that the FAMA is in the same normal range of valgus. However, anatomical variations may alter the FAMA [24, 25] and consequently result in malalignment of the FMA. Several studies have indeed shown that inaccurate femoral component placement can result from anatomical variations, such as excessive femoral bowing and capacious medullary canals [26, 27] and recommended to determine a patient-specific distal resection angle on a preoperative long-leg radiograph.

In this study, the first step in the patient-specific process, which is the determination of the FAA and subsequently the FIR orientation and entry point, was automated. The feature extraction methods were developed for 3D models, e.g. reconstructed from CT images, because there is an increased interest for preoperative surgery planning using 3D imaging methods in orthopaedics. The automated procedure offers a fast and user independent way for extracting landmarks. As a local optimisation routine is used for the geometric entity fitting, an initial estimate should be provided for some of the reference parameters. This could be achieved by orienting the femurs in a standardised way and using the resulting coordinate system as an estimate for extracting the FMDA and FAA. The 95th percentiles of the distances of the geometrical entity fittings show that the local optimum gives a good result for the FMDA, FAA and FIR. A larger mean value of 4 mm is found for the FMDA because the cylinder is a linear approximation of the curved middle diaphysis.

The femur models were then reduced to study the effect of partially scanning the patient's leg. A large variation is observed for the femoral length and the distances of the FAA endpoints to the most distal and proximal points of the femur (range of 120.63, 28.72 and 33.21 mm, respectively). This should be kept in mind when trying to find the acceptable scanning reduction. When fixed scanning heights are used, an over- or underestimation may be made in some cases. However, a safe zone that works for most of the cases should be determined, while the scanning height could be adjusted for excessive short or long legs. The comparison between the full models and reduced models consisting of a distal, central and proximal part (Figures 5.7 and 5.8) indicates that the scanning heights can be reduced to 120, 20 and 120 mm, respectively, without a significant change in the results for the reference parameters. Further reducing the central part to 10 mm causes the FAA to interpolate directly between the outer parts, because no hyperboloids are fitted centrally in this case. The large standard deviations and maximum values for the FAA-DP and FAA-PP of the outer parts of 110 mm demonstrate that in this case some outliers are present. For some femur models, too few hyperboloids are fitted to the outer parts to obtain precise results. Good results for all parameters are obtained with the outer heights of 120 mm and central height of 20 mm. This reduction corresponds to approximately 58 % of the mean length of the femurs. The mean values for the deviation from the full femur models are smaller than 1 mm (FAA), 0.5 mm (FAA-DP and FAA-PP) and 0.2° and 0.3 mm (FIR). The maximum values are smaller than 2 mm (FAA), 2.8 mm (FAA-DP and FAA-PP) and 0.7° and 1.3 mm (FIR). Figure 5.9 shows that, except for the FAA endpoints, omitting the central part from the model results in significantly larger deviations from the full model. The inclusion of the central part allows to better capture the curved nature of the diaphysis, which is reflected in the orthogonal distance between the FAA curves and in the intramedullary rod parameters. The anterior bow is a prominent feature of the femoral shaft, which is also demonstrated by the FMDA-FIR-SAG angle of 3.77° ± 0.96°. Although the FAA is usually straight in the frontal plane, inward or outward bowing may, however, also be present. This is demonstrated by the FMDA-FIR-COR angle, which has a mean value of 0.02° and a range of -2.16° to 2.02°.

Using the automated techniques presented in this study, a preoperative analysis of the intramedullary rod parameters could be accomplished, in minimal time and without observer variability. However, some limitations of the current study should be mentioned. The anatomical axis was defined as the medial axis of the diaphysis in this study. For the extraction of the optimal intramedullary rod entry point, however, it should be verified if this axis corresponds well to the medial axis of the medullary canal. Also, a relatively short rod length was chosen. As larger rods may inhibit a complete insertion because of the curved nature of the medullary canal, it will be important to take into account the rod and canal width. Although the feature extraction process is fully automated, manual processing of the CT data is still needed to segment the femur and obtain the 3D models. This process can be quite tedious, especially at the hip and knee joint, where the articular surfaces of the bones may be connected in the CT scans. Furthermore, edge reduction and smoothing operations are performed on the 3D models. It should therefore be investigated how these operations effect the results for the FAA and FIR. Finally, the computed reference parameters should be evaluated by comparison with a reference parameter set obtained by manual analysis. Further work should also be done to extract the FMA (and thus the hip and knee centres) to find a patient-specific distal femoral resection angle.

It has been shown that computer navigation systems may improve the accuracy of limb mechanical axis alignment and prosthetic component orientation [28]. As these systems align the femoral component based on the FMA, there is no need for determining the FAA. Navigation technology is used in few centres, however, and the cost of most systems may limit its access for smaller, low-volume institutions [29]. Moreover, to date no long-term studies have proven that navigation improves postoperative functional kinematics, allows for a more rapid recovery, or decreases complication rates [4]. Conventional instruments, such as intramedullary rods, are still commonly used [30], and automated feature extraction techniques could offer a valuable support to the surgeon and could possibly aid in improving the accuracy of TKA performed with these instruments.

5.1.5 Conclusions

An increased interest for preoperative surgery planning using 3D imaging methods is shown in orthopaedics. The automated extraction of anatomical reference parameters could improve the speed and precision of these preoperative studies and the accuracy of surgery. In this study, a new method for extracting the FAA was developed and tested on 50 femur models. Moreover, the FAA extraction was applied to conventional TKA, by computing the orientation and entry point of an intramedullary alignment rod with a length of 200 mm. The same methods were also used to study reduced models of the femur and it was shown that the reference parameters can be precisely determined by partially scanning the patient's thigh. These computer aided techniques could eventually be used to perform a preoperative planning of TKA and thus obtain a patient-specific distal femoral resection angle and entry point for conventional TKA instruments.

5.2 Automatic analysis of femur alignment

5.2.1 Introduction

Correct alignment of the prosthesis components is a crucial factor for the success of TKA [31, 32]. Postoperative malalignment has been associated with instability, stiffness, loosening and patellar dislocation [33–35] and is typically defined as a deviation of 3° or more from the targeted position [36, 37]. Several factors may contribute to errors in prosthesis alignment, such as observer variability during preoperative planning, difficulties in locating the reference axis during surgery and improper positioning of surgical instruments. The first source of error, i.e. the subjective perception of the operator during surgical planning, might be overcome by using automatic methods to determine the alignment of the limbs and prostheses. Several techniques for automatic landmark extraction on 3D images of the lower limbs have been presented, but only few studies on distal femoral alignment have been published [18, 38]. This study aims at applying automatic methods to extract the reference axes of the distal femur. In addition, the alignment of the bone is studied by calculating relevant angular measurements. The mean values for ten femurs are determined and compared to literature.

5.2.2 Materials and methods

5.2.2.1 Bone models

The algorithms were applied on CT images of 10 cadaveric femur specimens from the Department of Experimental Anatomy of the Vrije Universiteit Brussel. The images were acquired using a 64-slice CT scanner (LightSpeed VCT, GE Healthcare, Milwaukee, WI) and have a 0.79 x 0.79 mm pixel size and 0.63 mm slice increment. The femurs were segmented with the Mimics® software (Materialise NV, Leuven, Belgium) and 3D triangular surface meshes were created with the gray value interpolation method and without applying smoothing or reduction. The 3D models were then imported into pyFormex, reduced to 100000 edges and smoothed with a low-pass filter of 20 iterations with scale factor 0.5.

5.2.2.2 Reference axes

Table 5.3 gives an overview of the reference axes that are determined in this study. Several automatic landmark extraction methods are applied to deal with the different types of landmark definitions (e.g. central point, extreme point along certain anatomical direction or point of extreme curvature).

Table 5.3: Axis definitions.

Landmark	3D definition
Femoral anatomical transepicondylar axis	Line joining the prominences of the lateral and medial femoral epicondyles
Femoral central anatomical axis	Medial line of the central 1/3th of the femur
Femoral cylindrical axis	Medial line of two collinear best-fit cylinders to the circular parts of the lateral and medial femoral condyles
Femoral distal condylar axis	Line joining the most distal points of the lateral and medial femoral condyles
Femoral mechanical axis	Line joining the centre of the femoral head and the most anterior point of the femoral notch
Femoral posterior condylar axis	Line joining the most posterior points of the lateral and medial femoral condyles
Femoral trochlear AP axis	Line joining the deepest point of the trochlear groove with the most anterior point of the femoral notch

Axial alignment
As in the previous study, the landmark extraction process starts with estimating the anatomical directions by computing the principal axes of inertia of the surface mesh. Next, the central anatomical axis is determined as the longitudinal axis of the best-fit elliptic cylinder to the central 1/3th of the femur. The mechanical axis is defined as the line connecting the centre of the hip and the centre of the knee. The femoral hip centre is extracted as the centre of the best-fit sphere to the femoral head. Next, the femoral notch is identified. A series of sagittal intersections through the intercondylar fossa is made and for each cross-section, the point of maximum curvature lying on the notch is detected. This is illustrated in Figure 5.10. The left part of the figure shows the curvature values in a sagittal cross-section and the point of maximum curvature on the femoral notch (in black).

The femoral notch points for the different cross-sections are displayed in the right part of the figure. The femoral knee centre is then defined as the most anterior point of the notch. Finally, the femur model is aligned along the mechanical axis and the distal condylar axis is found by iteratively computing the most distal points on the lateral and medial condyles and rotating the RL axis in the frontal plane parallel to the distal condylar axis.

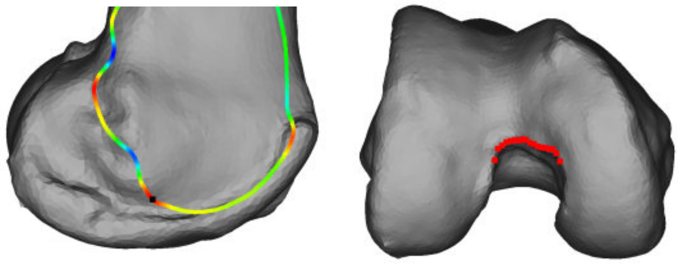

Figure 5.10: Extraction of the femoral notch: curvature analysis in sagittal cross-section with notch point shown in black (left) and notch points for different cross-sections (right).

Rotational alignment
Similarly to the distal condylar axis, the posterior condylar axis is extracted by aligning the model along the mechanical axis and iteratively computing the most posterior points on the lateral and medial condyles and rotating the RL axis in the horizontal plane parallel to the posterior condylar axis. Then, the cylindrical axis is found as the longitudinal axis of two collinear best-fit cylinders to the circular parts of the lateral and medial condyles. This is shown in Figure 5.11. The cylinders are fit to the mesh vertices at the posterior condyles for which the angle between their normal vector and the mechanical axis, projected in the sagittal plane, lies between 20° and 120° [39]. For each cylinder, a small strip of the posterior condyle is selected along the RL axis. Finally, the transepicondylar and trochlear AP axes are determined by projecting the 3D mesh of the femur onto the horizontal plane and detecting the points of local maximum or minimum curvature (see chapter 3).

The following coordinate system is set up from the axes: the longitudinal axis is parallel to the mechanical axis and the transverse axis is parallel to the posterior condylar line in the horizontal plane. The origin is positioned at the centre of gravity of the surface mesh. The extracted reference axes are then projected onto the anatomical planes and relevant angles are calculated.

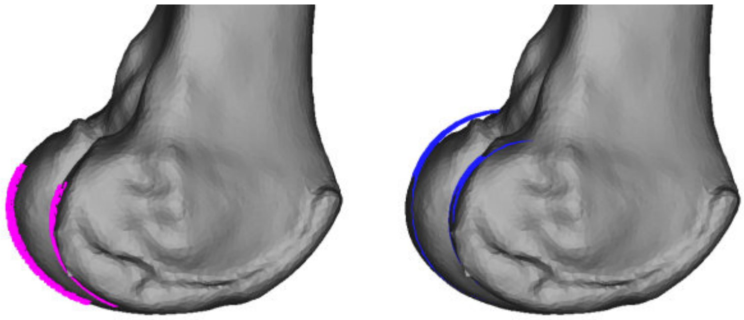

Figure 5.11: Extraction of the femoral cylindrical axis: circular parts of the posterior condyles (left) and their best-fit collinear cylinders (right).

5.2.3 Results

The axes for one of the femurs are displayed in Figure 5.12. The mean values and standard deviations of the angular measurements are summarised in Table 5.4. It should be noticed that for the distal condylar and trochlear AP lines, the perpendicular to the reference axis is used. The anatomical axis is on average in 6.9° valgus to the mechanical axis and has a low SD. The average coronal angle between the mechanical and distal condylar axis is 3.4° valgus, with nine femurs in valgus and one in varus alignment. In the sagittal plane, the central anatomical axis is in 3.2° flexion to the mechanical axis. In the horizontal plane, all axes are on average in external rotation to the posterior condylar line. A large SD is found for the trochlear AP axis, which is internally rotated in three cases. The cylindrical axis is closest to the posterior condylar line and has the lowest SD.

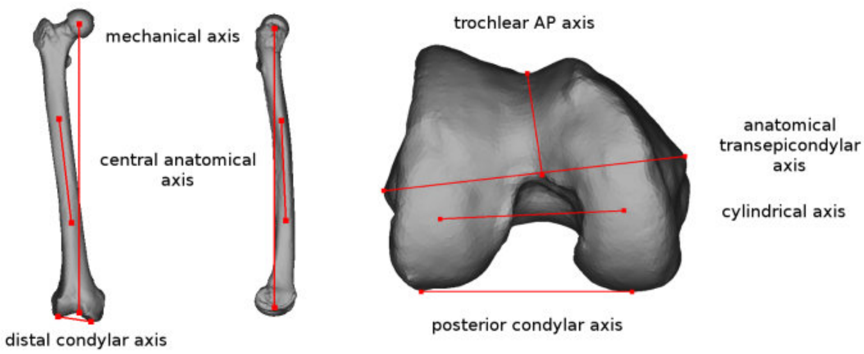

Figure 5.12: Computed reference axes (front, right and bottom view).

Table 5.4: Angular measurements of alignment (positive values correspond to valgus, flexion and external rotation).

Angle	plane	mean (°)	SD (°)
Mechanical axis - central anatomical axis	frontal	6.9	0.9
Mechanical axis - distal condylar axis	frontal	3.4	2.9
Mechanical axis - central anatomical axis	sagittal	3.2	1.9
Posterior condylar axis - anatomical transepicondylar axis	horizontal	7.9	1.6
Posterior condylar axis - cylindrical axis	horizontal	2.3	1.2
Posterior condylar axis - trochlear AP axis	horizontal	3.3	5.3

5.2.4 Discussion

Several studies on alignment of the normal lower limbs have been published. Paley [40] reported normal coronal angles of $7° \pm 2°$ between the femoral mechanical and anatomical axis. Also, the normal femoral distal condylar line is on average oriented in 3° valgus to the femoral mechanical axis. The automatically computed angles seem to correspond to these mean normal values. A review study on rotational alignment was presented by Victor [41]. He reported that the surgical and anatomical transepicondylar axis and the perpendicular to the trochlear AP axis are on average 3°, 5° and 4° externally rotated to the posterior condylar line. Also, the greatest interindividual variability was observed for the trochlear AP axis. Middleton and Palmer [42] measured 50 cadaveric distal femurs and found that the trochlear AP axis was on average perpendicular to the surgical transepicondylar axis (91°), but there was a large spread in the angles (SD of 4.7°). Our mean angle between the posterior condylar and trochlear AP axis and the large SD compared to the other angles are thus in agreement with other studies. However, only 10 femurs were studied and because of the large spread in the angles, the values should be carefully interpreted. Moreover, the deepest point of the trochlear groove was identified on a 2D horizontal view of the femur. By visualising the results, it was found that the deepest point may shift mediolaterally if the femur is rotated around the ML axis. The anatomical transepicondylar axis is 3° more externally rotated to the posterior condylar line compared to literature. This might be a result of the 2D projection of the femur model onto the horizontal plane. It seems that a 3D analysis should be preferred to find the bony prominences on the epicondyles. In addition, the medial sulcus should be identified to determine the surgical transepicondylar axis. The angle between the anatomical transepicondylar and cylindrical axis was measured by Eckhoff et al. [43]. They found an average difference of 2.3° (range 0.2° - 2.5°) in the horizontal plane for 23 knees. Assuming that the anatomical transepicondylar axis is 5° externally rotated to the posterior condylar line, the mean angle between the cylindrical and posterior condylar axis would be 2.7° and corresponds to our computed value. However, comparing the data to mean values reported in literature only serves as a first evaluation of the results. Further work should be done to assess the accuracy of the reference axes.

5.3 General discussion and conclusions

It was shown in chapter 2 that multiple studies on automatic landmark localisation on the lower limbs have been presented. However, in many papers, a limited amount of parameters is measured by using one or two feature extraction techniques. In this chapter, it was shown that by applying different methods for feature extraction, several geometrical parameters of the femur can be obtained. In the first study, the 3D femoral anatomical axis was extracted and used to determine the optimal intramedullary rod entry point. In addition, it was shown that precise measurements could be obtained using a reduced scanning protocol. Including the central part of the femur is required to correctly measure femoral bowing. In the second study, various reference axes to study femoral alignment were measured. Relevant angular measurements in the three anatomical planes were made and it was shown that most measurements are in agreement with mean values reported in literature. The automatic techniques can contribute to a faster and more precise 3D planning and evaluation of TKA.

The main advantage of the 3D analysis might be that the 3D relation between the axes can be obtained and that the measurements can be projected in any plane. For example, it has been shown that the flexion-extension axis of the knee (approximated by the cylindrical axis in this study) is not perpendicular to the traditional sagittal plane, which means that it is difficult to measure using conventional 2D images. Also, while the anatomical axis is usually straight in the frontal plane, inward or outward bowing may occur. As the bowing direction may change when the limb is internally or externally rotated, 2D images might be more prone to errors in measuring the coronal angle between the mechanical and anatomical axis. The main advantage of the automatic approach is that it eliminates observer variability. In addition, several parameters, such as the curved anatomical axis and cylindrical axis, can not be found by simply connecting two points lying on the bone, and are hard to determine manually.

The main limitation of the current work is that the automatically determined measurements were only compared to mean values found in literature. The accuracy of the reference axes should be assessed to further validate the method. Also, the medullary canal should be segmented to verify if the extracted medial axis of the diaphysis corresponds well to the medial axis of the medullary canal and to detect cases where the rod will impinge on the cortex. Finally, a 3D analysis of the femoral trochlear groove and epicondyles should be performed.

References

[1] Delaunay S, Dussault RG, Kaplan PA, Alford BA. Radiographic measurements of dysplastic adult hips. Skeletal Radiol, 26(2):75-81, 1997.

[2] Muhle C, Brossmann J, Heller M. Kinematic CT and MR imaging of the patellofemoral joint. Eur Radiol, 9(3):508-518, 1999.

[3] Nofrini L, Martelli S, Iacono F. In vivo evaluation of a computer planning system for total knee arthroplasty. Comput Methods Programs Biomed, 73(1):71-81, 2004.

[4] Siston RA, Giori NJ, Goodman SB, Delp SL. Surgical navigation for total knee arthroplasty: a perspective. J Biomech, 40(4):728-735, 2007.

[5] Ziegler CG, Pietrini SD, Westerhaus BD, Anderson CJ, Wijdicks CA, Johansen S, Engebretsen L, Laprade RF. Arthroscopically pertinent landmarks for tunnel positioning in single-bundle and double-bundle anterior cruciate ligament reconstructions. Am J Sports Med, 39(4): 743-752, 2011.

[6] LaPrade RF, Oro FB, Ziegler CG, Wijdicks CA, Walsh MP. Patellar height and tibial slope after opening-wedge proximal tibial osteotomy: a prospective study. Am J Sports Med, 38(1):160-170, 2010.

[7] Hankemeier S, Gosling T, Richter M, Hufner T, Hochhausen C, Krettek C. Computer-assisted analysis of lower limb geometry: higher intraobserver reliability compared to conventional method. Comput Aided Surg, 11(2):81-86, 2006.

[8] Lerner AL, Tamez-Pena JG, Houck JR, Yao J, Harmon HL, Salo AD, Totterman SM. The use of sequential MR image sets for determining tibiofemoral motion: reliability of coordinate systems and accuracy of motion tracking algorithm. J Biomech Eng, 125(2):246-253, 2003.

[9] Nofrini L, Slomczykowski M, Iacono F, Marcacci M. Evaluation of accuracy in ankle center location for tibial mechanical axis identification. J Invest Surg, 17(1):23-29, 2004.

[10] Victor J, Van Doninck D, Labey L, Innocenti B, Parizel PM, Bellemans J. How precise can bony landmarks be determined on a CT scan of the knee? Knee, 16(5):358-365, 2009.

[11] Benjamin J. Component alignment in total knee arthroplasty. Instr Course Lect, 55:405-412, 2006.

[12] Yoon YS, Hodgson AJ, Tonetti J, Masri BA, Duncan CP. Resolving inconsistencies in defining the target orientation for the acetabular cup angles in total hip arthroplasty. Clin Biomech (Bristol, Avon), 23(3):253-259, 2008.

[13] Reed SC, Gollish J. The accuracy of femoral intramedullary guides in total knee arthroplasty. J Arthroplasty, 12(6):677-682, 1997.

[14] Harding IJ, Crawford RW, Mclardy-Smith P, Murray DW. The importance of femoral intramedullary entry point in knee arthroplasty. The Knee, 6(3): 207-210, 1999.

[15] Mihalko WM, Boyle J, Clark LD, Krackow KA. The variability of intramedullary alignment of the femoral component during total knee arthroplasty. J Arthroplasty, 20(1):25-28, 2005.

[16] Mahaisavariya B, Sitthiseripratip K, Tongdee T, Bohez EL, Vander Sloten J, Oris P. Morphological study of the proximal femur: a new method of geometrical assessment using 3-dimensional reverse engineering. Med Eng Phys, 24(9):617-622, 2002.

[17] Cerveri P, Marchente M, Bartels W, Corten K, Simon JP, Manzotti A. Automated method for computing the morphological and clinical parameters of the proximal femur using heuristic modeling techniques. Ann Biomed Eng, 38(5):1752-1766, 2010.

[18] Subburaj K, Ravi B, Agarwal M. Computer-aided methods for assessing lower limb deformities in orthopaedic surgery planning. Comput Med Imaging Graph, 34(4):277-288, 2010.

[19] Lindstrom P, Turk G. Fast and memory efficient polygonal simplification. Proceedings of IEEE Visualization, pp. 279-286, 1998.

[20] Taubin G. A signal processing approach to fair surface design. Proceedings of the 22nd Annual Conference on Computer Graphics (SIGGRAPH), Los Angeles, California, USA, pp. 351-358, 1995.

[21] Sappa A, Rouhani M. Efficient distance estimation for fitting implicit quadric surfaces. IEEE Int Conf on Image Processing, Cairo, Egypt, pp. 3521-3524, 2009.

[22] Levenberg K. A method for the solution of certain non-linear problems in least squares. Quart Appl Math, 2(2):164-168, 1944.

[23] Marquardt W. An algorithm for least-squares estimation of nonlinear parameters. SIAM J Appl Math, 11(2):431-441, 1963.

[24] Mullaji AB,deakin11 Marawar SV, Mittal V. A comparison of coronal plane axial femoral relationships in Asian patients with varus osteoarthritic knees and healthy knees. J Arthroplasty, 24(6):861-867, 2009.

[25] Deakin AH, Basanagoudar PL, Nunag P, Johnston AT, Sarungi M. Natural distribution of the femoral mechanical-anatomical angle in an osteoarthritic population and its relevance to total knee arthroplasty. Knee, 19(2):120-123, 2012.

[26] Teter KE, Bregman D, Colwell CW Jr. The efficacy of intramedullary femoral alignment in total knee replacement. Clin Orthop Relat Res, 321:117-121, 1995.

[27] Jeffery JA. Accuracy of intramedullary femoral alignment in total knee replacement: intraoperative assessment of alignment rod position. The Knee, 6(3):211-215, 1999.

[28] Mason JB, Fehring TK, Estok R, Banel D, Fahrbach K. Meta-analysis of alignment outcomes in computer-assisted total knee arthroplasty surgery. J Arthroplasty, 22(8):1097-1106, 2007.

[29] Laskin RS, Beksaç B. Computer-assisted navigation in TKA: where we are and where we are going. Clin Orthop Relat Res, 452:127-131, 2006.

[30] Mufty S, Brabants K, Almqvist F, Bellemans J. The variability of surgical practice during total knee arthroplasty: results of a national survey amongst Belgian knee surgeons. Knee Surg Sports Traumatol Arthrosc, 19(10):1662-1668, 2011.

[31] Lotke PA, Ecker ML. Influence of positioning of prosthesis in total knee replacement. J Bone Joint Surg Am, 59(1):77-79, 1977.

[32] Ritter MA, Faris PM, Keating EM, Meding JB. Postoperative alignment of total knee replacement. Its effect on survival. Clin Orthop Relat Res, (299):153-156, 1994.

[33] Seil R, Pape D. Causes of failure and etiology of painful primary total knee arthroplasty. Knee Surg Sports Traumatol Arthrosc, 19(9):1418-1432, 2011.

[34] Windsor RE, Scuderi GR, Moran MC, Insall JN. Mechanisms of failure of the femoral and tibial components in total knee arthroplasty. Clin Orthop Relat Res, (248):15-19; discussion 19-20, 1989.

[35] Motsis EK, Paschos N, Pakos EE, Georgoulis AD. Review article: Patellar instability after total knee arthroplasty. J Orthop Surg (Hong Kong), 17(3):351-357, 2009.

[36] Sikorski JM. Alignment in total knee replacement. J Bone Joint Surg Br, 90(9):1121-1127, 2008.

[37] Lombardi AV Jr, Berend KR, Ng VY. Neutral mechanical alignment: a requirement for successful TKA: affirms. Orthopedics, 34(9):e504-506, 2011.

[38] Cerveri P, Marchente M, Bartels W, Corten K, Simon JP, Manzotti A. Towards automatic computer-aided knee surgery by innovative methods for processing the femur surface model. Int J Med Robot, 6(3):350-361, 2010.

[39] Eckhoff DG, Bach JM, Spitzer VM, Reinig KD, Bagur MM, Baldini TH, Rubinstein D, Humphries S. Three-dimensional morphology and kinematics of the distal part of the femur viewed in virtual reality. Part II. J Bone Joint Surg Am, 85-A Suppl 4:97-104, 2003.

[40] Paley D. Normal lower limb alignment and joint orientation. In: Paley D, Herzenberg JE. Principles of deformity correction. Springer-Verlag, New York, 2002.

[41] Victor, J. Rotational alignment of the distal femur: a literature review. Orthop Traumatol Surg Res, 95(5), 365-372, 2009.

[42] Middleton FR, Palmer SH. How accurate is Whiteside's line as a reference axis in total knee arthroplasty? Knee, 14(3):204-207, 2007.

[43] Eckhoff D, Hogan C, DiMatteo L, Robinson M, Bach J. Difference between the epicondylar and cylindrical axis of the knee. Clin Orthop Relat Res, 461:238-244, 2007.

6 Conclusions and perspectives

In this thesis, a set of landmark extraction tools for automatic 3D analysis of virtual bones was presented and applied on the skull and femur. This chapter gives an overview of the main contributions of this work to the field of 3D landmarks and offers some suggestions for further research.

6.1 Conclusions

The literature review on manual landmark localisation, presented in chapter 2, demonstrates that intra- and interobserver variability can be a limiting factor for obtaining correct measurements from 3D medical images. Differences between landmarks and anatomical directions are found and seem to be consistent among different studies. Landmarks located on relatively flat or widely curved anatomical structures and short axes are more prone to observer variability. However, precise measurements can also be obtained based on these points if the variations are small in the relevant directions. Furthermore, the reliability of manual landmark localisation may depend on the experience of the operator and might be improved through training and by using detailed landmark definitions and anatomical drawings. Finally, the reference frames proposed in literature are usually defined from the most reliable landmarks or landmark directions. By summarising the results for a set of commonly used skeletal cephalometric points it is found that 40 % of the mean 3D intraobserver values are above 1.5 mm and that 52 % of the mean 3D interobserver values are greater than 2 mm. Some of the axes of the knee were found to be very reliable, while other showed mean variations above 2°. By reviewing the literature on automatic landmark localisation, it is seen that fully automatic approaches to process 3D multiplanar images are hard to develop. The methods can be grouped into differential operators and deformable analytical, template and statistical shape models. Compared to local differential operators, deformable models are more robust to image noise by including more a priori knowledge about the landmarks, resulting in better values for the reproducibility. The automatic approaches seem to reduce the time spent for manual intervention and improve the landmark localisation precision. However, the amount of work published on the skull and lower limb bones is very limited. In contrast to multiplanar images, several studies on automatic analysis of 3D models of the lower limbs have been published. The most commonly used methods are curvature analysis and analytical curve and surface fitting. However, most papers describe only one or two techniques or extract only a limited amount of parameters. The most extensive work has been performed by two research groups: one presented methods for automatically measuring lower limb deformities and the other extracted several points and axes on the femur and pelvis and showed that most of the parameters were relatively close to the manual measurements (<2 mm and 2°). However, a complete set of measurements of femoral and tibial alignment has not yet been presented. In contrast to the lower limbs, no automatic approaches for landmark localisation on the virtual skull model have been proposed.

The mathematical background of the algorithms that were implemented and applied in this thesis was given in chapter 3. Different mesh operations were presented to process the 3D models. The simplification method proposed by Lindstrom & Turk was applied to reduce the model size. Using Taubin's $\lambda|\mu$ algorithm, the models were smoothed to remove noise and useless details. The subdivision technique of Dyn et al. and Zorin et al. was implemented to smoothly refine the mesh. Finally, by measuring the distance between two triangulated surfaces it was shown that the mesh operations can be performed without introducing large geometric errors. Because of the many different types of landmark definitions found in literature, the combination of multiple landmark extraction techniques is often desired for a complete 3D analysis of the bone geometry. Therefore, different methods were implemented and tested on the skull and femur. Convex-, concave- as well as saddle-shaped structures can be processed to detect the extreme points in predefined directions. Also, methods for curvature analysis of 3D curves and surfaces were implemented. While the first method allows for extracting points of local extreme curvature on a curve, the surface curvature values are more difficult to process and to reduce to one particular point. Geometrical entity fitting could be more robust to noise as it allows to approximate the anatomical structures with several predefined shapes. Furthermore, the smallest or largest cross-section of the mesh can be computed by searching for an optimal slicing plane. Another method is to use the rotational inertia characteristics of the surface mesh to extract the principal axes of the geometry. Finally, a 2D projection algorithm was implemented to create a 2D contour from the 3D surface mesh.

In chapter 4, a semi-automatic approach for landmark localisation on the 3D virtual skull was presented. The method allows the user to select a ROI in which the landmark is located and the exact position of the point is then determined automatically using the extreme point technique. While the method was first evaluated by assessing the intra- and interobserver variability for measurements performed on one image of each skull, further research was done to improve the technique and determine the intraobserver variability for measurements performed on different images of the same skull. It was shown that the automatic approach allows for precise landmark localisation. The results were compared to studies reporting on manual landmark localisation using 3D images. Differences in precision between landmarks and anatomical directions were observed and were in agreement with other studies. The mean 3D intraobserver variations are below 1.4 mm and the maximum variations are below 2 mm for 11 of the 15 studied landmarks. A major advantage of the automatic analysis might be that it is less prone to outlier variations. Finally, a reliable reference frame for cephalometric analysis was proposed. Overall, the proposed method is novel and allows for a more objective and standardised 3D analysis of the skull. The automatic analysis can contribute to an improved 3D surgical planning as well as evaluation of orthognathic surgery.

The femur was fully automatically analysed in chapter 5 using a variety of landmark extraction techniques. The 3D femoral anatomical axis was extracted from a series of best-fit hyperboloids to the shaft and used to determine the optimal intramedullary rod entry point. In addition, it was shown that precise measurements could be obtained using a reduced scanning protocol. Including the central part of the femur is required to correctly measure femoral bowing. Next, various reference axes to study femoral alignment were automatically determined by applying the different feature extraction methods presented in chapter 3. Relevant angular measurements in the three anatomical planes were made and it was shown that most measurements are in agreement with mean values reported in literature. The presented techniques form a basis for a more objective and standardised 3D analysis of femoral alignment. The automatic analysis can contribute to a faster and more precise 3D planning and evaluation of TKA.

This thesis aimed at developing automatic approaches to extract reference points and axes that could be used for orthognathic surgery and TKA. A novel semi-automatic approach for landmark localisation on the virtual skull was proposed and an extensive set of tools to measure femoral alignment was presented. Landmark definitions were adapted to include the three dimensions, mathematical descriptions and reference frames were proposed and the methods were evaluated using different techniques. The automatic methods save time for the surgeon and allow for a more objective analysis of patient data.

6.2 Future work

The main contribution of this thesis to the field of 3D landmarks is that several techniques for automatic landmark localisation have been implemented and applied to the 3D virtual skull and femur. However, further work is needed to employ these methods for clinical applications. In this thesis, the main focus was on orthognathic surgery and TKA. While several landmarks of the skull have been extracted, the semi-automatic procedure should be employed to detect the landmarks on the jaws, teeth and face. Furthermore, reliable measurements for cephalometric analysis should be proposed based on these landmarks. Various reference axes of the femur were automatically computed. However, relevant measurements for planning and evaluation of surgery should be determined and the alignment of the tibia and prosthesis components should be studied. Furthermore, the current procedures require a 3D model of the bony anatomy as input. Although CT imaging allows to obtain high contrast images of the bone structures, which can be mainly segmented using thresholding and region growing algorithms, some manual intervention might be required. (Semi)-automatic approaches for segmentation could be investigated to allow for a faster analysis of the patient data. Finally, further validation of the results is required prior to clinical application.

Different methods were used to evaluate the results of the automatic analysis: multiple trials were performed by one or more operators, different images of the same anatomical part were studied, images of the complete anatomy were compared to images of part of the anatomy and mean values were compared to literature. However, the main limitation in the evaluation of the landmark extraction methods is that the accuracy of the landmark positions was not assessed. While the semi-automatic procedure for the skull improves the precision of landmark localisation and the fully automatic procedure for the femur eliminates observer variability, the trueness of the results should be obtained to further validate the methods. The landmark positions should therefore be compared with measurements obtained on dry bones. The objective of this validation step is twofold: assess the closeness of agreement between the automatic methods and the clinical knowledge and assess the closeness of agreement between the virtual 3D models and the true anatomical structures. As an intermediate step, the (semi-)automatically obtained measurements could thus be compared to the mean values of a set of manually obtained measurements on the 3D models. A tool was already developed to manually identify landmarks on the 3D model, using point-picking as well as manual geometrical entity fitting, which can be applied for future studies. Finally, the accuracy of the imaging and the image processing procedure should be assessed by comparison with data obtained on dry bones or on highly accurate laser surface scanning images.

Some suggestions for further research on the landmark extraction techniques can also be made. As mentioned in chapter 4, the landmarks on the skull were determined by locally processing the anatomical regions and extracting a single extreme point. It could be investigated if semi-global approaches, such as quadric surface fitting, could further improve the precision. Also, curvature analysis instead of predefined directions might be employed to process ridge-like structures. One method for estimating curvature values on the surface mesh was implemented and tested in this thesis. However, other methods have been proposed in literature and it could be interesting to test their robustness to noise to extract tip-like structures, such as the femoral epicondyles. Furthermore, smoothing algorithms based on the normal vectors of the mesh might be investigated, as they may better preserve small scale features.

The bone models were analysed by mainly computing clinically relevant points and axes that are commonly discussed in the literature. In future work, it would also be interesting to define new landmarks and measurements, which could be more accurately obtained using the automatic methods compared to the manual analysis (e.g. using 3D geometrical objects). To be used in clinical practice, however, those landmarks should either be related to existing clinically relevant landmarks or normal values should be established for the new variables.

The surgical procedures that are discussed in this thesis aim at achieving a proper alignment of bones and prosthesis components and mainly deal with non-deformed anatomical structures. The landmark extraction methods were therefore developed and tested on such normal morphologies. However, it would be interesting to apply the algorithms on deformed shapes to evaluate how well these cases can be analysed using the current techniques. Moreover, it would be useful to develop specific tools to analyse abnormal morphologies.

As this thesis provides a basis for landmark extraction from 3D models, the tools could be customised for several other applications. The algorithms can be applied to other human bones, such as the tibia, pelvis and spine. Many orthopaedic surgical procedures rely on landmark-based measurements for preoperative planning, surgical instrument positioning or implant design. Typical examples are arthroplasties, osteotomies and fracture treatments. As mentioned in chapter 3 and demonstrated in chapters 4 and 5 for the skull and femur, however, a new strategy needs to be developed for the (semi-)automatic analysis of each specific bone, which includes orienting the model in a standardised way, selecting the anatomical structures on which the landmarks are located, extracting the positions of the points and axes and deriving clinically relevant measurements. A fast analysis of patient data can also be of interest to gain additional insights in different pathological morphologies and to compare the results of different surgical procedures. Data on joint kinematics could be analysed in a more standardised and objective way by automatically computing coordinate systems. Moreover, other anatomical tissues that contain distinct features could be analysed (e.g. the face). The methods could also be applied outside the medical field, such as for forensic anthropometry or morphometrics of other biological specimens.

List of Figures

List of Tables

Publications

Publications in international journals

First author

- Van Cauter S, Okkerse W, Brijs G, De Beule M, Braem M, Verhegghe B. A new method for improved standardisation in three-dimensional computed tomography cephalometry. Computer Methods in Biomechanics and Biomedical Engineering, 13(1): 59-69, 2010.
- Van Cauter S, De Beule M, Van Haver A, Verdonk P, Verhegghe B. Automated extraction of the femoral anatomical axis for determining the intramedullary rod parameters in total knee arthroplasty. International Journal for Numerical Methods in Biomedical Engineering, 28(1):158-169, 2012.

Co-author

- De Beule M, Van Cauter S, Mortier P, Van Loo D, Van Impe R, Verdonck P, Verhegghe B .Virtual optimization of self-expandable braided wire stents. Medical Engineering Physics, 31(4):448-453, 2009.
- Praet T, Adriaens D, De Beule M, Van Cauter S, Verhegghe B. Design from nature: kinematic modelling of the musculoskeletal structure of the seahorse tail. International Journal for Numerical Methods in Biomedical Engineering, submitted.

Book chapters

- Gomes GT, Van Cauter S, De Beule M, Vigneron L, Pattyn C, Audenaert EA. Patient-specific modelling in orthopedics: from image to surgery. Biomedical imaging and computational modeling in biomechanics, Springer, accepted.